UNIVERSITY OF OKLAHOMA
GRADUATE COLLEGE

PSEUDO-INVERSE IMAGING FOR GROUND PENETRATING RADAR DATA

A Dissertation
SUBMITTED TO THE GRADUATE FACULTY
in partial fulfillment of the requirements of the
degree of
Doctor of Philosophy

By

YAN CHEN
Norman, Oklahoma
2001

UMI Number: 3029617

Bell & Howell Information and Learning Company
300 North Zeeb Road
P.O. Box 1346
Ann Arbor, MI 48106-1346

PSEUDO-INVERSE IMAGING FOR GROUND PENETRATING RADAR DATA

A Dissertation APPROVED FOR THE SCHOOL OF GEOLOGY AND GEOPHYSICS

BY

ACKNOWLEDGEMENTS

I would like to express my deep gratitude and appreciation to my advisor, Dr. Alan Witten, for his guidance, encouragement, and constant support throughout my Ph.D. program. I would also like to thank Dr. Ross Deming, for his suggestions in conducting the research work for this dissertation, and his help and support when I was in difficulties. Thanks are also due to other members of my advisory committee, Dr. Judson Ahern, Dr. John Castagna, Dr. Walter Wei, and Dr. Roger Young, for their advice and support on my research, and their reviewing the manuscript.

I would like to thank Dr. Claren Kidd of Youngblood library, University of Oklahoma, for her assistance and encouragement. Many thanks to all the staff members, Donna Mullins, Stephen Sandifer, Brian Silver, Nancy Leonard, Carol Drayton, Terry Brady in particular, for their help and cooperation. I would like to thank my friends, Kristie White, Jan Dodson, Greg Calvert, Shengjie Sun, Qiang Sun, Julie Staggs and all others who helped me during my stay here.

Finally, I would like to thank my parents, Zhirong Chen and Shijun Hu, my husband, Hehua Zheng, and son, Norman Zheng, who loved me and shared my dreams and frustrations, for their understanding, encouragement and constant support, which made it possible to complete this work. I also thank all other members of my family for their support and encouragement.

Contents

List of Figures

Abstract

Ground Penetrating Radar (GPR) is a proven method of characterizing the shallow subsurface. Most interpretations using GPR have relied upon raw data records or records that have been processed with seismic data processing techniques. To aid in the interpretation of GPR reflection sections, a regularized pseudo-inverse algorithm is described based on Geophysical Diffraction Tomography (GDT) from multifrequency multi-monostatic GPR measurements. The algorithm is based on the first Born approximation for vector electromagnetic (EM) scattering. Fully analytical reconstruction results are obtained by using a regularized pseudo-inverse operator. In contrast to existing matrix-based methods, which numerically calculate the pseudo-inverse, our calculations are based on continuous operators. The main advantage of our method is the computational efficiency. While the existing, analytical, GDT techniques, known as Filtered Backpropagation (FBProp), require a lossless background, the algorithm described here allows either a lossless background medium or an attenuating background. Since radar wavelengths are often times on the same order as the depth and size of underground object of interest, the evanescent components are included in our algorithm to enhance the image resolution. The quality of the images and limitations of some simplifying assumptions are investigated for two-dimensional and three-dimensional algorithms using both simulated and experimental data. It is found that our inversion formula yields

good image quality and is not substantially limited by the necessary simplifying assumptions.

1 Introduction

In this thesis, the inverse scattering methodology is used to develop an algorithm for geophysical imaging which is based on Geophysical Diffraction Tomography (GDT) [10, 13, 34, 41, 53, 56, 59]. Inverse scattering problems are, in general, nonlinear [3]. However, it is possible to linearize the original nonlinear inverse scattering problems by using some approximations, such as the Born or Rytov approximation [36], geometrical optics approximation [32], etc. Our algorithm uses the regularized pseudo-inverse operator [3, 9, 10], to compute minimum energy solutions for linear underdetermined inverse scattering problems.

The pseudo-inverse algorithm [9, 10] employed in this thesis is useful for geophysical tomographic imaging in a monostatic measurement geometry with intended application for the signal processing of GPR data. GPR imaging is one of the most popular techniques associated with shallow subsurface characterization, such as locating pipes at construction sites, detecting explosive mines in military zones, locating toxic waste at industrial dumps, etc. GPR tends to be one of the methods of choice because of its field efficiency and nonintrusiveness.

In the literature, many authors have used the regularized pseudo-inverse as the basis for geophysical imaging. Some of the methods focused on numerical matrix-based techniques [43, 45, 48], such as Singular Value Decomposition (SVD) and Conjugate Gradients (CG) algorithm. In contrast, our algorithm is based on continuous operators rather than matrices. Computational efficiency is the main advantage of our directly fully analytical inversion.

1.1 Electromagnetic (EM) Inverse Scattering

Inverse scattering is the designation for mathematical methods that are used to obtain information about an object from the scattered wave field measured outside the object (Figure (1-1)). Inverse scattering applies to a wide range of areas, such as landmine detection, remote sensing, medical imaging, target identification, geophysical exploration, and non-destructive testing. The object, from which the information is desired, is usually inaccessible or its material properties are unknown such that the application of wave fields is one of the few possible means for exploration. Our GPR imaging problem belongs to the category of *EM inverse scattering* problems in which EM wave fields are employed.

EM inverse scattering can be considered as the opposite of *forward scattering*. In forward scattering one determines the explicit or implicit relation for the electric or magnetic field outside the object as a function of some properties describing the object. For instance, for our GPR imaging problems, the properties of the object of interest are the constitutive parameters, which are, permittivity, permeability, and conductivity. The explicit or implicit relation is referred to as the *forward model*. The inverse scattering scheme is arrived at by inverting the forward model. This scheme expresses the constitutive parameters as a function of the electric or magnetic field.

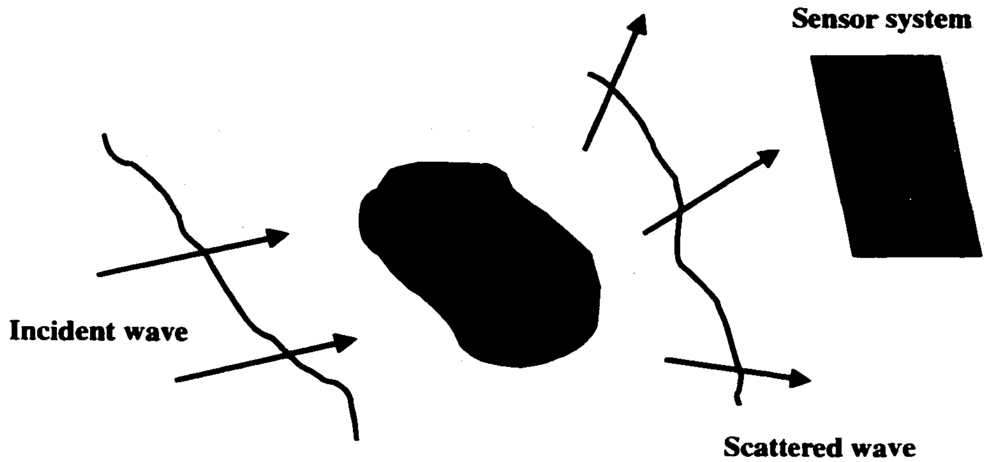

Figure 1-1: Illustration of inverse scattering configuration (after A.J. Devaney, 1999)

By measuring the electric or magnetic field and using the inverse scattering scheme it is possible to obtain the desired information about the object.

The inversion of the forward model is, however, not a simple task. The EM inverse scattering problems are, in general, nonlinear problems. In order to simplify the problem or to transform it from an implicit into an explicit expression, it is often convenient to introduce some physical approximations, which allow a linearization of the nonlinear problem. A well-known case is that of a weak scatterer; here Born approximation [36] may be used. Another kind of approximation that also leads to a linear problem is Rytov approximation [36], which is valid when variations in the properties of the scatterer are large compared to the wavelength of the incident radiation [3]. In our GPR imaging problems, the first Born approximation is used to linearize our forward scattering model.

The linear EM inverse scattering problem can be formulated as follows [3]: Given $\mathbf{g} \in \mathbf{U}$ and a linear operator $\mathcal{A} : \mathbf{U} \rightarrow \mathbf{V}$, find $\mathbf{f} \in \mathbf{V}$ such that

$$\mathbf{g} = \mathcal{A}\mathbf{f} \tag{1-1}$$

An element of $\mathbf{V}$ will be called an *object* while an element of $\mathbf{U}$ will be called an *image*. Accordingly, $\mathbf{V}$ will be the *object space* and $\mathbf{U}$ will be called the *image space*. $\mathcal{A}$ is a coupled set of integral operators describing the physical process. For example, in GPR imaging problems, $\mathcal{A}$ is a linearized forward EM scattering model, based on the wave equation, relating underground inhomogeneities to measurements of the scattered EM field. In such problems, it is assumed that both $\mathbf{U}$ and $\mathbf{V}$ are Hilbert spaces.

According to the definition introduced by Courant and Hilbert, in Equation (1-1) the inverse problem of finding $\mathbf{f}$, given $\mathbf{g}$, is *well-posed* in the sense of Hadamard [3] if the solution $\mathbf{f} \in \mathbf{V}$ exists for any $\mathbf{g} \in \mathbf{U}$ (existence of solution), if the solution $\mathbf{f}$ is unique in $\mathbf{V}$ (uniqueness), and if the inverse mapping $\mathbf{g} \rightarrow \mathbf{f}$ is continuous (stability). When Equation (1-1) is the mathematical model of the given EM inverse scattering problem, it may not satisfy these criteria. In such cases, the problem is said to be *ill-posed*. For example, GPR imaging is ill-posed since it is underdetermined, which means that there's not enough data to uniquely determine the unknown function describing the properties of the object. *Regularization* is one of the basic theories in the treatment of ill-posed problems. This will be addressed below.

1.2 Ground Penetrating Radar (GPR) Imaging

Radar (*radio detection and ranging* for short), a system that uses short EM pulses, was fully developed in Britain for defense against enemy planes during the Second World War, although several such systems did exist in Britain, France, Germany and the USA before the War[2]. In addition to its numerous military and civil applications, radar is now a very important tool in ground investigations, normally from the near surface to a depth of several tens of meters. Ground penetrating radar (GPR) is a geophysical method which employs EM waves, typically in 1 MHz to 1GHz frequency range, for high-resolution detection, imaging and mapping of subsurface structures.

A typical GPR system has three main components: Transmitter and receiver that are directly connected to antennas, and a control unit (timing) (Figure (1-2)). The transmitting antenna radiates a short high-frequency incident EM pulse into the ground. This incident wavefield is then scattered as it encounters changes in dielectric permittivity and electric conductivity corresponding to subsurface inhomogeneities. The propagation of a radar signal depends mainly on the electrical properties of the subsurface materials. Waves that are scattered back toward the earth's surface induce a signal in the receiving antenna, and are recorded as digitized signals for display and further processing. This process is normally repeated many times, where in each experiment either the incident field is altered or the transmitting/receiving antennas are repositioned. By processing the group of scattered field measurements, we seek to identify buried structures and/or determine their material properties.

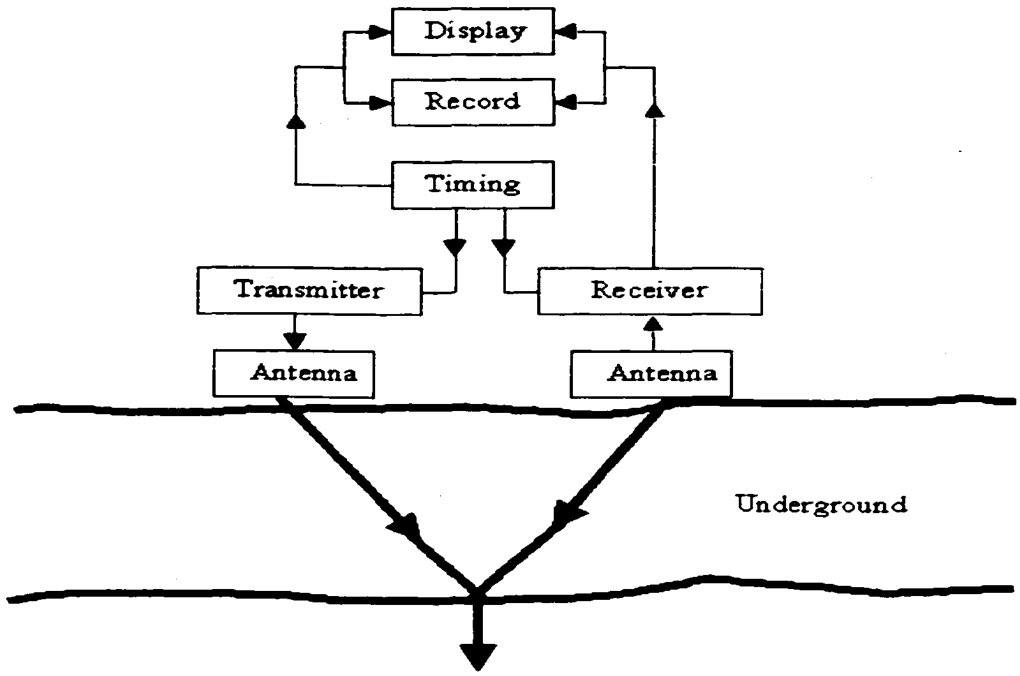

Figure 1-2: Flow chart for a typical GPR system (after Davis et al., 1989)

GPR systems can be deployed in three basic modes. The most common operation mode of GPR is the *Reflection mode*, whereby traces of returned waves are collected either continuously or in stations along a line, thus creating a *time cross-section* of the subsurface[2]. *Common-mid-point Sounding* which is used to estimate velocity versus depth by varying antenna spacing and identifying the time move out versus antenna separation for the various EM wavefronts, and *Transillumination* are other two modes of operation [1, 2]. In this thesis, both two-dimensional and three-dimensional GPR data were collected using the reflection mode.

When operating a GPR system in the conventional reflection mode, a reflection profile is obtained. Most of the returned signals in such a profile are reflections from subsurface discontinuities. However, in certain common conditions during GPR investigations, in addition to reflections, the EM waves undergo *diffractions*, which is the main interest for our imaging objective in this thesis, from small inhomogeneities and objects. Diffractions that can be identified as *hyperbolas* in the time section occur in two cases: when the dominant wavelength in the radar pulse is lager than the dimensions of the diffractions' source, and when waves are diffracted from sharp edges[2].

GPR surveys are based on two different measurement geometries that are referred to here as the *multi-monostatic* and *multi-bistatic* geometries. In this thesis, our pseudo-inverse algorithm is used to solve the imaging problems for multi-monostatic GPR data. But, it also could be used to solve GPR imaging problems in multi-bistatic geometry by slightly changing the algorithm.

The multi-monostatic geometry is defined to be measurements made with a co-located transmitter and receiver that are moved in unison along a line on the ground surface (Figure (1-3)). This is the commonly utilized measurement geometry in GPR and is also referred to as zero-offset seismic reflection. This measurement geometry is monostatic in the sense that transmitters and receivers cannot be independently positioned. The multi-bistatic geometry is defined to be the standard seismic reflection geometry (Figure (1-4)) where an array of receivers is deployed at a uniform spacing over a line on the ground surface. Multiple transmitter positions are similarly established at a uniform spacing over the same line. This geometry is referred to as bistatic because the transmitter and receiver positions are independent of each other.

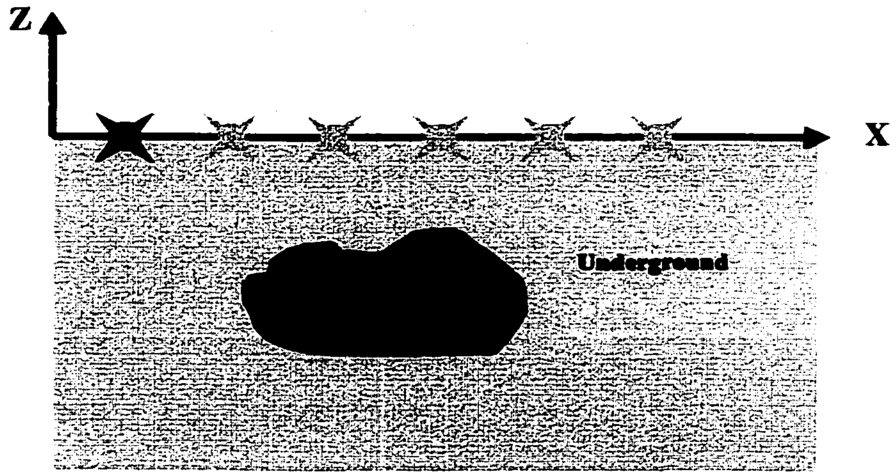

Figure 1-3: Illustration of the two-dimensional multi-monostatic reflection geometry. The **x** and • represent transmitter and receiver locations, respectively. One transmitter/receiver pair is represented in black while the rest are gray to indicate that only a single pair is used to traverse the x-direction or, if an array of receivers is employed, data is recorded for the receiver co-located with the transmitter. (After A.J. Witten, 1999)

A useful step in processing the large volume of raw data acquired by GPR is to compute a radar image that shows (approximately) the location and strength of scattering centers, such as buried objects. This thesis describes a GPR imaging algorithm, called pseudo-inverse imaging, which is an extension of a DT algorithm for multi-monostatic GPR imaging developed by Deming and Devaney [9, 10]. This imaging technique belongs to the general category known as EM inverse scattering methods. EM inverse scattering methods in general consist of two steps, first, deriving a mathematical equation representing the forward model, and second, mathematically inverting the forward model, subsequently solving for a function describing the buried objects.

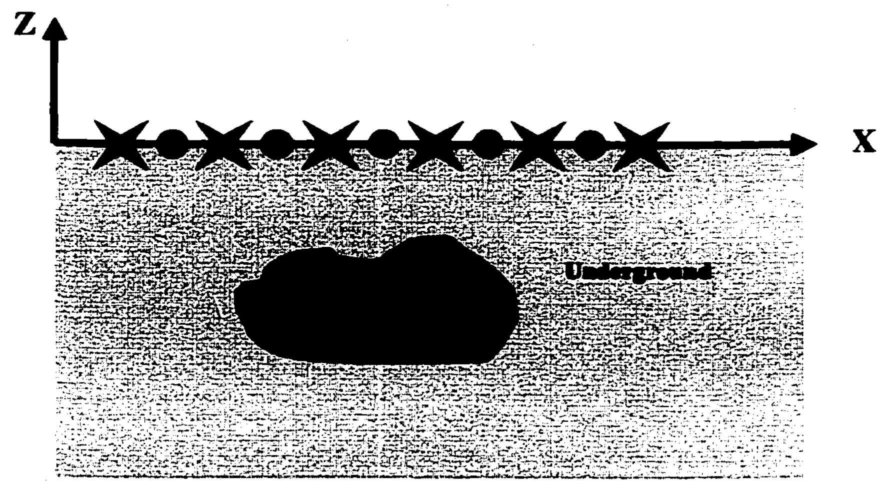

Figure 1-4: Illustration of the two-dimensional multi-bistatic reflection geometry. The **x** and • represent transmitter and receiver locations, respectively. (After A.J. Witten, 1999)

Our pseudo-inverse imaging algorithm is related to well established method of DT, which is used in various forms for such applications as optical inverse scattering, medical ultrasonic imaging, and geophysical imaging. In many applications of DT [13, 14, 41, 53, 56, 59, 61], the ground attenuation effects are assume to be negligible, evanescent components are discarded, and the assumption of ideal point sources/receivers are employed. However, in GPR imaging, the soil background losses are significant, and evanescent wavefield components are important because radar wavelengths are often times on the same order as the depth and size of underground objects of interest [10]. Therefore, in our algorithm, the soil attenuation is incorporated into the mathematical inversions, and evanescent components are included to help enhance the image resolution. Moreover, a realistic near-field model for the transmitting/receiving antenna pair is employed. Deming and Devaney [10] successfully tested the two-dimensional algorithm using computer simulated data.

Here, reconstructed images from two-dimensional and three-dimensional simulated and experimental data will be presented.

We summarize our methodology as follows. The pseudo-inverse algorithm employed in this thesis consists of several steps. First, a vector EM forward scattering model is defined based on the Born approximation. We use either ideal point sources/receivers or Kerns' scattering matrix formulation [27] to simulate the near-field characteristics of the transmitting and receiving antennas. This forward model then yields a coupled set of integral equations, relating the data at each excitation frequency to the "object function". Finally, the regularized pseudo-inverse algorithm is applied to get the fully analytical inverse solution for the object function.

1.3 Dissertation Organization

EM inverse scattering and GPR imaging are introduced briefly above. In Chapter 2, background information is given to better understand the application of the pseudo-inverse imaging algorithm based on DT techniques. We start with the derivation of the first Born approximation in Section 2.1, then a general review of the existing important tomography methods in Section 2.2, including Filtered Backprojection (FBP), Filtered Backpropagation (FBProp), Algebraic Reconstruction Technique (ART) and Synthetic Aperture Radar (SAR). In Section 2.3, the pseudo-inverse algorithm is introduced in full detail.

Chapter 3 is devoted to our GPR imaging algorithm, using both point sources/receivers and Kerns' scattering matrix model. The three-dimensional algorithm is given in Section 3.1, and the two-dimensional algorithm is given in Section 3.2. For both algorithms, first, the forward EM Scattering model is developed based on the vector wave equation. Then, the inversion method based on a fully analytical pseudo-inverse technique is developed.

We present our reconstruction results in Chapter 4. Two-dimensional and three-dimensional images of both synthetic and experimental GPR data are presented in Section 4.1 and Section 4.2, respectively. Here, we show reconstructed images for a number of examples. Experimental examples show that the algorithm can image plastic and metallic pipes buried in a half-space. The examples are designed to show the robustness of our algorithm and the improvements over standard DT algorithms. Finally, in Section 5, we give conclusions about this research project and discuss possible future directions.

2 Background

2.1 Born Approximation

Our DT algorithm is designed based on the framework of linearized EM inverse scattering. The term *linearized* refers to the fact that the forward model underlying the inverse scattering problem has been linearized using the first Born approximation. Thus, we give a brief derivation of the first Born approximation as following.

It is well-known that the EM wave field $\overline{\mathbf{U}}(\mathbf{r}, t)$ in the time domain is governed by vector wave equation

$$\nabla^2 \overline{\mathbf{U}}(\mathbf{r}, t) - \frac{1}{c^2(\mathbf{r})} \frac{\partial^2 \overline{\mathbf{U}}(\mathbf{r}, t)}{\partial t^2} = \overline{\rho}(\mathbf{r}, t) \tag{2-1}$$

where $\mathbf{r}$ is the spatial coordinate, t is the time variable, c($\mathbf{r}$) is defined as a spatially-variable wave speed and $\overline{\rho}(\mathbf{r}, t)$is a source distribution. Equation (2-1) can be transferred into the frequency domain

$$\nabla^2 \mathbf{U}(\mathbf{r}, \omega) + \frac{\omega^2}{c^2(\mathbf{r})} \mathbf{U}(\mathbf{r}, \omega) = \rho(\mathbf{r}, \omega) \tag{2-2}$$

where ω is the angular frequency. Define the *object function* $\mathbf{O}$ as

$$\mathbf{O}(\mathbf{r}) = 1 - \frac{{c_0}^2}{c^2(\mathbf{r})} \tag{2-3}$$

where c_0 is the background wave speed. Defining k to be the associated wave number at frequency ω, the term $\omega^2/c^2(\mathbf{r})$ appearing in Equation (2-2) can be written as

$$\frac{\omega^2}{c^2(\mathbf{r})} = \frac{k^2 {c_0}^2}{c^2(\mathbf{r})} = k^2 - k^2\left[1 - \frac{{c_0}^2}{c^2(\mathbf{r})}\right] = k^2 - k^2\mathbf{O}(\mathbf{r}) \qquad (2\text{-}4)$$

Using this relationship in Equation (2-2) gives

$$\nabla^2\mathbf{U}(\mathbf{r},\omega) + k^2\mathbf{U}(\mathbf{r},\omega) = \rho(\mathbf{r},\omega) + k^2\mathbf{O}(\mathbf{r})\mathbf{U}(\mathbf{r},\omega) \qquad (2\text{-}5)$$

Or, Equation (2-5) can be expressed in the form of an integral equation

$$\mathrm{U}(\mathbf{r},\omega) = -\int d\boldsymbol{\xi}\rho(\boldsymbol{\xi},\omega)\mathbf{G}(\mathbf{r}-\boldsymbol{\xi},\omega) - k^2\int d\boldsymbol{\xi}\mathbf{O}(\boldsymbol{\xi})\mathbf{U}(\boldsymbol{\xi},\omega)\mathbf{G}(\mathbf{r}-\boldsymbol{\xi},\omega) \qquad (2\text{-}6)$$

where $\mathbf{G}$ is Green's dyadic. If the goal of an analysis is to image, that is to characterize $\mathbf{O}$ and thus $c(\mathbf{r})$ in terms of measurements of $\mathbf{U}$ over some contour $\mathbf{r}$, it is clear that left hand side of Equation (2-6) is known by measurement. On the right hand side of Equation (2-6), the term $\mathbf{U}(\boldsymbol{\xi},\omega)$ appearing under the second integral is unknown since this is the wave field that exists within the inhomogeneities. If not for this term, all quantities would be known except $\mathbf{O}$ and it would be possible to invert Equation (2-6) so as to express $\mathbf{O}$ in terms of the measured data $\mathbf{U}$.

In order to facilitate this inversion, Equation (2-6) can be linearized by invoking the first Born approximation. This is accomplished by defining the wavefield $\mathbf{U}$ to be an incident field $\mathbf{U}_i$ and a scattered field $\mathbf{U}_s$ associated with the inhomogeneities $\mathbf{O}(\mathbf{r}) \neq 0$

$$\mathbf{U} = \mathbf{U}_i + \epsilon \mathbf{U}_s \tag{2-7}$$

where ϵ is a small real positive number, and the fact that $\mathbf{U}_s$ is assumed to be small is explicitly represented by this small multiplicative factor. Similarly, it is assumed that the small scattered field $\mathbf{U}_s$ is created by weak inhomogeneities explicitly expressed as $\epsilon\mathbf{O}(\mathbf{r})$. Substituting these expression into Equation (2-5) and collecting terms of the same order of ϵ gives

$$\begin{aligned}
&\epsilon^0 : \nabla^2 \mathbf{U}_i + k^2 \mathbf{U}_i = \rho && \text{incident field} \\
&\epsilon^1 : \nabla^2 \mathbf{U}_s + k^2 \mathbf{U}_s = k^2 \mathbf{O}\mathbf{U}_i && \text{scattered field} \\
&\epsilon^2 : k^2 \mathbf{O}\mathbf{U}_s \ldots &&
\end{aligned} \tag{2-8}$$

Using Equation (2-8), Equation (2-6) splits into two equations

$$\mathbf{U}_i(\mathbf{r}, \omega) = -\int d\boldsymbol{\xi} \rho(\boldsymbol{\xi}, \omega) \mathbf{G}(\mathbf{r} - \boldsymbol{\xi}, \omega) \tag{2-9}$$

and

$$\mathbf{U}_s(\mathbf{r},\omega) = -k^2 \int d\boldsymbol{\xi}\mathbf{O}(\boldsymbol{\xi})\mathbf{U}_i(\boldsymbol{\xi},\omega)\mathbf{G}(\mathbf{r}-\boldsymbol{\xi},\omega) \tag{2-10}$$

Thus, by invoking the first Born approximation, the unknown term $\mathbf{U}$ appearing under the integral in Equation (2-6) has been replaced by the incident field $\mathbf{U}_i$ and, in this form, an inversion of Equation (2-10) can be derived.

From the derivation above, we could summarize that the first Born approximation implies that multiple interactions within a scattering object are neglected. Hence, the approximation is valid only for weak scattering objects, that is, the size of the object must be small in wavelengths or its EM properties (permittivity, conductivity, permeability) must not differ much from those of the background medium.

2.2 Existing Inversion Algorithms for Tomography Problems

The inverse scattering problem is, in general, nonlinear and ill-posed. Over the years, several techniques have been developed for this problem, and a very rough classification would place these into linearized model or solving the full nonlinear problem by optimization methods [6]. These approaches have their advantages as well as their drawbacks. Generally, nonlinear methods can generate more accurate solutions since they are not limited by the linearized approximations. But, nonlinear methods are more computational intensive since they require a certain amount of iterations to get to the final results and these iterations may not necessarilly converge to the correct result. Nonlinear methods are not the focus of our current research, but could be an important direction for future research. In this section, we give several tomography algorithms based on the linearized model that serve as a basis for our GPR imaging algorithm. These methods are discussed individually below.

2.2.1 Filtered Backprojection (FBP)

The basic idea of tomography is to use data outside an object to infer values inside the object. Radon [8] showed that if a complete set of sums or projections of the object's parameters were measured then the parameters of the object could be calculated. In fact, Radon derived an analytic formula (Radon Transform) that relates the object's parameter (object function) to its projections. The Radon transform provides the mathematical basis for slant stack procedures and is well known by geophysicists. In tomographic applications, the transform is used to map a series of one-dimensional projections into a two-dimensional grid from which an image of an object may be obtained. Given a line l which is a perpendicular distance d and form an angle θ with respect to a Cartesian coordinate system origin (Figure (2-1)), the Radon transform changes the system from an (x, y) to (d,θ) coordinate system by integrating a function of (x, y) along the line l [33].

$$R\left[\mathbf{f}(x,y)\right] = \mathbf{P}(d,\theta) = \int_{-\infty}^{\infty}\int_{-\infty}^{\infty} dxdy\delta(xcos\theta + ysin\theta - d)\mathbf{f}(x,y) \tag{2-11}$$

where $\mathbf{f}(x,y)$ is an object function, $\mathbf{P}(d,\theta)$ is a set of projections, and $d = xcos\theta +$

$y sin\theta$.

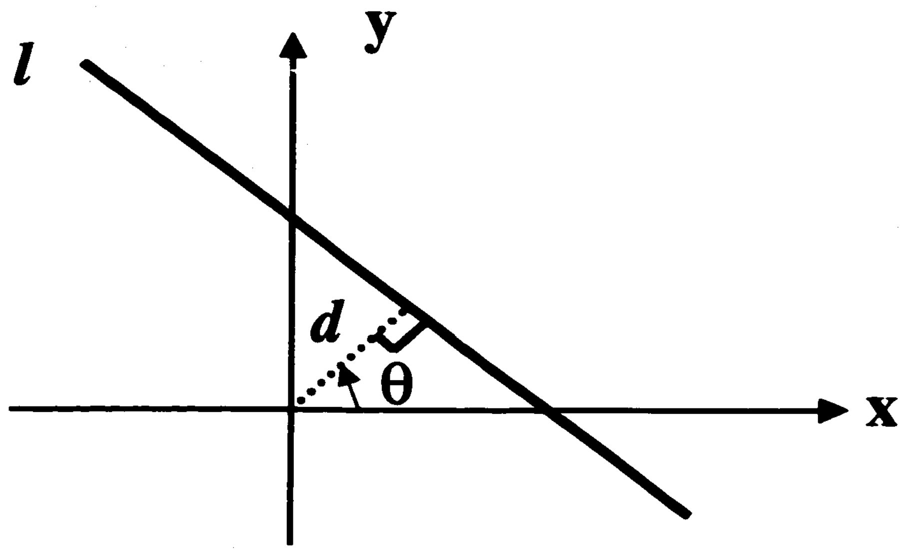

Figure 2-1: Performing a Radon Transform by integrating a function of (x,y) along the line l to a function of (d, θ). (After Basson, 2000)

The forward and inverse Radon transform can easily be implemented using the Projection Slice theorem [44]. This theorem states that the one-dimensional Fourier transform along a line l_i is a slice at the same position of the two-dimensional Fourier transform of the original object:

$$\tilde{\mathbf{P}}(K,\theta) = \frac{1}{\sqrt{2\pi}} \int_{-\infty}^{\infty} \int_{-\infty}^{\infty} dxdy e^{-iKd} \mathbf{f}(x,y) \tag{2-12}$$

where K is the spatial frequency variable, and $\tilde{\mathbf{P}}(K,\theta)$ is the spatially Fourier transformed projection. This theorem provides the means to construct the two-dimensional object from a series of one-dimensional projections through the object. *Backprojec-*

tion [21] is an operation which sums projected values (Radon transforms) together.

Backprojection is only valid when the wavelength of the source is significantly smaller than the dimensions of the object in question. In practice, the method of backprojection is also limited by the finite bandwidth (a non-spike impulse response) of the insonifying wave. Thus, from the reconstruction of backprojection, we often see a blurring image, or we might say that the true image has been convolved with the smearing Point Spread Function (PSF) to form the output image. To attain a better image, it is reasonable to attempt to design an inverse *filter* to collapse the blur or response back to a point. So, the notion of *filtered backprojection* (FBP) arises to provide a clearer image.

In FBP, the projections are multiplied by a band-limited impulse function h defined by

$$h(d) = \frac{1}{2\pi} \int_{-\omega}^{+\omega} dK |K| e^{iKd} \tag{2-13}$$

where the frequency bandwidth of K extends from $-\omega$ to $+\omega$ where K and d form a Fourier transform pair [26]. The frequency weighting factor $|K|$ is the spatial deconvolution factor which removes the backprojection blurring.

The filtering step can be expressed by the following equation [26]

$$\mathbf{P}_{\mathit{filt}}(d,\theta) = \int_{-\infty}^{\infty} dd' h(d-d')\mathbf{P}(d',\theta) \tag{2-14}$$

where $\mathbf{P}_{\mathit{filt}}$ is referred to *filtered data*. In the spatial frequency domain, Equation (2-14) is represented as

$$\tilde{\mathbf{P}}_{\mathit{filt}}(K,\theta) = H(K)\tilde{\mathbf{P}}(K,\theta) \tag{2-15}$$

where $\tilde{\mathbf{P}}_{\mathit{filt}}$ and $\tilde{\mathbf{P}}$ are spatial Fourier transforms of $\mathbf{P}_{\mathit{filt}}$ and $\mathbf{P}$ respectively, and $H(K) = |K|$ is the well known "rho" filter. After filtering, the backprojection step in the spatial frequency domain is given by

$$\mathbf{f}(x,y) = \int_{0}^{\pi}\int_{-\infty}^{\infty} dK d\theta e^{iKd}\tilde{\mathbf{P}}_{\mathit{filt}}(K,\theta) \tag{2-16}$$

Here, the final reconstruction is obtained by integrating over viewing angles the filtered and backprojected data.

FBP method is commonly and successfully employed in medical imaging techniques such as computer tomography (CT) scanners of diagnostic medicine. However, when the wavelength of the insonifying source is not significantly smaller than the dimensions of the object to be imaged, the raypaths become severely distorted due to diffractions and dispersion of the wave and the FBP method is no longer a valid imaging technique. A generalization of the technique has been developed that incorporates the wavelength of the source and is called *diffraction tomography* or *filtered backpropagation* (FBProp) [12, 13].

2.2.2 Diffraction Tomography (DT)

Unlike x-rays, the longer wavelength employed in geophysical exploration using acoustic (as well as radar) waves do not travel in straight lines and that interactions of these waves with subsurface inhomogeneities produce a redistribution of wave amplitude and phase known as *diffraction*. For this reason, Devaney proposed a geophysical imaging procedure, based on the concept of structure determination in holography [60], that he called *geophysical diffraction tomography* (GDT) [13]. Thus, diffraction tomography (DT) is actually a generalization of the conventional tomography method (FBP) to incorporate wave diffraction effects. The goal in DT is to generate an exact inversion of a linearized forward model relating an unknown scatterer to scattered wavefield measurements. As discussed in the introduction, our imaging algorithm belongs to the category of GDT.

The basis for DT is the Generalized Projection Slice Theorem (GPST) [12], which is the DT generalization of the projection slice theorem of CT, relating a known function of the measured data to the spatially variable refractive index, subject to a weak scattering approximation. For a wave equation in the frequency domain (Equation (2-2)), the weak scattering approximation (Born approximation) yields its linearized version, which can also be expressed as the integral equation form

$$\mathbf{U}_s(\mathbf{r},\omega) = -k^2 \int d\boldsymbol{\xi}\mathbf{O}(\boldsymbol{\xi})\mathbf{U}_i(\boldsymbol{\xi},\omega)\mathbf{G}(\mathbf{r}-\boldsymbol{\xi},\omega) \tag{2-17}$$

where $\mathbf{G}$ is the Green's function for the scalar Helmholtz operator. It can be readily seen from Equation (2-17) that $\mathbf{U}_s$ is derived from measurement and the function $\mathbf{U}_i$ and $\mathbf{G}$ can be computed making the only unknown quantity the object profile $\mathbf{O}(\mathbf{r})$. In the form given by this equation, the desired inversion can be accomplished by *deconvolution* of the integral. This deconvolution can be achieved by representing the Green's function by its plane wave expansion[1] [36]

$$\mathbf{G}(\mathbf{r},\omega) = \frac{i}{4\pi}\int \frac{d\alpha}{\gamma(\alpha)} e^{i[\alpha\hat{x}+\gamma(\alpha)\hat{z}]\cdot\mathbf{r}} \tag{2-18}$$

where $\gamma(\alpha) = \pm\sqrt{k^2-\alpha^2}$, with the sign chosen to render $\Im[\gamma] \geq 0$. The quantity k is the wavenumber in the homogeneous background, $\hat{x}$ and $\hat{z}$ are unit vectors in the x and z directions, respectively, and measurement of $\mathbf{U}$ ($\mathbf{U}_s$) are made along a line parallel to the x-axis on the ground surface (Figure (2-2)). For receivers deployed on the line $\mathbf{r} = (l, 0)$, assuming the incident field is a plane wave propagating in the s_0 direction[2], $\mathbf{U}_i(\mathbf{r},\omega) = e^{iks_0\cdot\mathbf{r}}$, and using Weyl's expansion of the Green's function given by Equation (2-18), Equation (2-17) becomes

[1] For simplicity, we consider only the two-dimensional case. A similar plane wave expansion (Green's dyadic) can be used in the three-dimensional case.

[2] Again for simplicity, plane wave illumination is assumed. Point source/receiver illumination or beam pattern can also be used for our derivation.

$$\mathbf{U}_s(\mathbf{r},\omega) = -\frac{ik^2}{4\pi}\int \frac{d\alpha}{\gamma(\alpha)} e^{i\alpha l} \int d\boldsymbol{\xi}\mathbf{O}(\boldsymbol{\xi}) e^{-i(\alpha\hat{x}+\gamma\hat{z}-k\mathbf{s}_0)\cdot\boldsymbol{\xi}} \quad . \tag{2-19}$$

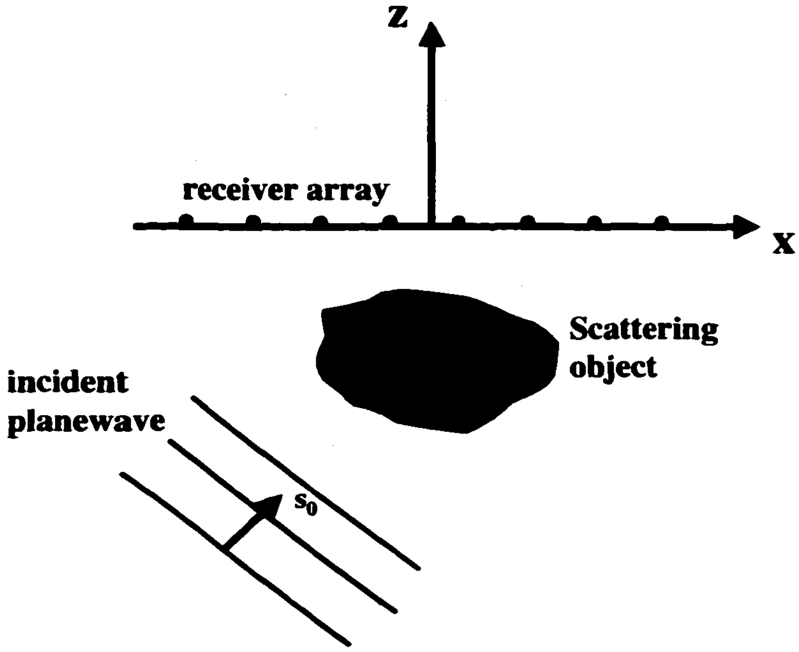

Figure 2-2: Illustration of geometry and notation used in the derivation of the GPST inversion algorithm.

The deconvolution of Equation (2-19) can be accomplished by defining the Fourier transform of the data $\mathbf{U}_s$ as

$$\tilde{\mathbf{U}}_s = \int dl e^{-i\mu l}\mathbf{U}_s \tag{2-20}$$

and applying this integral transform to Equation (2-19) gives

$$\tilde{\mathbf{U}}_s(\mu,\omega) = -\frac{ik^2}{2\gamma(\mu)} \int d\boldsymbol{\xi} \mathbf{O}(\boldsymbol{\xi}) e^{-i[\mu\hat{x}+\gamma(\mu)\hat{z}-k\mathbf{s}_0]\cdot\boldsymbol{\xi}} \tag{2-21}$$

where $\gamma(\mu) = \pm\sqrt{k^2-\mu^2}$, with the sign chosen to render $\Im[\gamma] \geq 0$. This procedure yields the final form of the GPST

$$\tilde{\mathbf{U}}_s(\mu,\omega) = -\frac{ik^2}{2\gamma(\mu)} \tilde{\mathbf{O}}(\mathbf{K}) \tag{2-22}$$

where

$$\tilde{\mathbf{O}}(\mathbf{K}) = \int d\boldsymbol{\xi} \mathbf{O}(\boldsymbol{\xi}) e^{-i\mathbf{K}\cdot\boldsymbol{\xi}} = \int d\boldsymbol{\xi} \mathbf{O}(\boldsymbol{\xi}) e^{-i[\mu\hat{x}+\gamma(\mu)\hat{z}-k\mathbf{s}_0]\cdot\boldsymbol{\xi}} \ . \tag{2-23}$$

Here, $\mathbf{K} = \mu\hat{x} + \gamma(\mu)\hat{z} - k\mathbf{s}_0 = k(\mathbf{s} - \mathbf{s}_0)$ is the wave vector variable, and $\mathbf{s}_0$ and $\mathbf{s}$ are incident and scattered wave, respectively. The desired result of an analytic expression between measurement and subsurface properties is achieved in Equation (2-22), which relates the one-dimensional Fourier transform of the scattered field to the two-dimensional Fourier transform of the object profile.

It is now possible to reconstruct the spatial variations in $\mathbf{O}$. Rewriting Equation (2-22) as

$$\tilde{\mathbf{O}}(\mathbf{K}) = \frac{2i\gamma(\mu)}{k^2} \tilde{\mathbf{U}}_s(\mu,\omega) \ , \tag{2-24}$$

then inverting the integral transform of $\mathbf{O}$ by

$$\begin{aligned}\mathbf{O}(\mathbf{r}) &= \frac{1}{(2\pi)^2}\int d\mathbf{K}\tilde{\mathbf{O}}(\mathbf{K})e^{i\mathbf{K}\cdot\mathbf{r}} \\ &= \frac{2i}{(2\pi k)^2}\int d\mathbf{K}\gamma(\mu)\tilde{\mathbf{U}}_s(\mu,\omega)e^{i[\mu\hat{x}+\gamma(\mu)\hat{z}-k\mathbf{s}_0]\cdot\mathbf{r}} \quad .\end{aligned} \tag{2-25}$$

For example, for illumination by a plane wave propagation straight down, the incident field is $\mathbf{U}_i(\mathbf{r}) = e^{-ikz}$ and the wave vector is

$$\mathbf{K} = (K_x, K_z) = (\mu, \gamma(\mu) + k) \quad . \tag{2-26}$$

Thus, we get the final form of the imaging algorithm

$$\mathbf{O}(\mathbf{r}) = \frac{i}{2\pi^2}\int \frac{dk}{k^2}\int d\mu\,[\gamma(\mu)+k]\,\tilde{\mathbf{U}}_s(\mu,\omega)e^{i\{\mu x+[\gamma(\mu)+k]z\}} \quad . \tag{2-27}$$

Imaging by means of the GPST and the transform inversion given by Equation (2-25) has become known as *diffraction tomography* (DT) and it is analogous to holographic imaging using a variety of laser beam illumination direction $\mathbf{s}_0$. The GPST, Equation (2-22), provides a knowledge of $\tilde{\mathbf{O}}$ over a wave vector space $\mathbf{K} = \mathbf{K}(\mathbf{s}_0, \mathbf{s})$. The resulting image quality will depend upon the extent of the wavenumber k and the directions spanned by both the incident wave $\mathbf{s}_0$ and the scattered wave $\mathbf{s}$. For an infinitely long receiver array and full range of view angles (0 to 2π), $\mathbf{K}$-space coverage is of a circle of radius 2k [53]. For any particular view direction, **K**-space coverage will be a portion of a circular arc [57]. As the view direction changes, a region of **K**-space is "swept" out. For any practical geophysical measurement geometry, there will necessarily be gaps in **K**-space that will introduce artifacts (blurring) into the image. The effects of measurement geometry on image quality are addressed in [13] and [50]. While the image quality will be strongly influenced by measurement geometry, in general, some elongation of the image will always occur along the dominant direction of incident wave propagation. This phenomenon also appears in our GPR imaging results using the pseudo-inverse algorithm.

The previous discussion is appropriate for wave-based methods such as seismic reflection, which typically employs independently positioned sources and receivers (multi-bistatic). In our multi-monostatic GPR survey, a collocated source/receiver pair is moved in unison. For this measurement geometry, individual incident and scattered wave directions cannot be independently controlled and, as a consequence, only a single arc in **K**-space can be realized for a particular frequency ω. Fortunately, in general, GPR systems are pulsed, offering a reasonable source bandwidth. This bandwidth can be exploited by representing the integration over **K** in Equation (2-25) as a summation over frequencies ω and an integration over the spatial Fourier transform variable μ. By this means, **K**-space coverage is a series of concentric arcs sufficient to yield good tomographic images [57].

In geophysical imaging, there have been many modifications and extensions to the application of the DT algorithm. In [13] and [61], DT has been used in various geophysical geometries, such as offset vertical seismic profile (VSP) and cross-well. GDT in a layered background has been discussed in [14]. These algorithm neglect evanescent waves and require a lossless soil model. Witten [49] investigated the influence of a number of factors on the quality of tomographic reconstructions obtained via the DT algorithm. These factors include the approximate generation of plane waves, the attenuation of high frequency components (evanescent wave), the density of receivers, the quality of the received signal, etc. The author found that the density of receivers limits the size of the smallest features that can be imaged, while the loss of evanescent wave components limits the image sharpness, and errors that can occur as a result of the approximate generation of plane waves can be overcome by an appropriate slant stack procedure. A GDT algorithm with arbitrary source illumination has been presented in [50], in which a cylindrical beam (a point source in two dimensions) illumination is implemented. GDT has also been incorporated into field instrumentation [54], and applied to problems such as the location and identification of buried waste [51], imaging the skeletal remains of a supergiant sauropod dinosaur [55], detecting tunnels in the Korean demilitarized zone [52], and quantifying the spatial extent of subterranean features at Shiqmim, Israel [58]. In these applications, the background medium is assumed to be lossless and nondispersive, and point sources/receivers are used.

Several author have addressed, within the context of DT, the problem of fully analytical inverse scattering using a multi-monostatic geometry instead of using plane wave illumination. The multi-monostatic geometry is convenient and popular in GPR imaging applications. In [39], exact inversion formulas, within the Born approximation, is derived using broadband multi-monostatic measurements conducted on planar, spherical and cylindrical surfaces. The authors use an ideal point source/receiver approximation, and assume the distance to a scattering object is much greater than a wavelength. This treatment requires transmitted pulses that are not bandlimited, however the authors suggest Wiener filtering as a means to circumvent this restriction. In [62], DT imaging methods are described using multifrequency multi-monostatic data for both constant and vertically varying backgrounds. Inversion formulas are given using both the Born and the physical optics approximations, assuming a lossless background medium. Efficient two-dimensional and three-dimensional DT imaging algorithms with scalar waves for the multi-monostatic geometry are derived in [34] and [24], respectively. In these algorithms, the derived inversion schemes have been classified as Fourier transform and far-field methods [34]. The Fourier transform method relates the spatial Fourier transform of the object profile to the spatial Fourier transform of the data as in the GPST, while the far-field method relates the transform of the object profile to the data itself. Simplifying assumptions also include weak scattering approximations, point sources/receivers and a lossless background medium.

There are some limitations of the use of these DT algorithms in GPR imaging. First, in GPR imaging, the soil attenuation effects can be significant and therefore must be incorporated to the forward scattering model. Second, most of the DT algorithms use point sources/receivers. Third, imaging blurring associated with long wavelengths can be reduced by inclusion of high spatial frequency (evanescent) components of the data. These challenges will be addressed in this thesis.

2.2.3 Algebraic Reconstruction Technique (ART)

FBP and FBProp belong to *non-iterative* methods in tomography reconstruction techniques. The *algebraic reconstruction technique* (ART) [18, 19, 20, 22, 23] and *simultaneous iterative reconstruction technique* (SIRT) [16, 17, 31] are *iterative* methods. The iterative methods generate reconstructions via an iterative process, which begins with an initial estimate of the object being reconstructed and then improves on this initial estimate via a sequence of estimates that presumably converge to an 'optimum' reconstruction after some number of iterations. ART was first employed in conventional CT, then formulated for medical and geophysical problems in DT [28, 29, 30]. The mathematical foundation of the ART algorithms is the method of Kaczmarz [25, 37], which is described briefly below.

In our tomographic imaging applications (Equation (1-1)), it is assumed that the measured data $\mathbf{g}$ can be divided into a finite number of partitions $\mathbf{g}_n \in \mathbf{U}_n, n = 1, 2, \ldots, N$, each associated with a particular experiment. Likewise, the operator $\mathcal{A}$ can be partitioned into a set of linear and continuous operators $\mathcal{A}_n$, each mapping the unknown function $\mathbf{f} \in \mathbf{V}$ into the data $\mathbf{g}_n \in \mathbf{U}_n$ from each experiment. Therefore, Equation (1-1) can be expressed as the following coupled set of linear equations [9]:

$$\begin{pmatrix} \mathbf{g}_1 \\ \mathbf{g}_2 \\ \vdots \\ \mathbf{g}_N \end{pmatrix} = \begin{pmatrix} \mathcal{A}_1 \\ \mathcal{A}_2 \\ \vdots \\ \mathcal{A}_N \end{pmatrix} \mathbf{f} \ . \tag{2-28}$$

Karzmarz's method can be used to iteratively solve the coupled set of Equation (2-28), and takes the form of the following iteration structure:

$$\mathbf{f}_{(0)} = \mathbf{f}^{(j-1)} \quad \mathrm{j} = 1, 2, ..., \mathrm{J}$$
$$\mathbf{f}_n = \mathbf{f}_{n-1} + \mathcal{A}_n^{\dagger}(\mathcal{A}_n\mathcal{A}_n^{\dagger})^{-1}(\mathbf{g}_n - \mathcal{A}_n\mathbf{f}_{n-1}) \quad \mathrm{n} = 1, 2, ..., \mathrm{N}$$
$$\mathbf{f}^{(j)} = \mathbf{f}_N$$

where J is the total number of iterations, N is the total number of experiments, $\mathbf{f}^{(0)}$ is the initial estimate, $\mathbf{f}^{(j)}$ is the intermediate approximation of $\mathbf{f}$ computed after j iterations, and $\mathcal{A}_n^{\dagger}$ is the Hermitian adjoint of $\mathcal{A}_n$. It is proven [37] that as the number of iterations $\mathrm{J} \to \infty$, $\mathbf{f}^{(J)}$ converges monotonically to a solution of Equation (2-28), if a solution exists. If Equation (2-28) is underdetermined, $\mathbf{f}^{(J)}$ converges to the solution having minimum Euclidean distance $||\mathbf{f}^{(1)} - \mathbf{f}^{(J)}||^2$ to the initial assigned value $\mathbf{f}^{(0)}$. If $\mathbf{f}^{(0)}$ is initialized as $\mathbf{f}^{(0)} = 0$, then $\mathbf{f}^{(J)}$ approaches the minimum L^2 norm solution of Equation (2-28).

The intermediate solutions $\mathbf{f}^{(j)}$ monotonically approach any solution $\hat{\mathbf{f}}$ of Equation (2-28) with increasing iterations [9]. Since $\mathcal{A}_n\hat{\mathbf{f}} = \mathbf{g}_n$ (from Equation (2-28)) and $\mathcal{A}_n\mathbf{f}_n = \mathbf{g}_n$, therefore the vector $(\hat{\mathbf{f}} - \mathbf{f}_n)$ is in the null space of $\mathcal{A}_n$. Since $\mathcal{A}_n$ is

Hermitian, it can be shown from inner product relations that any vector in the null space of $\mathcal{A}_n$ is orthogonal to any vector $(\mathcal{A}_n^\dagger \mathbf{g}_n')$, where $\mathbf{g}_n' \in \mathbf{U}_n$. Thus, $(\hat{\mathbf{f}} - \mathbf{f}_n)$ is orthogonal to

$$(\mathbf{f}_n - \mathbf{f}_{n-1}) = \mathcal{A}_n^\dagger(\mathcal{A}_n\mathcal{A}_n^\dagger)^{-1}(\mathbf{g}_n - \mathcal{A}_n\mathbf{f}_{n-1}) = \mathcal{A}_n^\dagger\mathbf{g}_n' \quad . \tag{2-29}$$

Using this orthogonal argument, we can show that the repeated iterations will successively reduce the energy of the error $\|\hat{\mathbf{f}} - \mathbf{f}_n\|^2$. Because the vector $(\hat{\mathbf{f}} - \mathbf{f}_n)$ and $(\mathbf{f}_n - \mathbf{f}_{n-1})$ are orthogonal, we can compute the inequality on the relative errors between the iterations (n-1) and n, i.e.,

$$\begin{aligned} \|\hat{\mathbf{f}} - \mathbf{f}_{n-1}\|^2 &= \|(\hat{\mathbf{f}} - \mathbf{f}_n) + (\mathbf{f}_n - \mathbf{f}_{n-1})\|^2 \\ &= \|\hat{\mathbf{f}} - \mathbf{f}_n\|^2 + \|\mathbf{f}_n - \mathbf{f}_{n-1}\|^2 \\ &\geq \|\hat{\mathbf{f}} - \mathbf{f}_n\|^2 \quad . \end{aligned} \tag{2-30}$$

Thus, the error successively decreases with each iteration, and therefore Kaczmarz's method approaches a solution $\hat{\mathbf{f}}$ of Equation (2-28).

In [28], ART has been generalized to DT within the Rytov approximation. The algorithm was shown to yield a minimum-norm solution to the limited-view problem in DT when the data are noise free and to reduce to the CT ART algorithm in the short-wavelength limit when DT is known to reduce to CT. The algorithm assumes the so-called conventional scan configuration, which employs plane wave illumination and planar measurement surfaces. The method has also been developed to cross-well geophysical tomography in [29]. Although ART can generate high-quality reconstructed images, non-iterative tomography methods, such as FBP, FBProp and pseudo-inverse imaging algorithms have the advantage of high execution speed and high-quality of reconstructions when a relatively large number of tomographic experiments are available.

SIRT is a variation of ART. When solving a system of equations in an ART-type algorithm, the solution $\mathbf{f}^{(j)}$ is updated after each iteration. In the SIRT-type methods the same guessed solution is updated by each iteration, and then all of these updated solutions are then averaged before beginning the next cycle through the set of equations. SIRT-type algorithms are ideally suited for a parallel processing machine as each iteration or equation can be handled independently and simultaneously. Making the equation solution and averaging operation in parallel could decrease the computing time significantly.

2.2.4 Synthetic Aperture Radar (SAR)

Another tomography method is *synthetic aperture radar* (SAR) which acquires broad-area imaging at high resolution from airplanes and satellites. SAR systems take advantage of the long-range propagation characteristics of radar signals and the complex information processing capability of modern digital electronics to provide high resolution imagery. SAR complements photographic and other optical imaging capabilities because of the minimum constraints of time-of-day and atmospheric conditions and because of the unique responses of terrain and cultural targets to radar frequencies.

A SAR antenna transmits pulses very rapidly. In fact, SAR is generally able to transmit several hundred pulses while its parent spacecraft passes over a particular object. Many backscattered radar responses are therefore obtained for that object. After intensive signal processing, all of those responses can be manipulated such that the resulting image looks like the data were obtained from a large, stationary antenna. The distance the spacecraft flies in synthesizing the antenna is known as the *synthetic aperture* (Figure (2-3)). A narrow synthetic beamwidth results from the relatively long synthetic aperture, which yields finer resolution than is possible from a smaller physical antenna.

The mathematical algorithms in SAR reconstruction are rather complicated. Here, we give a short description of the basic idea underlying the algorithms used in most present systems [4]. Assume in SAR imaging, an antenna (on a plane or a satellite) flies along a nominally straight track, which we will assume is along the x_2 axis (Figure (2-4)). The antenna emits pulses of EM radiation in a directed beam perpendicular to the flight track (i.e., in the x_1 direction). These waves scatter off the terrain, and the scattered waves are detected with the same antenna. The received signals are then used to produce an image of the terrain. The data depend on two variables, namely time t and position x along the x_2 axis, so we expect to be able to reconstruct

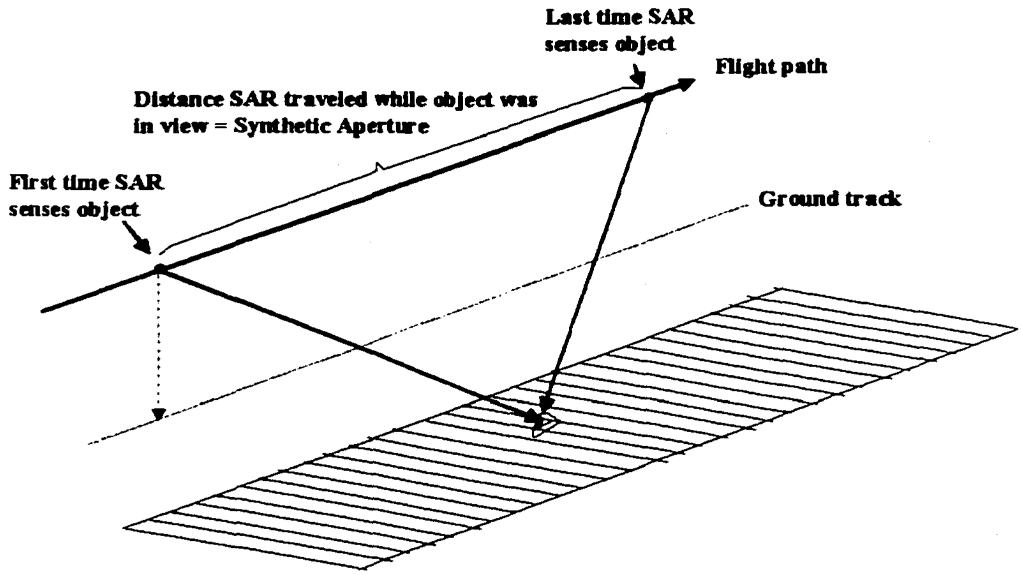

Figure 2-3: Illustration of geometry of Synthetic Aperture.

a function of two variables.

We assume that the earth is roughly situated at the plane $x_3 = 0$, and that for $x_3 > 0$, the wave speed is the speed of light in vacuum, c(x) $= c_0$. The fundamental solution of the free-space wave equation [47] is $\mathbf{G}_0(t-\tau, x-y)$, given by

$$\mathbf{G}_0(t-\tau, x-y) = \frac{\delta(t-\tau-\mid x-y\mid /c_0)}{4\pi \mid x-y \mid} \quad . \tag{2-31}$$

It has the physical interpretation of the field at (x,t) due to a delta function point source at position y and time τ. If the source signal at y has the time history of the form

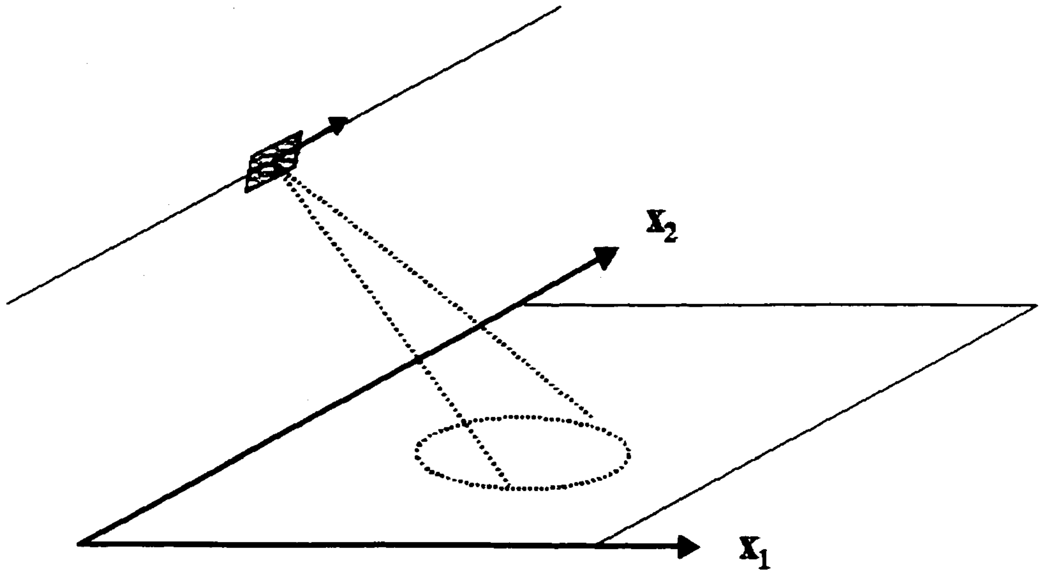

Figure 2-4: The geometry of a conventional SAR system (after Cheney, 2000)

$$P(t) = A(t)e^{i\omega_0 t} \tag{2-32}$$

where ω_0 is the angular frequency and A is a slowly varying amplitude that is allowed to be complex. The resulting field $\mathbf{U}_y(t, z-y)$ satisfies the equation

$$\left(\nabla_2 - \frac{1}{c_0^2}\partial_t^2\right)\mathbf{U}_y(t, z-y) = P(t)\delta(z-y) \tag{2-33}$$

and thus is given by

$$\mathbf{U}_y(t, z) = (\mathbf{G}_0 * P)(t, z-y) = \frac{A(t-|z-y|/c_0)}{4\pi|z-y|}e^{i\omega_0(t-|z-y|/c_0)} \quad . \tag{2-34}$$

The antenna, however, is not a point source. Most conventional SAR antennas are either slotted waveguides [11, 63], or microstrip antennas [40], and in either case, a good mathematical model is a rectangular distribution of point sources. Therefore, we denote the length and width of the antenna by L and D, respectively. We denote the center of the antenna by x; thus a point on the antenna can be written as y = x + q, where q is a vector from the center of the antenna to a point on the antenna. Define coordinates on the antenna to be q = $s_1\hat{e}_1 + s_2\hat{e}_2$, where $\hat{e}_1$ and $\hat{e}_2$ are unit vectors along the width and length of the antenna. After some approximations of series expansions ([4]), we get

$$\mathbf{U}_y(t,z) \sim \frac{P(t-|z-x|/c_0)}{4\pi|z-x|} e^{ik\widehat{z-x}\cdot q} \tag{2-35}$$

where k $= \omega_0/c_0$, and the hat denotes a unit vector. Far from the antenna, the field from the antenna is

$$\mathbf{U}_x^{in}(t,z) = \int_{-L/2}^{L/2}\int_{-D/2}^{D/2} \mathbf{U}_{x+s_1\hat{e}_1+s_2\hat{e}_2}(t,z)ds_1 ds_2 \sim \frac{P(t-|z-x|/c_0)}{4\pi|z-x|}\mathcal{W}(\widehat{z-x}) \tag{2-36}$$

where $\mathcal{W}$ is the antenna beam pattern. From classical EM scattering theory, we know that a scattering solution can be written as

$$\mathbf{U}(t,x) = \mathbf{U}^{in}(t,x) + \mathbf{U}^s(t,x) \tag{2-37}$$

where $\mathbf{U}^{in}$ is the incident field and $\mathbf{U}^s$ is the scattered field. Using the Born approximation, we get [4]

$$
\begin{aligned}
\mathbf{U}^s(t,x) &\approx \int\int \mathbf{G}_0(t-\tau, x-z)\mathbf{V}(z)\partial_\tau^2 \mathbf{U}^{in}(t,x)d\tau dx \\
&= \int \frac{\mathbf{V}(z)}{4\pi|x-z|}\partial_\tau^2 \mathbf{U}^{in}(t-|x-z|/c_0, z)dz \qquad (2\text{-}38)
\end{aligned}
$$

where $\mathbf{V}(z) = \frac{1}{c^2(z)} - \frac{1}{c_0^2}$. In the case of SAR, the antenna emits a series of fields of the form as Equation (2-36) as it moves along the flight track. In particular, we assume that the antenna is located at position x^n at time nT, then the incident field is $\mathbf{U}^{in}(\tau, z) = \sum_n \mathbf{U}_n^{in}(\tau, z)$. Substituting Equation (2-36) to Equation (2-38), we get [4]

$$
\mathbf{U}^s(t-nT, x^n) = -\int \frac{\omega_0^2 P(t-nT-2|z-x^n|/c_0)}{4\pi|z-x^n|}\frac{\mathbf{V}(z)}{4\pi|z-x^n|}\mathcal{W}(\widehat{z-x^n})dz \quad . \qquad (2\text{-}39)
$$

In Equation (2-39), we note that $2|z-x^n|/c_0$ is the two-way travel time from the center of the antenna to the point z. The factors $4\pi|z-x^n|$ in the denominator corresponds to the geometrical spreading of the spherical wave emanating from the antenna and from the point z. So, we get the forward scattering model for SAR system.

The SAR reconstruction problem is to reconstruct V from Equation (2-39). It would be a problem in integral geometry if the transmitted signal P were a delta function. Unfortunately, a delta function cannot be produced in practice. To circumvent this difficulty, SAR system use *matched filter processing* [4, 46], in which the system transmits a complex waveform and then compresses the received signal mathematically, to synthesize the response from a short pulse. Besides the standard matched filter reconstruction algorithm, a filtered backprojection scheme [38] can also be used.

SAR technology has provided terrain structural information to geologists for mineral exploration, oil spill boundaries on water to environmentalists, sea state and ice hazard maps to navigators, and reconnaissance and targeting information to military operations. There are many other applications or potential applications. Some of these, particular civilian, have not been adequately explored because lower cost electronics are just beginning to make SAR technology economical for smaller scale uses.

2.3 Pseudo-inverse Algorithm

In Equation (1-1), the pseudo-inverse of operator $\mathcal{A}$ can be defined as [3]:

- Left pseudo-inverse of $\mathcal{A}$:

$$\mathcal{A}^{\mathbf{L}} = (\mathcal{A}^{\dagger}\mathcal{A})^{-1}\mathcal{A}^{\dagger} \tag{2-40}$$

- Right pseudo inverse of $\mathcal{A}$:

$$\mathcal{A}^{\mathbf{R}} = \mathcal{A}^{\dagger}(\mathcal{A}\mathcal{A}^{\dagger})^{-1} \tag{2-41}$$

where $\mathcal{A}^{\dagger}$ is the Hermitian adjoint[3] of $\mathcal{A}$, uniquely defined by the following inner product relation [3]

$$\langle \mathcal{A}\mathbf{f}, \mathbf{g} \rangle_{\mathbf{U}} = \langle \mathbf{f}, \mathcal{A}^{\dagger}\mathbf{g} \rangle_{\mathbf{V}} \tag{2-42}$$

which holds for any $\mathbf{f} \in \mathbf{V}$ and $\mathbf{g} \in \mathbf{U}$.

---

[3]The adjoint $\mathcal{A}^{\dagger}$ is given by the complex conjugate transpose of $\mathcal{A}$. This operator is also linear and continuous and has the same norm as $\mathcal{A}$: $||\mathcal{A}^{\dagger}|| = ||\mathcal{A}||$. For example, we consider a particular example of Equation (1-1), the case of *Fredolm integral equation of the first kind* of the type

$$\mathbf{g}(x) = \int_a^b \mathcal{K}(x,y)\mathbf{f}(y)dy, \qquad c \leq x \leq d$$

which can be written in the general form

$$(\mathcal{A}\mathbf{f})(x) = \int_a^b \mathcal{K}(x,y)\mathbf{f}(y)dy, \qquad c \leq x \leq d$$

In this case, the adjoint operator is given by the equation

$$(\mathcal{A}^{\dagger}\mathbf{g})(y) = \int_c^d \mathcal{K}(x,y)^{\dagger}\mathbf{g}(x)dx, \qquad a \leq y \leq b \quad .$$

Here, we use $\mathcal{A}^-$ to represent the *pseudo-inverse*, $\mathcal{A}^- = \mathcal{A}^{\mathbf{L}} = \mathcal{A}^{\mathbf{R}}$. It is also called the *generalized* or *Moore-Penrose generalized inverse* of the linear operator $\mathcal{A}$ [3].

The solutions to ill-posed problems are unstable, since small fluctuation in the data function $\mathbf{g}$ might cause large changes in the solution $\mathbf{f}$. Our GPR imaging problem is ill-posed since it is underdetermined and sometimes singular. For underdetermined inverse problems, we have an infinite number of solutions $\mathbf{f}$ satisfying the data $\mathbf{g}$. Thus, we consider a solution that is unique in the least squares sense.

The unconstrained least squares estimate $\hat{\mathbf{f}}$ minimizes the norm

$$\mathbf{J} = \|\mathbf{g} - \mathcal{A}\hat{\mathbf{f}}\|^2 \quad . \tag{2-43}$$

A solution vector $\hat{\mathbf{f}}$ that minimizes Equation (2-43) must satisfy

$$\mathcal{A}^\dagger \mathcal{A}\hat{\mathbf{f}} = \mathcal{A}^\dagger \mathbf{g} \quad . \tag{2-44}$$

If $\mathcal{A}^\dagger \mathcal{A}$ is nonsingular, Equation (2-44) gives [3]

$$\hat{\mathbf{f}} = \mathcal{A}^- \mathbf{g} \tag{2-45}$$

as the unique least squares solution for Equation (1-1). Here, $\mathcal{A}^-$ is the pseudo-inverse of $\mathcal{A}$, $\mathcal{A}^- = (\mathcal{A}^\dagger\mathcal{A})^{-1}\mathcal{A}^\dagger = \mathcal{A}^\dagger(\mathcal{A}\mathcal{A}^\dagger)^{-1}$.

The method of pseudo-inverse solutions provides a satisfactory answer to questions of existence and uniqueness for Equation (1-1) only when the pseudo-inverse is continuous and well-conditioned. This means that the range[4] of the operator $\mathcal{A}$ is closed and the condition number[5] is not much greater than one. The method is not adequate when the pseudo-inverse is not continuous, or if continuous the condition number is too large [3]. In the first case, the pseudo-inverse solution may not exist because the data are contaminated by experimental errors; in the second case, the solution always exists but a small change in input can yield a drastic change in output. Because of these cases, *regularization* methods are introduced to obtain physically meaningful approximation of the pseudo-inverse solutions.

---

[4]The *range* of the operator $\mathcal{A}$, denoted by $\mathbf{R}(\mathcal{A})$, is the set into which $\mathcal{A}$ maps $\mathbf{V}$

$$\mathbf{R}(\mathcal{A}) = \{\mathbf{g} \in \mathbf{U} | \mathbf{g} = \mathcal{A}\mathbf{f}, \mathbf{f} \in \mathbf{V}\}$$

and therefore $\mathbf{R}(\mathcal{A})$ is the linear subspace of the exact or noise free images(data).

[5]In the case of well-posed problem, the propagation of realtive errors from the data to the solution is controlled by the *condition number*. If $\delta\mathbf{g}$ is small variation of $\mathbf{g}$ and $\delta\mathbf{f}$ the corresponding variation of $\mathbf{f} = \mathcal{A}^{-1}\mathbf{g}$, then

$$||\delta\mathbf{f}||_{\mathbf{V}}/||\mathbf{f}|| \leq cond(\mathcal{A})||\delta\mathbf{g}||_{\mathbf{U}}/||\mathbf{g}||_{\mathbf{U}}$$

where cond(A)is the *condition number* given by

$$\mathbf{cond}(\mathcal{A}) = ||\mathcal{A}||||\mathcal{A}^-|| \quad .$$

Here $||\mathcal{A}||$ and $||\mathcal{A}^{-1}$ denote the norms of the continuous operator $\mathcal{A}$ and $\mathcal{A}^{-1}$, respectively. When cond($\mathcal{A}$) is not too large, the problem Equation (1-1) is said to be *well-conditioned* and the solution *stable* with respect to small variations of the data. On the other hand, when cond($\mathcal{A}$) is very large the problem is said to be *ill-conditioned* and a small variation of the data can produce a completely different solution.

One well-known regularization method is *Tikhonov-Phillips regularization* [3, 37], which generates the following approximation solution to Equation (1-1)

$$\mathbf{f}_\beta = (\mathcal{A}^\dagger \mathcal{A} + \beta \mathcal{I})^{-1} \mathcal{A}^\dagger \mathbf{g} \tag{2-46}$$

where β is known as the *regularization parameter* and $\mathcal{I}$ is the identity operator. It is apparent that as $\beta \to 0$, the regularized solution $\mathbf{f}_\beta$ approaches the minimum norm solution $\hat{\mathbf{f}}$, which satisfies Equation (1-1). An alternate form of Tikhonov-Philips regularization is

$$\mathbf{f}_\beta = \mathcal{A}^\dagger (\mathcal{A}\mathcal{A}^\dagger + \beta \mathcal{I})^{-1} \mathbf{g} \tag{2-47}$$

Determining a good regularization parameter is one of the crucial points in the application of regularization methods. The larger the regularization parameter β, the smoother the solution, but the worse the residuals, and vice versa. Choosing an optimal β will clearly yield a well balanced compromise of a sufficiently smooth solution that satisfies the discretized integral equation. We do not discuss this matter, assuming that a good regularization parameter can be found by trial and error.

Deming [9] discussed the computational efficiency advantage of our directly analytical pseudo-inverse imaging algorithm over the other numerical matrix-based techniques based on the regularized pseudo-inverse. The author points out that the main goal of these methods is a feasible means of computing and inverting a large matrix represented, for example, by $(\mathcal{A}\mathcal{A}^\dagger + \beta\mathcal{I})$ in Equation (2-47). As we show in Equation (2-28), the matrix $\mathcal{A}$ can typically be partitioned into N submatrices $\mathcal{A}_n$, and the vector $\mathbf{g}$ can be partitioned into N sub-vectors $\mathbf{g}_n$, where N is the number of tomographic experiments. If M is the number of samples in each sub-vectors $\mathbf{g}_n$ and P is the number of pixels (or voxels) in the unknown function $\mathbf{f}$, then each submatrix $\mathcal{A}_n$ is M×P. From Equation (2-47), in order to calculate the regularized pseudo-inverse of $\mathcal{A}$ we must compute the inverse of

$$(\mathcal{A}\mathcal{A}^\dagger + \beta\mathcal{I}) = \begin{bmatrix} (\mathcal{A}_1\mathcal{A}_1^\dagger + \beta\mathcal{I}) & \mathcal{A}_1\mathcal{A}_2^\dagger & \mathcal{A}_1\mathcal{A}_3^\dagger & \cdots & \mathcal{A}_1\mathcal{A}_N^\dagger \\ \mathcal{A}_2\mathcal{A}_1^\dagger & (\mathcal{A}_2\mathcal{A}_2^\dagger + \beta\mathcal{I}) & \mathcal{A}_2\mathcal{A}_3^\dagger & \cdots & \mathcal{A}_2\mathcal{A}_N^\dagger \\ \mathcal{A}_3\mathcal{A}_1^\dagger & \mathcal{A}_3\mathcal{A}_2^\dagger & (\mathcal{A}_3\mathcal{A}_3^\dagger + \beta\mathcal{I}) & \cdots & \mathcal{A}_3\mathcal{A}_N^\dagger \\ \vdots & \vdots & \vdots & \ddots & \vdots \\ \mathcal{A}_N\mathcal{A}_1^\dagger & \mathcal{A}_N\mathcal{A}_2^\dagger & \mathcal{A}_N\mathcal{A}_3^\dagger & \cdots & (\mathcal{A}_N\mathcal{A}_N^\dagger + \beta\mathcal{I}) \end{bmatrix} \tag{2-48}$$

where each block $\mathcal{A}_n\mathcal{A}_m^\dagger$ is M×M. The total matrix will be NM×NM and full unless special techniques are employed. The calculation of each element will take $\mathcal{O}(N^2M^2P)$ complex multiplications. For example, for a two dimensional imaging problem, if N $\approx$ 100, M $\approx$ 256, P $= 256^2$, then we have to store and invert a full matrix which is NM×NM = 25,600 × 25,600, and computing all of the matrix elements will take $\mathcal{O}(N^2M^2P) = \mathcal{O}(6.55 \times 10^8)$ [9]. For three dimensional imaging problems, this number will be orders of magnitude higher. Evidently, direct matrix solutions will be computationally intense. Much of the literature on pseudo-inverse is devoted to such techniques.

In the imaging algorithm described in this thesis, our forward model is linearly transformed such that the block matrices $\mathcal{A}_n\mathcal{A}_m^\dagger$ in Equation (2-48) become diagonal [9]. Therefore, not only are there a factor of M less elements to compute, but due to its convenient form the total matrix is inverted with on the order of M^2 less multiplications. This advantage will be particularly impressive for our three dimensional imaging algorithm.

3 Pseudo-inverse Imaging for Multi-monostatic GPR Data

In this section we describe a pseudo-inverse imaging algorithm, which is an extension of the DT algorithms developed by Deming and Devaney [9, 10]. The algorithm is based on DT, which will yield quantitative underground images from multi-monostatic GPR data. Our inversion algorithm includes both point sources/receivers and the Kerns' scattering matrix simulation for the near-field characteristic of the transmitting and receiving antennas.

In section 3.1, the full derivation of the three-dimensional imaging algorithm is given. We first define the forward EM scattering model (section 3.1.1) based on vector wave equation, then give the inversion algorithm (section 3.1.2) based on fully analytical computation of the pseudo-inverse operator. In section 3.2, we give the analogous version of the two dimensional algorithm.

3.1 Three-dimensional (3-D) Pseudo-inverse Algorithm

We consider an imaging geometry for a 3-D multi-monostatic GPR survey (Figure (3-1)). By probing the earth with EM wavefields, we wish to estimate the electrical permittivity distribution in the underground region $z < 0$ from scattering field measurements at the surface $z = 0$. The incident fields are generated by a GPR system operating in pulse-echo mode. Our forward scattering models are developed here in the frequency domain, related to the time domain through the standard Fourier and inverse Fourier transform definitions[6] [9, 10].

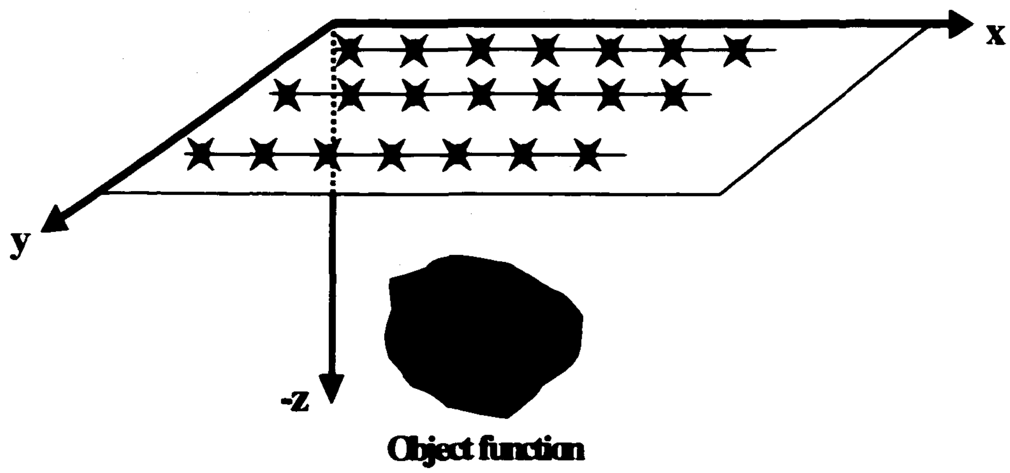

Figure 3-1: Illustration of the 3-D geometry of a multi-monostatic GPR survey. The x's and •'s represent source and receiver locations, respectively.

We assume that our GPR survey consists of a number of monostatic experiments, each corresponding to a different location of the transmitting/receiving antennas on the ground surface, and each incorporating data collected over a band of frequencies ω. In each experiment the scattering field results from the interaction of the incident field with inhomogeneities in the subsurface, described by the *object function*

$$\mathbf{O}(\mathbf{r},\omega) = 1 - \frac{\varepsilon(\mathbf{r},\omega)}{\varepsilon_0(\omega)} \quad . \tag{3-1}$$

[6] A consistent notation of Fourier and inverse Fourier transform is defined throughout our derivation. We define the Fourier transform

$$\hat{\mathbf{F}}(K) = \frac{1}{\sqrt{2\pi}} \int_{-\infty}^{\infty} dt e^{-iKt} \mathbf{F}(t)$$

and the inverse Fourier transform

$$\mathbf{F}(t) = \frac{1}{\sqrt{2\pi}} \int_{-\infty}^{\infty} dK e^{iKt} \hat{\mathbf{F}}(K) \quad .$$

Here, $\mathbf{r} = (x, y, z)$ is the 3-D spatial coordinate and $\varepsilon(\mathbf{r}, \omega) = \varepsilon'(\mathbf{r}, \omega) + i\sigma(\mathbf{r}, \omega)/\omega$ is the complex permittivity in the underground. The quantity $\varepsilon'(\mathbf{r}, \omega)$ is the real dielectric constant and $\sigma(\mathbf{r}, \omega)$ is the conductivity, while $\varepsilon_0(\omega)$ is the complex permittivity of the background soil medium. It is assumed that the magnetic permeability in the underground is equal to μ_0, the value in a vacuum.

3.1.1 Forward Model for Electromagnetic Scattering

The Fourier amplitude of the measured total electric field satisfies the well-known Lippman-Schwinger equation[5, 9, 10, 36]

$$\begin{aligned} \mathbf{E}(\mathbf{r}, \omega) &= \mathbf{E}_i(\mathbf{r}, \omega) + \mathbf{E}_s(\mathbf{r}, \omega) \\ &= \mathbf{E}_i(\mathbf{r}, \omega) - k_0^2(\omega) \int d\boldsymbol{\xi} \mathbf{G}(\mathbf{r} - \boldsymbol{\xi}, \omega) \cdot \mathbf{E}(\boldsymbol{\xi}, \omega) \mathbf{O}(\boldsymbol{\xi}, \omega) \end{aligned} \tag{3-2}$$

where $\mathbf{E}_i(\mathbf{r}, \omega)$ is the incident field, $\mathbf{E}_s(\mathbf{r}, \omega)$ is the scattered field component of the electric field vector, $k_0(\omega) = \sqrt{\omega^2 \mu_0 \varepsilon_0 + i\mu_0 \sigma \omega}$ [7] is the complex wavenumber of the background soil medium, and $\mathbf{G}(\mathbf{r}, \omega)$ is the Green's dyadic. We assume that the scattered field satisfy the Sommerfield radiation condition[36] as $|z| \to 0$, and the suitable boundary conditions[8] are also specified. In computing the scattered field we

[7]For a lossless case, we assume the conductivity of background soil medium $\sigma = 0$, thus k_0 is real, and $k_0(\omega) = \omega\sqrt{\mu_0 \varepsilon_0}$.

[8]The appropriate conditions to be imposed in this case are the continuity of $\mathbf{E}$ and $\partial \mathbf{E}/\partial z$ across the ground-air interface.

neglect the scattering effect of the ground-air interface and approximate the incident field by its infinite medium value.

In order to establish an analytical expression for the object function $\mathbf{O}$ in terms of the scattered field component of the electric field vector $\mathbf{E}_s$, we linearize Equation (3-2) by using the Born approximation[9, 10, 13, 36]. This gives

$$\mathbf{E}_s(\mathbf{r}, \omega) = -k_0^2(\omega) \int d\boldsymbol{\xi} \mathbf{G}(\mathbf{r} - \boldsymbol{\xi}, \omega) \cdot \mathbf{E}_i(\boldsymbol{\xi}, \omega) \mathbf{O}(\boldsymbol{\xi}, \omega) \quad . \tag{3-3}$$

In Equation (3-2), the scattered field $\mathbf{E}_s(\mathbf{r}, \omega)$ appears implicitly both on the left-hand side and within the $\boldsymbol{\xi}$ integration of the equation. As we introduced in Section 2.1, by using the Born approximation, the total field $\mathbf{E}(\boldsymbol{\xi}, \omega)$ within the $\boldsymbol{\xi}$ integration is replaced by the incident field $\mathbf{E}_i(\boldsymbol{\xi}, \omega)$, which is convenient for us because it allows a linear relation between the object function $\mathbf{O}(\mathbf{r}, \omega)$ and the scattered field $\mathbf{E}_s(\mathbf{r}, \omega)$. The Born approximation is a "weak scattering approximation", but we'll show in Section 4 that in GPR imaging application, it should not be overly restrictive. Our imaging algorithm is not only suitable for larger weak scatterers, but good image results are also obtained from smaller diameter strong scatterers such as metal pipes.

To incorporate the characteristics of the transmitting/receiving antenna into Equation (3-3), we first transform the equation into the spatial frequency domain, then use point source illumination or Kerns' antenna scattering matrix formulation to model the near-field characteristics of the transmitting/receiving antenna. To convert Equation

(3-3) to the spatial frequency domain, we use the spectral plane wave expansion for the Green's dyadic [5]

$$\mathbf{G}(\mathbf{r}-\boldsymbol{\xi},\omega)=\frac{i}{8\pi^2}\int_{-\infty}^{\infty}\frac{d\mathbf{K}}{\gamma(\mathbf{K},\omega)}\cdot\left[\mathcal{I}-\frac{\mathbf{k}^{+}(\omega)\cdot\mathbf{k}^{+}(\omega)}{k_0^2(\omega)}\right]\cdot e^{i\mathbf{k}^{+}(\omega)\cdot(\mathbf{r}-\boldsymbol{\xi})} \tag{3-4}$$

where $\mathbf{K}=K_x\hat{x}+K_y\hat{y}$ is the spatial frequency variable, $\mathbf{k}^{+}(\omega)=\mathbf{K}+\gamma(\mathbf{K},\omega)\hat{z}$ is the wave vector for each planewave $e^{i\mathbf{k}^{+}(\omega)\cdot(\mathbf{r}-\boldsymbol{\xi})}$ in the expansion, $\gamma(\mathbf{K},\omega)=\pm\sqrt{k_0^2(\omega)-\mathbf{K}\cdot\mathbf{K}}$ with the sign chosen to render $\Im[\gamma]\geq 0$, and $\mathcal{I}$ is the identity operator. For the matrix $\left[\mathcal{I}-\frac{\mathbf{k}^{+}(\omega)\cdot\mathbf{k}^{+}(\omega)}{k_0^2(\omega)}\right]$, if we assume that the transmitted electric field has only a $\hat{y}$ polarization, that is $\hat{\mathbf{n}}=(0,1,0)$, then

$$\begin{aligned}\hat{\mathbf{n}}\cdot\left[\mathcal{I}-\frac{\mathbf{k}^{+}(\omega)\cdot\mathbf{k}^{+}(\omega)}{k_0^2(\omega)}\right]\cdot\hat{\mathbf{n}} &= \begin{bmatrix}0&1&0\end{bmatrix}\begin{bmatrix}1&0&0\\0&1&0\\0&0&1\end{bmatrix}\begin{bmatrix}0\\1\\0\end{bmatrix}\\ &\quad-\frac{1}{k_0^2(\omega)}\begin{bmatrix}0&1&0\end{bmatrix}\begin{bmatrix}K_x^2&K_xK_y&K_x\gamma\\K_xK_y&K_y^2&K_y\gamma\\K_x\gamma&K_y\gamma&\gamma^2\end{bmatrix}\begin{bmatrix}0\\1\\0\end{bmatrix}\\ &= 1-\frac{K_y^2}{k_0^2}\ .\end{aligned} \tag{3-5}$$

If the polarization of the transmitted electric field is assumed to be $\hat{\mathbf{n}}=(1,0,0)$, then by the same derivation as Equation (3-5), we get that

$$\hat{\mathbf{n}}\cdot\left[\mathcal{I}-\frac{\mathbf{k}^{+}(\omega)\cdot\mathbf{k}^{+}(\omega)}{k_0^2(\omega)}\right]\cdot\hat{\mathbf{n}}=1-\frac{K_x^2}{k_0^2}\ . \tag{3-6}$$

In wave propagation theory, for the above plane wave expansion (Equation (3-4)), when the wave vector $\mathbf{k}^+(\omega)$ is purely real, the wave is called a *propagating* wave, whereas when $\mathbf{k}^+(\omega)$ is purely imaginary, the wave is called an *evanescent* wave, which will decay exponentially with increasing depth. We are treating both the lossless case (lossless soil background) and the lossy case (attenuating soil background) in this thesis. In the lossless case (real k_0), the above plane wave expansion includes both propagating ($|\mathbf{K}| \leq k_0$) and evanescent plane waves ($|\mathbf{K}| > k_0$). In the lossy case (complex k_0), all plane waves will have complex wave vectors. Thus, in the lossy case, the term 'evanescent' is often applied to plane waves corresponding to the range $|K| > \Re[k_0]$, in which the plane waves will decay quickest with increasing depth [9, 10]. In most GDT application, the evanescent waves are discarded [13, 34] since it is assumed that the inhomogeneity is many wave lengths deep. But for some GPR imaging application, the scatterer may be near the surface and therefore the evanescent waves may contain valuable information. Therefore, we use evanescent waves to enhance our image quality.

Substituting Equation (3-4) into Equation (3-3) and evaluating the resulting expression at $z = 0$ yields the scattered electric field at the ground surface. This expression is converted to the spatial frequency domain by Fourier transforming relative to the $\mathbf{X} = x\hat{x} + y\hat{y}$ coordinate to obtain

$$
\begin{aligned}
\tilde{\mathbf{E}}_s(\mathbf{K},\omega) &= \frac{1}{(2\pi)^2}\int_{-\infty}^{\infty} d\mathbf{X} e^{-i\mathbf{K}\cdot\mathbf{X}} \left[\mathbf{E}_s(\mathbf{r},\omega)\right]_{z=0} \\
&= \frac{-ik_0^2(\omega)}{8\pi^2\gamma(\mathbf{K},\omega)}\int_{z'<0} d\boldsymbol{\xi} e^{-i\mathbf{k}^+(\omega)\cdot\boldsymbol{\xi}} \cdot \left[\mathcal{I} - \frac{\mathbf{k}^+(\omega)\cdot\mathbf{k}^+(\omega)}{k_0^2(\omega)}\right]\cdot \mathbf{E}_i(\boldsymbol{\xi},\omega)\mathbf{O}(\boldsymbol{\xi},\omega)
\end{aligned} \tag{3-7}
$$

and then we use ideal point source/receiver illumination or the Kerns' antenna scattering matrix formulation [9, 10, 27] to model the near-field interactions between antennas and scatterers.

Point Source Illumination

For point sources deployed on the ground surface $\mathbf{X}_0 = x_0\hat{x}+y_0\hat{y}$, the incident electric field propagating in the negative $\hat{z}$-direction is given by

$$
\begin{aligned}
\mathbf{E}_i(\boldsymbol{\xi},\omega) &= G(\boldsymbol{\xi}-\mathbf{X}_0,\omega) \\
&= i\int \frac{d\mathbf{K}_0}{\gamma(\mathbf{K}_0,\omega)} e^{i\mathbf{k}_0^-(\omega)\cdot(\boldsymbol{\xi}-\mathbf{X}_0)}
\end{aligned} \tag{3-8}
$$

where $\mathbf{K}_0 = K_{0x}\hat{x}+K_{0y}\hat{y}$, $\mathbf{k}_0^-(\omega) = \mathbf{K}_0-\gamma(\mathbf{K}_0,\omega)\hat{z}$, and $\gamma(\mathbf{K}_0,\omega) = \pm\sqrt{k_0^2(\omega)-\mathbf{K}_0\cdot\mathbf{K}_0}$ with the sign chosen to render $\Im[\gamma] \geq 0$.

If we assume that the inhomogeneity is dispersionless[9], we can express the object function as $\mathbf{O}(\mathbf{r}, \omega) = \mathbf{O}(\mathbf{r})$. Substituting Equation (3-8) into Equation (3-7), we get

$$\begin{aligned} \tilde{\mathbf{E}}_s(\mathbf{K}, \omega) &= \frac{k_0^2(\omega)}{8\pi^2 \gamma(\mathbf{K}, \omega)} \cdot \left[\mathcal{I} - \frac{\mathbf{k}^+(\omega) \cdot \mathbf{k}^+(\omega)}{k_0^2(\omega)} \right] \int \frac{d\mathbf{K}_0 e^{-i\mathbf{K}_0 \cdot \mathbf{X}_0}}{\gamma(\mathbf{K}_0, \omega)} \\ & \int_{-\infty}^{0} dz' e^{-i[\gamma(\mathbf{K},\omega)+\gamma(\mathbf{K}_0,\omega)]z'} \int_{-\infty}^{\infty} d\mathbf{X}' e^{-i(\mathbf{K}-\mathbf{K}_0)\cdot \mathbf{X}'} \mathbf{O}(\boldsymbol{\xi}) \ . \end{aligned} \tag{3-9}$$

We make the change of variables $\bar{\mathbf{K}} = \mathbf{K} - \mathbf{K}_0$, then dropping the bar notation on $\bar{\mathbf{K}}$ to get

$$\begin{aligned} \tilde{\mathbf{E}}_s(\mathbf{K}+\mathbf{K}_0, \omega) &= \mathcal{P}(\omega) \int d\mathbf{K}_0 \mathcal{B}(\mathbf{K}+\mathbf{K}_0, \mathbf{K}_0; \omega) \\ & \int_{-\infty}^{0} dz' e^{-i[\gamma(\mathbf{K}+\mathbf{K}_0,\omega)+\gamma(\mathbf{K}_0,\omega)]z'} \int_{-\infty}^{\infty} d\mathbf{X}' e^{-i\mathbf{K}\cdot\mathbf{X}'} \mathbf{O}(\boldsymbol{\xi}) \end{aligned} \tag{3-10}$$

where

$$\mathcal{P}(\omega) = \frac{k_0^2(\omega)}{8\pi^2} \tag{3-11}$$

and

[9] This assumption allows us to couple the measured data at each frequency, thus, incorporating more information into the mathematical inversions and leading to better solutions for the object function. Deming [9, 10] discusses the alternatives, including: (i)solve for the frequency dependent object function $\mathbf{O}(\mathbf{r}, \omega)$ independently at each single radar frequency; (ii)treat the object function as the product of a known frequency dependent factor $\Theta(\omega)$ and an unknown frequency independent factor $\mathbf{O}(\mathbf{r})$.

$$\mathcal{B}(\mathbf{K}, \mathbf{K}_0; \omega) = \frac{e^{-i\mathbf{K}_0 \cdot \mathbf{X}_0}}{\gamma(\mathbf{K}, \omega)\gamma(\mathbf{K}_0, \omega)} \cdot \left[\mathcal{I} - \frac{\mathbf{k}^+(\omega) \cdot \mathbf{k}^+(\omega)}{k_0^2(\omega)}\right] \tag{3-12}$$

It is assumed that, in a three dimensional GPR survey, the data is stored from N different excitation frequencies ω_n for each monostatic experiment. Thus, the forward model in the spatial frequency domain using ideal point source illumination for multi-monostatic measurements is

$$\begin{aligned} \tilde{\mathbf{E}}_s(\mathbf{K}+\mathbf{K}_0, \omega_n) &= \mathcal{P}(\omega_n) \int d\mathbf{K}_0 \mathcal{B}(\mathbf{K}+\mathbf{K}_0, \mathbf{K}_0; \omega_n) \\ & \int_{-\infty}^{0} dz' e^{-i[\gamma(\mathbf{K}+\mathbf{K}_0,\omega_n)+\gamma(\mathbf{K}_0,\omega_n)]z'} \int_{-\infty}^{\infty} d\mathbf{X}' e^{-i\mathbf{K}\cdot\mathbf{X}'} \mathbf{O}(\boldsymbol{\xi}) \end{aligned} \tag{3-13}$$

Kerns' Scattering Matrix Model

In a multi-monostatic GPR survey, a single transmitter and receiver are moved as a fixed unit over the ground surface. The incident field in each monostatic measurement is generated from a single transmitting antenna. Kerns' scattering matrix formulation [27] allows the simulation of the beam pattern of a transmitting/receiving antenna pair. Using Kerns' scattering model, a transmitting antenna centered at a position $\mathbf{X}_0 = x_0\hat{x} + y_0\hat{y}$ on the ground surface and driven by matched terminal voltage $C(\omega)$ will give rise to the following plane wave expansion for the incident electric field propagating in the negative $\hat{z}$-direction [9, 10]

$$\mathbf{E}_i(\mathbf{r},\omega) = C(\omega)\int_{-\infty}^{\infty} d\mathbf{K}_0 e^{-i\mathbf{K}_0\cdot\mathbf{X}_0}\mathbf{S}_{10}(\mathbf{K}_0,\omega)e^{i\mathbf{k}_0^-(\omega)\cdot\mathbf{r}} \tag{3-14}$$

where $\mathbf{S}_{10}$ is off-diagonal scattering matrix coefficient for the transmitting antenna, and is given by

$$\mathbf{S}_{10}(\mathbf{K},\omega) = \frac{e^{-a(\omega)\mathbf{K}\cdot\mathbf{K}}}{\gamma(\mathbf{K},\omega)} \tag{3-15}$$

where $a(\omega)$ is chosen such that $e^{-a(\omega)[\Re(k_0)]^2} \approx \frac{1}{10}$[9, 10]. This coefficient weights the direction components of the plane wave expansion given by Equation (3-4). By using this expansion (Equation (3-14)), the point source approximation needs not to be made.

Similarly, the matched terminal voltage at a receiver centered at the spatial coordinate $\mathbf{X}_0$ is given by [9, 10, 27]

$$\mathbf{V}(\omega;\mathbf{X}_0) = \int_{-\infty}^{\infty} d\mathbf{K}e^{i\mathbf{K}\cdot\mathbf{X}_0}\mathbf{S}_{01}(\mathbf{K},\omega)\tilde{\mathbf{E}}_s(\mathbf{K},\omega) \tag{3-16}$$

where S_{01} is an off-diagonal scattering matrix coefficient for the receiving antenna. If the transmitting and receiving antemmas are reciprocal, as would be the case for a typical monostatic radar system [9, 10, 27],

$$Y_0(\omega)\mathbf{S}_{01}(\mathbf{K},\omega) = \frac{\gamma(\mathbf{K},\omega)}{\omega\mu_0}\mathbf{S}_{10}(-\mathbf{K},\omega) \tag{3-17}$$

where μ_0 is the background magnetic permeability and Y_0 is the antenna terminal admittance.

Combining Equation (3-7), Equation (3-14), Equation (3-16) and Equation (3-17) and also assuming a dispersionless object such as the case in ideal point source illumination, gives

$$\begin{aligned} \mathbf{V}(\omega;\mathbf{X}_0) &= \mathcal{P}(\omega)\int_{-\infty}^{\infty} d\mathbf{K}\int_{-\infty}^{\infty} d\mathbf{K}_0 e^{-i(\mathbf{K}_0-\mathbf{K})\cdot\mathbf{X}_0}\mathcal{B}(\mathbf{K},\mathbf{K}_0;\omega) \\ &\quad \int_{-\infty}^{0} dz' e^{i[\gamma(\mathbf{K},\omega)+\gamma(\mathbf{K}_0,\omega)]z'}\int_{-\infty}^{\infty} d\mathbf{X}' e^{-i(\mathbf{K}-\mathbf{K}_0)\cdot\mathbf{X}'}\tilde{\mathbf{O}}(\boldsymbol{\xi}) \end{aligned} \tag{3-18}$$

where

$$\mathcal{P}(\omega) = \frac{-iC(\omega)k_0^2(\omega)}{8\pi^2\omega Y_0(\omega)\mu_0} \tag{3-19}$$

and

$$\mathcal{B}(\mathbf{K},\mathbf{K}_0;\omega) = \mathbf{S}_{10}(-\mathbf{K},\omega)\cdot\left[\mathcal{I} - \frac{\mathbf{k}^+(\omega)\cdot\mathbf{k}^+(\omega)}{k_0^2(\omega)}\right]\cdot\mathbf{S}_{10}(\mathbf{K}_0,\omega) \quad . \tag{3-20}$$

Assume that in a three dimensional GPR survey, a series of monostatic experiments are performed over the ground surface at evenly spaced locations corresponding to points on a two dimensional grid, and the data is stored from N different excitation frequencies ω_n for each monostatic experiment. If the grid spacing is small enough to satisfy the Nyquist sampling criterion for the voltage measurements, the transmitter/receiver position can be treated as a continuous variable $\mathbf{X} = (x, y)$ and then, Equation (3-18) becomes

$$\begin{aligned} \mathbf{V}(\omega_n; \mathbf{X}) &= \mathcal{P}(\omega_n) \int_{-\infty}^{\infty} d\mathbf{K} \int_{-\infty}^{\infty} d\mathbf{K}_0 e^{-i(\mathbf{K}_0 - \mathbf{K})\cdot\mathbf{X}} \mathcal{B}(\mathbf{K}, \mathbf{K}_0; \omega_n) \\ & \quad \int_{-\infty}^{0} dz' e^{i[\gamma(\mathbf{K},\omega_n) + \gamma(\mathbf{K}_0,\omega_n)]z'} \int_{-\infty}^{\infty} d\mathbf{X}' e^{-i(\mathbf{K}-\mathbf{K}_0)\cdot\mathbf{X}'} \tilde{\mathbf{O}}(\boldsymbol{\xi}). \end{aligned} \quad (3\text{-}21)$$

By changing variables $\bar{\mathbf{K}} = \mathbf{K} - \mathbf{K}_0$, dropping the bar notation on $\bar{\mathbf{K}}$, and spatially Fourier transforming Equation (3-21) with respect to the $\mathbf{X}$ variable, we obtain

$$\begin{aligned} \tilde{\mathbf{V}}(\omega_n; \mathbf{K}) &= \frac{1}{2\pi^2} \int_{-\infty}^{\infty} d\mathbf{X} e^{-i\mathbf{K}\cdot\mathbf{X}} \mathbf{V}(\omega_n; \mathbf{X}) \\ &= \mathcal{P}(\omega_n) \int_{-\infty}^{\infty} d\mathbf{K}_0 \mathcal{B}(\mathbf{K} + \mathbf{K}_0, \mathbf{K}_0; \omega_n) \\ & \quad \int_{-\infty}^{0} dz' e^{i[\gamma(\mathbf{K}+\mathbf{K}_0,\omega_n) + \gamma(\mathbf{K}_0,\omega_n)]z'} \int_{-\infty}^{\infty} d\mathbf{X}' e^{-i\mathbf{K}\cdot\mathbf{X}'} \tilde{\mathbf{O}}(\boldsymbol{\xi}). \end{aligned} \quad (3\text{-}22)$$

Hence, we get the forward scattering model (Equation (3-22)) in the spatial frequency domain using Kerns' scattering matrix model for multi-monostatic measurements.

3.1.2 Inversion Algorithm

Since the forward scattering models using ideal point source illumination (Equation (3-13)) and using Kerns' scattering matrix formulation (Equation (3-22)) have the same mathematical formalism, the pseudo-inverse algorithm can be applied to both cases in the same way. Here, we only give the brief derivation of the inversion algorithm for the forward scattering model using Kerns' scattering matrix formulation, the reader is referred to [9, 10] for the full derivation.

In order to use the regularized pseudo-inverse method to solve the unknown object function, first, define Hilbert spaces $\mathbf{U}$ and $\mathbf{Y}$ for the object function $\mathbf{O}(\mathbf{r})$ and the transformed measured terminal voltage $\tilde{\mathbf{V}}(\omega_n;\mathbf{K})$ respectively. The standard $\mathbf{L}^2$-inner products can be employed in both spaces. We also assume that the elements of each space have finite $\mathbf{L}^2$-norms[10] Then, Equation (3-22) can be expressed in the compact mathematical operator form

$$\tilde{\mathbf{V}}(\omega_n;\mathbf{K}) = \mathcal{A}\mathbf{O}(\omega_n;\mathbf{K}) \tag{3-23}$$

where $\mathcal{A}$ is a linear operator which maps $\mathbf{U}$ into $\mathbf{Y}$.

[10]This means that [9, 10]

- $\mathbf{O}(\mathbf{r}) \in \mathbf{U}$, where $\mathbf{U}$ is the space of square integrable functions defined on $-\infty < (x, y) < \infty, -\infty < z < 0$;
- $\tilde{\mathbf{V}}(\omega_n;\mathbf{K}) \in \mathbf{Y}$, where $\mathbf{Y}$ is the direct product space of square integrable function on $-\infty < (K_x, K_y) < \infty$ with the finite dimensional vector space $\mathbf{Y}_0$ of functions of the discrete variable ω_n.

By using the regularized pseudo-inverse operator, we get the minimum $\mathbf{L}^2$-norm solution for the object function $\mathbf{O}(\mathbf{r})$ [3, 9, 10, 37]

$$
\begin{aligned}
\hat{\mathbf{O}}_\beta &= \mathcal{A}^\dagger(\mathcal{A}\mathcal{A}^\dagger + \beta\mathcal{I})^{-1}\tilde{\mathbf{V}} \\
&= \mathcal{A}^\dagger\tilde{\mathbf{V}}_{filt} \qquad (3\text{-}24)
\end{aligned}
$$

where $\mathcal{A}^\dagger$ is the Hermitian adjoint of $\mathcal{A}$, β is the Tikhonov-Phillips regularization parameter[11], $\mathcal{I}$ is the identity operator, and $\tilde{\mathbf{V}}_{filt} = (\mathcal{A}\mathcal{A}^\dagger + \beta\mathcal{I})^{-1}\tilde{\mathbf{V}}$ is referred to as the *filtered data* [9, 10].

By using the property of adjoint operators[12], we get the inverse of filtering operator

$$
\begin{aligned}
\tilde{\mathbf{V}}(\omega_m; \mathbf{K}) &= (\mathcal{A}\mathcal{A}^\dagger + \beta\mathcal{I})\tilde{\mathbf{V}}_{filt}(\omega_m; \mathbf{K}) \\
&= \sum_{n=1}^{N} \mathbf{Q}_{mn}(\mathbf{K})\tilde{\mathbf{V}}_{filt}(\omega_n; \mathbf{K}) + \beta\tilde{\mathbf{V}}_{filt}(\omega_m; \mathbf{K}) \qquad (3\text{-}26)
\end{aligned}
$$

where N is the total number of the experiments; and

[11]Generally, there is a tradeoff between selecting β small enough such that $\hat{\mathbf{O}}_\beta$ approximately satisfies the data yet large enough that the solution is stable, and typically β is selected by trial and error.

[12]Given the vector space definitions, the Hermitian adjoint $\mathcal{A}^\dagger$ of $\mathcal{A}$ maps the space $\mathbf{Y}$ onto the space $\mathbf{U}$ so that we have the inner product relation

$$
\langle \mathcal{A}\mathbf{O}_\beta, \tilde{\mathbf{V}}\rangle_{\mathbf{Y}} = \langle \mathbf{O}_\beta, \mathcal{A}^\dagger\tilde{\mathbf{V}}\rangle_{\mathbf{U}} \quad . \qquad (3\text{-}25)
$$

$$\mathbf{Q}_{mn}(\mathbf{K}) = \int_{-\infty}^{\infty} d\mathbf{K}_0 \int_{-\infty}^{\infty} d\mathbf{K}_0' \frac{4i\pi^2 \mathcal{P}(\omega_m)\mathcal{P}^*(\omega_n)\mathcal{B}(\mathbf{K}+\mathbf{K}_0, \mathbf{K}_0; \omega_m)\mathcal{B}^*(\mathbf{K}+\mathbf{K}_0', \mathbf{K}_0'; \omega_n)}{\gamma(\mathbf{K}+\mathbf{K}_0, \omega_m) + \gamma(\mathbf{K}_0, \omega_m) - \gamma^*(\mathbf{K}+\mathbf{K}_0', \omega_n) - \gamma^*(\mathbf{K}_0', \omega_n)}$$

the * denotes the complex conjugate.

Equation (3-26) can be written in block matrix notation

$$\begin{bmatrix} \tilde{\mathbf{V}}(\mathbf{K};\omega_1) \\ \tilde{\mathbf{V}}(\mathbf{K};\omega_2) \\ \vdots \\ \tilde{\mathbf{V}}(\mathbf{K};\omega_N) \end{bmatrix} = \begin{bmatrix} \mathbf{Q}_{11}(\mathbf{K})+\beta & \mathbf{Q}_{12}(\mathbf{K}) & \dots & \mathbf{Q}_{1N}(\mathbf{K}) \\ \mathbf{Q}_{21}(\mathbf{K}) & \mathbf{Q}_{22}(\mathbf{K})+\beta & \dots & \mathbf{Q}_{2N}(\mathbf{K}) \\ \vdots & \vdots & \ddots & \vdots \\ \mathbf{Q}_{N1}(\mathbf{K}) & \mathbf{Q}_{N2}(\mathbf{K}) & \dots & \mathbf{Q}_{NN}(\mathbf{K})+\beta \end{bmatrix} \begin{bmatrix} \tilde{\mathbf{V}}_{filt}(\mathbf{K};\omega_1) \\ \tilde{\mathbf{V}}_{filt}(\mathbf{K};\omega_2) \\ \vdots \\ \tilde{\mathbf{V}}_{filt}(\mathbf{K};\omega_N) \end{bmatrix} \tag{3-27}$$

which can be inverted by Gaussian elimination, Cramer's rule, or other methods in linear algebra to yield the filtered data $\tilde{\mathbf{V}}_{filt}$ in terms of the raw, unfiltered data $\tilde{\mathbf{V}}$.

Then the final form of the imaging algorithm can be established by expressing $\mathbf{O}$ as a function of the filtered data $\tilde{\mathbf{V}}_{filt}$ [9, 10]

$$\begin{aligned} \hat{\mathbf{O}}_\beta(\boldsymbol{\xi}) &= \mathcal{A}^\dagger \tilde{\mathbf{V}}_{filt}(\boldsymbol{\xi}) \\ &= \sum_{n=1}^{N} \mathcal{P}^*(\omega_n) \int_{-\infty}^{\infty} d\mathbf{K}' \int_{-\infty}^{\infty} d\mathbf{K}_0' \mathcal{B}^*(\mathbf{K}'+\mathbf{K}_0', \mathbf{K}_0'; \omega_n) \\ &\quad e^{i\left[\gamma^*(\mathbf{K}'+\mathbf{K}_0', \omega_n)+\gamma^*(\mathbf{K}_0', \omega_n)\right]z'} e^{i\mathbf{K}'\cdot\mathbf{X}'} \tilde{\mathbf{V}}_{filt}(\mathbf{K}'; \omega_n) \end{aligned} \tag{3-28}$$

where $\boldsymbol{\xi} = (\mathbf{X}', z')$.

3.2 Two-Dimensional (2-D) Pseudo-inverse Algorithm

The 2-D case corresponds to the situation in which a coordinate system is defined by $\hat{x}$-axis representing the ground surface, and $\hat{z}$-axis pointing vertically upward (Figure (3-2)). The 2-D object function $\mathbf{O}(x, z)$ is assumed to be invariant in the $\hat{y}$-direction. We can treat the 2-D imaging problem in a manner completely analogous to the 3-D case. In the 3-D case, a series of monostatic experiments are conducted over a two-dimensional grid on the xy plane; whereas in 2-D case, we conduct the experiments at intervals along a line corresponding to the $\hat{x}$-axis. We also wish to reconstruct the object function from the scattered field measurement.

3.2.1 Forward Model for Electromagnetic Scattering

By using the Born approximation, we get the scattered field component of the electric field vector

$$\mathbf{E}_s(\mathbf{r}, \omega) = -k_0^2(\omega) \int d\boldsymbol{\xi} \mathbf{G}(\mathbf{r} - \boldsymbol{\xi}, \omega) \cdot \mathbf{E}_i(\boldsymbol{\xi}, \omega) \mathbf{O}(\boldsymbol{\xi}, \omega) \tag{3-29}$$

where $\mathbf{r} = (x, z)$ is the two-dimensional spatial coordinate. In our 2-D imaging problems, we assume that the transmitted electric field has only a $\hat{y}$ polarization, and

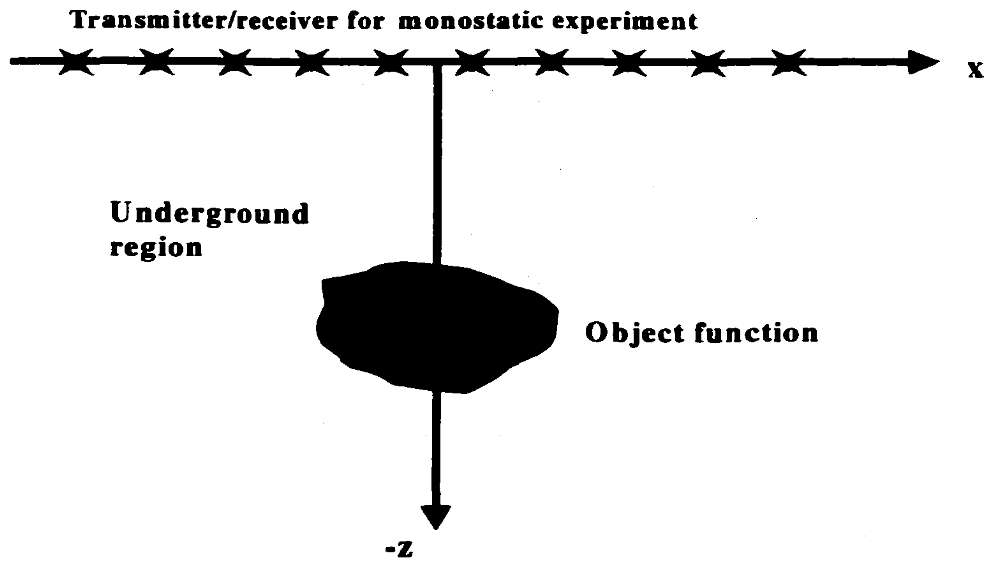

Figure 3-2: Illustration of the 2-D geometry of multi-monostatic GPR survey.

the antennas and scatterers do not vary in the $\hat{y}$ direction, so that the Equation (3-4) becomes the scalar spectral plane wave expansions for the Green's function[13]

$$\mathbf{G}(\mathbf{r}-\boldsymbol{\xi},\omega) = \frac{i}{8\pi^2}\int_{-\infty}^{\infty}\frac{d\mathbf{K}}{\gamma(\mathbf{K},\omega)}e^{i\mathbf{k}^{+}(\omega)\cdot(\mathbf{r}-\boldsymbol{\xi})} \tag{3-30}$$

where $\mathbf{K} = K_x\hat{x}$ is the spatial frequency variable. Substituting Equation (3-30) into Equation (3-29) and evaluating the resulting expression at $z = 0$ yields the scattered electric field at the ground surface. This expression is converted to the spatial frequency domain by Fourier transforming relative to the $\mathbf{X} = x\hat{x}$ coordinate to obtain

[13]This means in Equation (3-5), $K_y = 0$.

$$
\begin{aligned}
\tilde{\mathbf{E}}_s(K_x,\omega) &= \frac{1}{2\pi}\int_{-\infty}^{\infty} dx e^{-iK_x x}\left[\mathbf{E}_s(\mathbf{r},\omega)\right]_{z=0} \\
&= \frac{-ik_0^2(\omega)}{8\pi^2\gamma(K_x,\omega)}\int_{z'<0} d\boldsymbol{\xi} e^{-i\mathbf{k}^+(\omega)\cdot\boldsymbol{\xi}}\mathbf{E}_i(\boldsymbol{\xi},\omega)\mathbf{O}(\boldsymbol{\xi},\omega). \qquad (3\text{-}31)
\end{aligned}
$$

If we use *ideal point source illumination*, for point sources deployed on the line $\mathbf{X}_0 = (x_0, 0)$,

$$
\begin{aligned}
\mathbf{E}_i(\boldsymbol{\xi},\omega) &= \mathbf{G}(\boldsymbol{\xi}-\mathbf{X}_0,\omega) \\
&= i\int \frac{d\mathbf{K}_0}{\gamma(\mathbf{K}_0,\omega)} e^{i\mathbf{k}_0^-(\omega)\cdot(\boldsymbol{\xi}-\mathbf{X}_0)} \qquad (3\text{-}32)
\end{aligned}
$$

where $\mathbf{K}_0 = K_{0x}\hat{x}$. By methods similar to the three-dimensional analysis, assume for each monostatic experiment, the data is stored from N different excitation frequencies ω_n, and substituting Equation (3-32) into Equation (3-31), making the change of variables $\bar{K_x} = K_x - K_{0x}$, then dropping the bar notation on $\bar{K_x}$ yields

$$
\begin{aligned}
\tilde{\mathbf{E}}_s(K_x+K_{0x},\omega_n) &= \mathcal{P}(\omega_n)\int dK_{0x}\mathcal{B}(K_x+K_{0x}, K_{0x};\omega_n) \\
&\quad \int_{-\infty}^{0} dz' e^{-i[\gamma(K_x+K_{0x},\omega_n)\gamma(K_{0x},\omega_n)]z'} \\
&\quad \int_{-\infty}^{\infty} dx' e^{-iK_x x'} O(x',z') \qquad (3\text{-}33)
\end{aligned}
$$

where

$$\mathcal{P}(\omega_n) = \frac{k_0^2(\omega_n)}{8\pi^2} \tag{3-34}$$

and

$$\mathcal{B}(K_x, K_{0x}; \omega_n) = \frac{e^{-iK_{0x}X_0}}{\gamma(K_x, \omega_n)\gamma(K_{0x}, \omega_n)} \quad . \tag{3-35}$$

Thus, Equation (3-33) is a forward model in the spatial frequency domain using ideal point source illumination for 2-D multi-monostatic measurements.

Using *Kerns' scattering matrix model*, we assume the interval spacing along the $\hat{x}$-axis is small enough to satisfy the Nyquist sampling criterion for the voltage measurements, thus we can treat the measured voltage $\mathbf{V}(\omega_n; x)$ as a function of continuous variable x. By methods similar to the three-dimensional case, the data are defined as the spatial Fourier transform relative to the x coordinate of the measured voltage:

$$\begin{aligned}\tilde{\mathbf{V}}(\omega_n; K_x) &= \frac{1}{2\pi}\int_{-\infty}^{\infty} dx e^{-iK_x x}\mathbf{V}(\omega_n; \mathbf{X}) \\ &= 2\pi\mathcal{P}(\omega_n)\int_{-\infty}^{\infty} dK_{0x}\mathcal{B}(K_x + K_{0x}, K_{0x}; \omega_n) \\ &\quad \int_{-\infty}^{0} dz' e^{i[\gamma(K_x+K_{0x},\omega_n)+\gamma(K_{0x},\omega_n)]z'}\int_{-\infty}^{\infty} dx' e^{-iK_x x'}\tilde{\mathbf{O}}(x', z')\end{aligned} \tag{3-36}$$

where

$$\mathcal{P}(\omega_n) = \frac{-iC(\omega_n)k_0^2(\omega_n)}{8\pi^2\omega_n Y_0(\omega_n)\mu_0} \tag{3-37}$$

and

$$\mathcal{B}(K_x, K_{0x}; \omega_n) = \mathbf{S}_{10}(-K_x, \omega_n)\mathbf{S}_{10}(K_{0x}, \omega_n) \ . \tag{3-38}$$

Thus, Equation (3-36) is a forward model in the spatial frequency domain using Kerns' scattering matrix formulation for 2-D multi-monostatic measurements.

3.2.2 Inversion Algorithm

Here we also use the Hilbert space definitions[14] for $\mathbf{O}(x, z)$ and $\tilde{\mathbf{V}}(\omega_n; K_x)$. The regularized pseudo-inverse solution for the object function is

$$\begin{aligned} \hat{\mathbf{O}}_\beta(x, z) &= \mathcal{A}^\dagger(\mathcal{A}\mathcal{A}^\dagger + \beta\mathcal{I})^{-1}\tilde{\mathbf{V}}(x, z) \\ &= \mathcal{A}^\dagger\tilde{\mathbf{V}}_{filt}(x, z) \end{aligned} \tag{3-39}$$

[14]This means that [9, 10]

- $\mathbf{O}(x, z) \in \mathbf{W}$, where $\mathbf{W}$ is the space of square integrable functions on $-\infty < x < \infty$, $-\infty < z < 0$;
- $\tilde{\mathbf{V}}(\omega_n; K_x) \in \mathbf{Z}$, where $\mathbf{Z}$ is the direct product space of square integrable functions on $-\infty < K_x < \infty$ with the finite-dimensional vector space $\mathbf{Y}_0$ of functions of the discrete variable ω_n;
- $\mathcal{A}$ is a linear operator which maps $\mathbf{W}$ into $\mathbf{Z}$.

The relation between the filtered data $\tilde{\mathbf{V}}_{filt}(\omega; K_x)$ and unfiltered data $\tilde{\mathbf{V}}(\omega; K_x)$ is

$$\begin{aligned}\tilde{\mathbf{V}}(\omega_m; K_x) &= (\mathcal{A}\mathcal{A}^\dagger + \beta\mathcal{I})\tilde{\mathbf{V}}_{filt}(\omega_m; K_x) \\ &= \sum_{n=1}^{N} \mathbf{Q}_{mn}(K_x)\tilde{\mathbf{V}}_{filt}(\omega_n; K_x) + \beta\tilde{\mathbf{V}}_{filt}(\omega_m; K_x) \qquad (3\text{-}40)\end{aligned}$$

where

$$\mathbf{Q}_{mn}(K_x) = \int_{-\infty}^{\infty} dK_{0x} \int_{-\infty}^{\infty} dK'_{0x} \frac{8i\pi^3\mathcal{P}(\omega_m)\mathcal{P}^*(\omega_n)\mathcal{B}(K_x + K_{0x}, K_{0x}; \omega_m)\mathcal{B}^*(K_x + K'_{0x}, K'_{0x}; \omega_n)}{\gamma(K_x + K_{0x}, \omega_m) + \gamma(K_{0x}, \omega_m) - \gamma^*(K_x + K'_{0x}, \omega_n) - \gamma^*(K'_{0x}, \omega_n)} .$$

For each value of K_x, Equation (3-41) can be written in the matrix notation

$$\begin{bmatrix} \tilde{\mathbf{V}}(K_x; \omega_1) \\ \tilde{\mathbf{V}}(K_x; \omega_2) \\ \vdots \\ \tilde{\mathbf{V}}(K_x; \omega_N) \end{bmatrix} = \begin{bmatrix} \mathbf{Q}_{11}(K_x) + \beta & \mathbf{Q}_{12}(K_x) & \cdots & \mathbf{Q}_{1N}(K_x) \\ \mathbf{Q}_{21}(K_x) & \mathbf{Q}_{22}(K_x) + \beta & \cdots & \mathbf{Q}_{2N}(K_x) \\ \vdots & \vdots & \ddots & \vdots \\ \mathbf{Q}_{N1}(K_x) & \mathbf{Q}_{N2}(K_x) & \cdots & \mathbf{Q}_{NN}(K_x) + \beta \end{bmatrix} \begin{bmatrix} \tilde{\mathbf{V}}_{filt}(K_x; \omega_1) \\ \tilde{\mathbf{V}}_{filt}(K_x; \omega_2) \\ \vdots \\ \tilde{\mathbf{V}}_{filt}(K_x; \omega_N) \end{bmatrix} \qquad (3\text{-}41)$$

which can be inverted by the standard methods of linear algebra to yield the filtered data $\tilde{\mathbf{V}}_{filt}$ in terms of the raw, unfiltered data $\tilde{\mathbf{V}}$.

Then the final form of the imaging algorithm can be established by expressing $\mathbf{O}$ as a function of the filtered data $\tilde{\mathbf{V}}_{filt}$ [9, 10]

$$\begin{aligned}
\hat{\mathbf{O}}_\beta(x', z') &= \mathcal{A}^\dagger \tilde{\mathbf{V}}_{filt}(x', z') \\
&= \sum_{n=1}^{N} 2\pi \mathcal{P}^*(\omega_n) \int_{-\infty}^{\infty} dK_x{}' \int_{-\infty}^{\infty} dK_{0x}{}' \mathcal{B}^*(K_x{}' + K_{0x}{}', K_{0x}{}'; \omega_n) \\
&\quad e^{i[\gamma^*(K_x{}'+K_{0x}{}', \omega_n)+\gamma^*(K_{0x}{}', \omega_n)]z'} e^{iK_x{}'x'} \tilde{\mathbf{V}}_{filt}(K_x{}'; \omega_n) \quad . \qquad \text{(3-42)}
\end{aligned}$$

4 Reconstruction Results

The two-dimensional and three-dimensional pseudo-inverse imaging algorithms described in the previous sections have been applied to both synthetic and experimental multi-monostatic GPR data. Good quantitative images of objects embedded in both lossless and attenuating background are generated. Our goal is to show that our algorithms are suitable for realistic GPR applications.

4.1 2-D Pseudo-inverse Reconstruction

In Section 4.1.1, we show examples of image reconstructions for 2-D synthetic multi-monostatic GPR data. In Section 4.1.2, the reconstruction images of 2-D experimental multi-monostatic GPR data are shown. Both reconstructions use the direct analytical pseudo-inverse techniques described in Section 3.

4.1.1 Reconstruction Results for Synthetic Data

In our two-dimensional synthetic data simulations, two 2-D objects are used, one is a point scatterer(Figure (4-1)), and the other is a rectangle(Figure (4-2)).[15] The point scatterer and rectangle are both embedded in a soil background having a complex dielectric contrast $\varepsilon/\varepsilon_0 = 0.8$ [16]at all frequencies relative to the surrounding soil. Therefore, the value of object function is (from Equation (3-1)) $\mathbf{O}(x, z) = 1 - 0.8 = 0.2$

[15]In all the figures illustrated in Chapter 4, the plotting contrast has been reversed to improve the display so that, in the reconstructed images, the negative object function $-\mathbf{O}$ is plotted.

[16]It has been shown [42] that DT using the Born approximation is adequate for quantitatively reconstructing objects with roughly

for the point scatterer or within the rectangle, and $\mathbf{O} = 0$ within the background area.

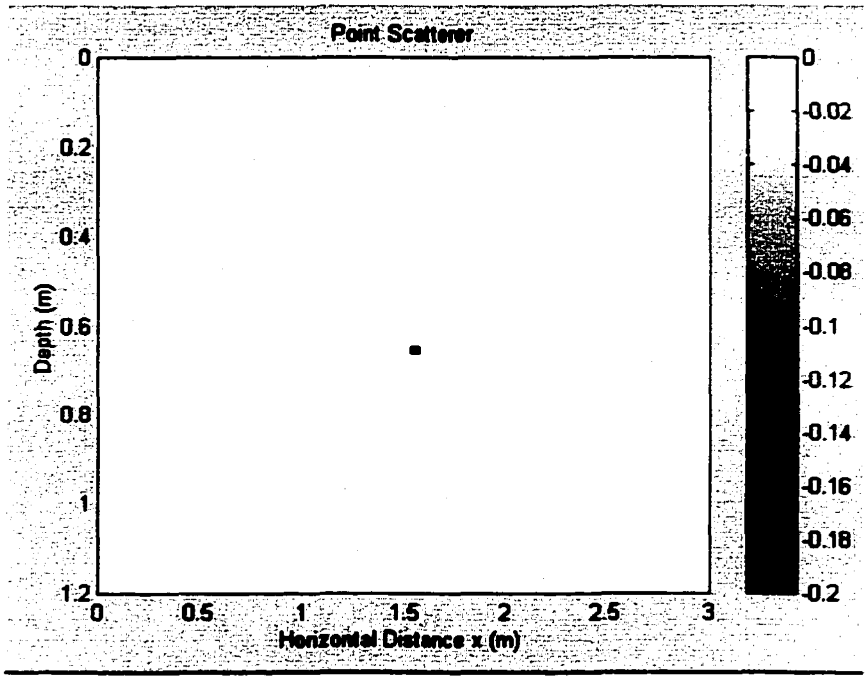

Figure 4-1: Location of the two-dimensional point scatterer for pseudo-inverse synthetic data reconstruction. The point scatterer has a value of $\mathbf{O} = 0.2$ at all frequencies, and the background value is zero.

Lossless Background

First, it is assumed that our objects exist in a non-attenuating background soil (real k_0[17]). Figure (4-3) and Figure (4-4) are the forward scattering models of the point scatterer in the x-t domain using point source illumination and the Kerns' scattering

---

$$\left(0.8 \leq |\frac{\varepsilon}{\varepsilon_0}| \leq 1.2\right) \tag{4-1}$$

or a 20% contrast, when the object size is on the order of a wavelength.

[17]The range of the wavelengths λ is $0.2m \leq \lambda \leq 1m$. For lossless case, $k_0 = 2\pi/\lambda$.

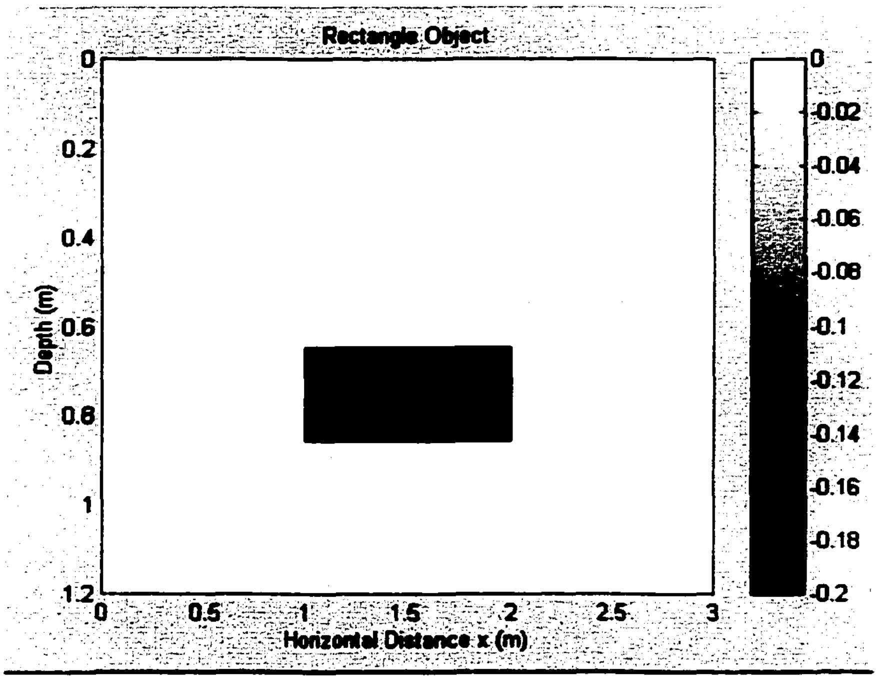

Figure 4-2: Original two-dimensional rectangle for pseudo-inverse synthetic data reconstruction. The rectangle has a value of $\mathbf{O} = 0.2$ at all frequencies, and the background value is zero.

matrix formulation. Figure (4-5) and Figure (4-6) are the reconstructed images of the point scatterer for both cases. Similarly, we show the forward model data for the rectangle in Figure (4-7) and Figure (4-8), and the reconstructed results are shown in Figure (4-9) and Figure (4-10).

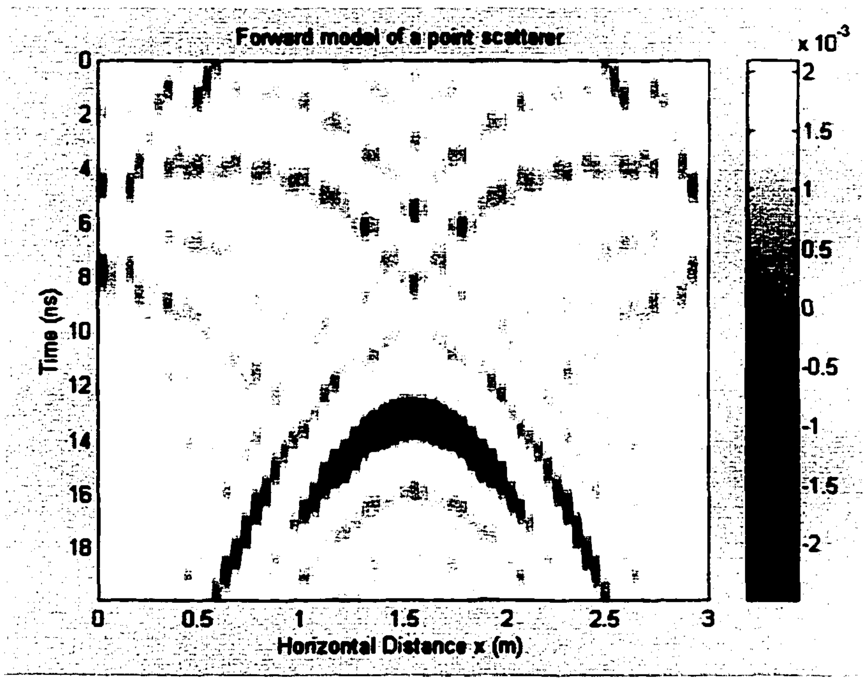

Figure 4-3: Forward model of a two-dimensional point scatterer in the x-t domain using point source illumination in a lossless background.

The reconstruction results are all based on nine frequencies uniformly distributed over 100 MHz to 500 MHz for a regularization parameter $\beta = 10^{-9}$. It can be noted that we get the rather good representation of the original objects.

Lossy Background

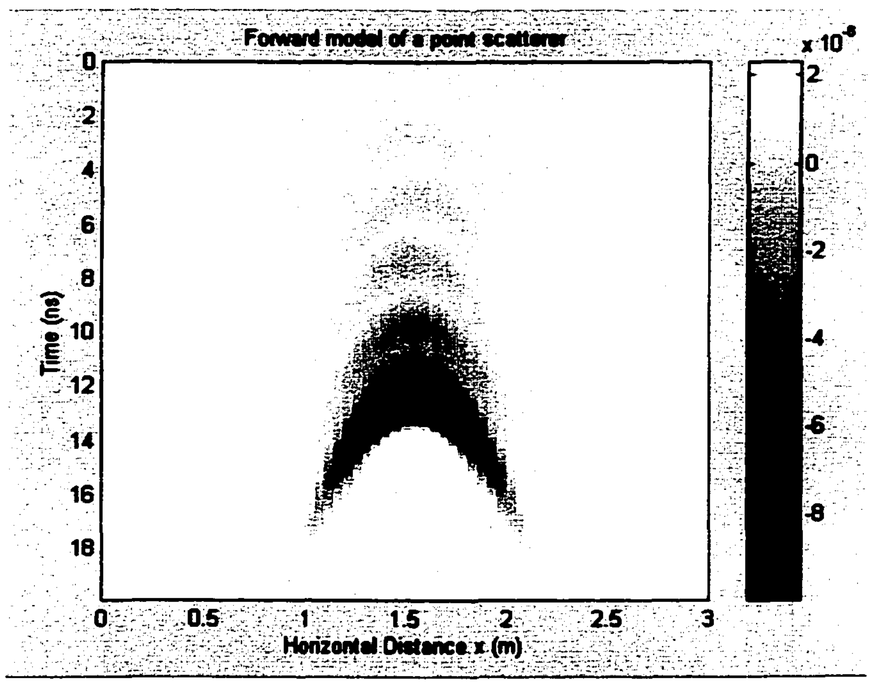

Figure 4-4: Forward model of a two-dimensional point scatterer in the x-t domain using the Kerns' scattering matrix formulation in a lossless background.

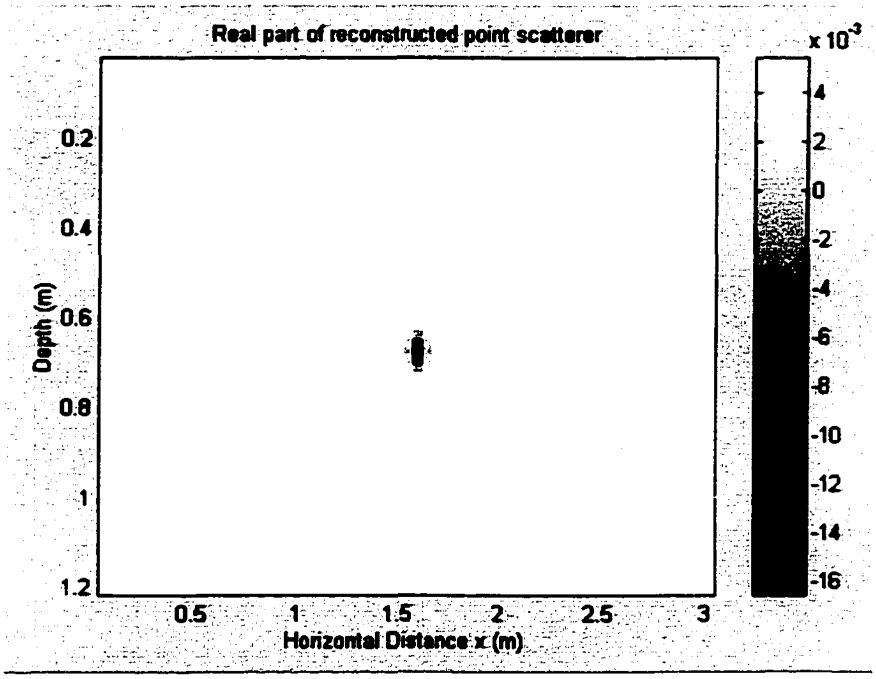

Figure 4-5: Two-dimensional pseudo-inverse reconstruction of a point scatterer using point source illumination based on nine frequencies in a lossless background.

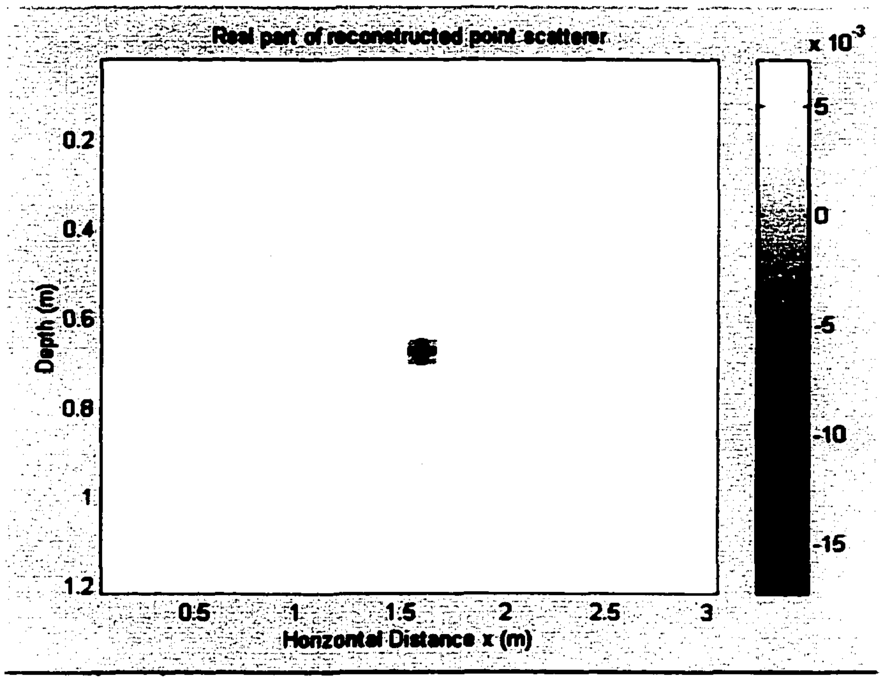

Figure 4-6: Two-dimensional pseudo-inverse reconstruction of a point scatterer using the Kerns' scattering matrix formulation based on nine frequencies in a lossless background.

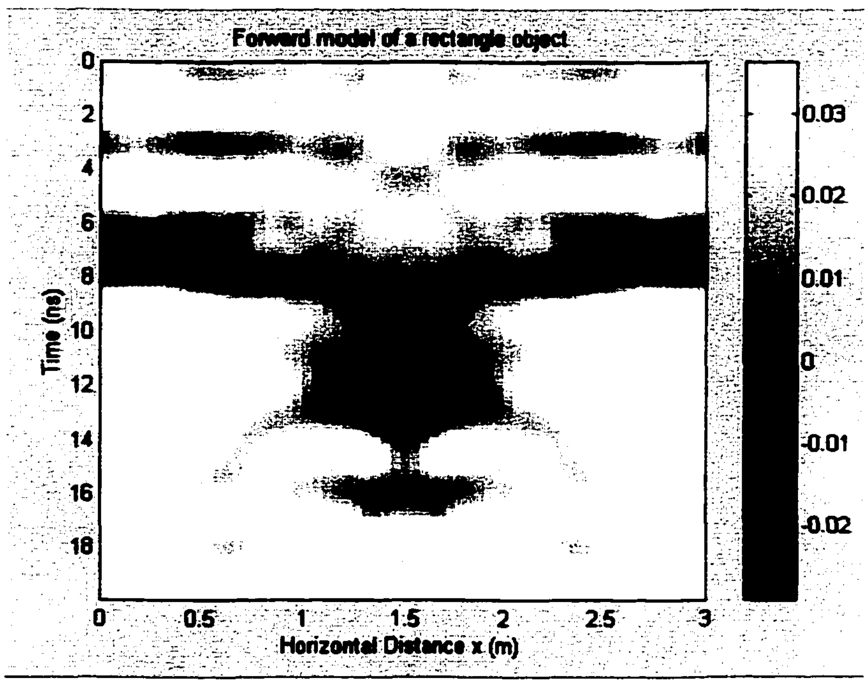

Figure 4-7: Forward model of a two-dimensional rectangle in the x-t domain using point source illumination in a lossless background.

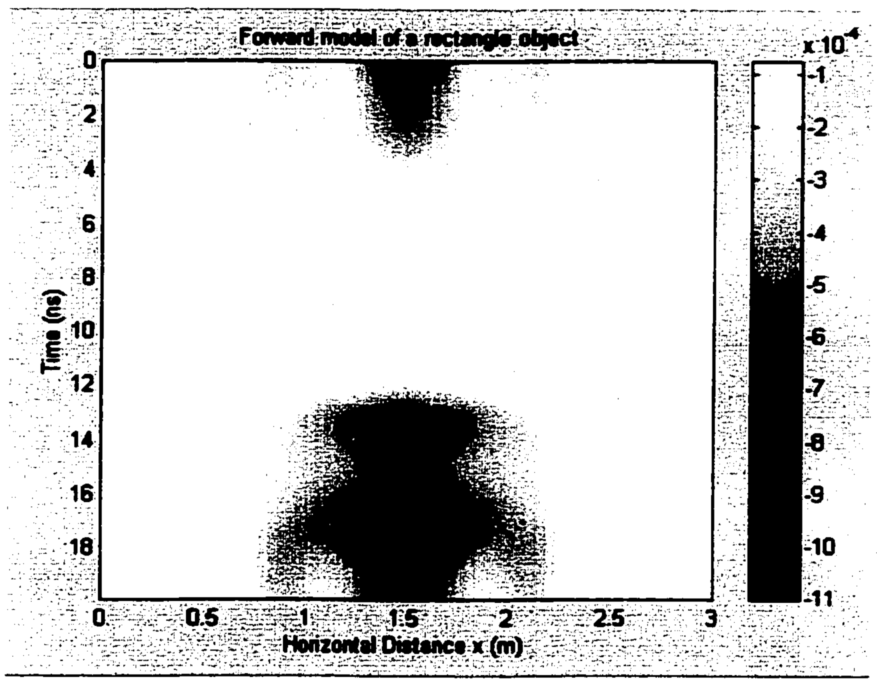

Figure 4-8: Forward model of a two-dimensional rectangle in the x-t domain using the Kerns' scattering matrix formulation in a lossless background.

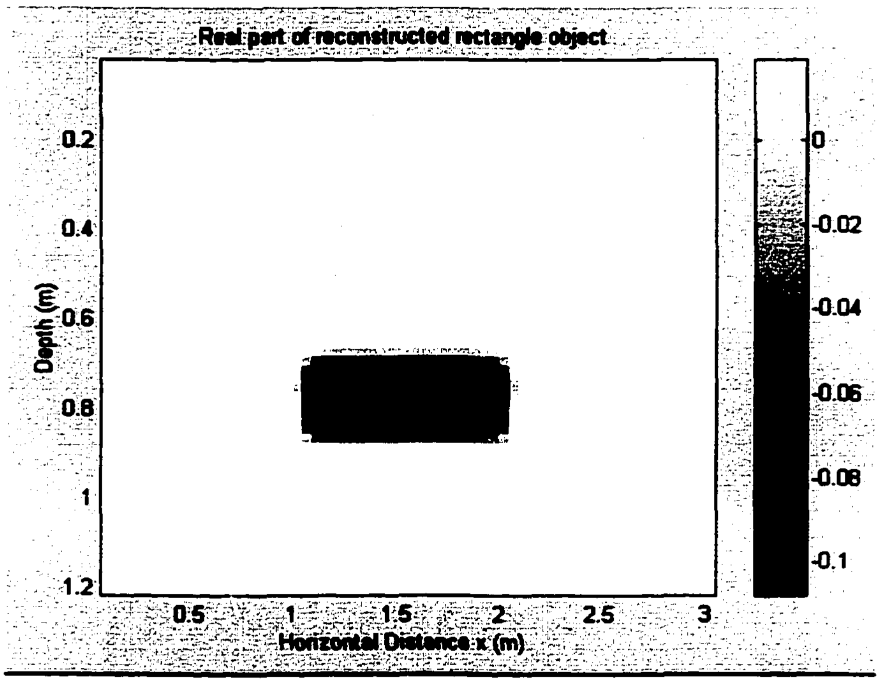

Figure 4-9: Two-dimensional pseudo-inverse reconstruction of a rectangle using point source illumination based on nine frequencies in a lossless background.

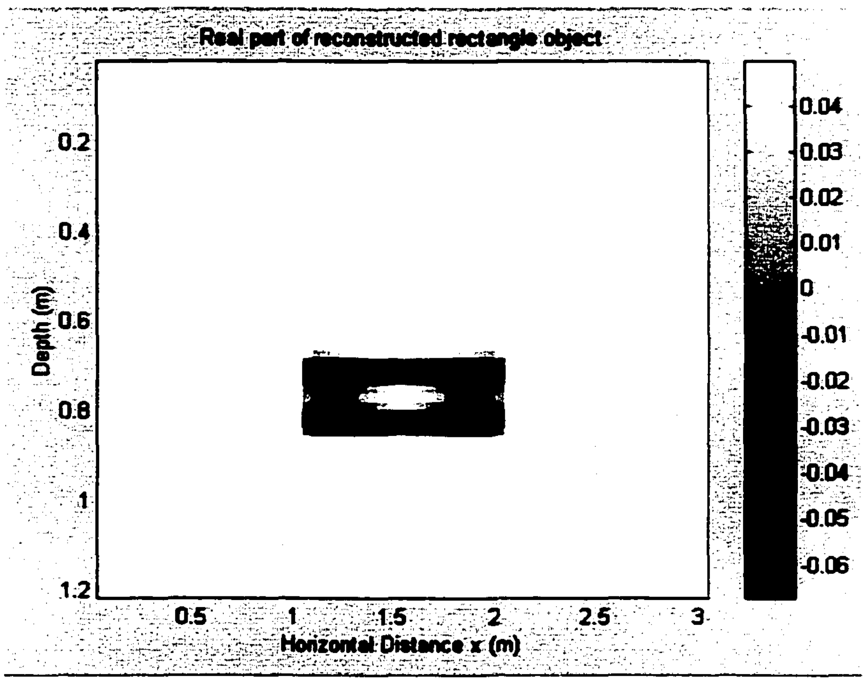

Figure 4-10: Two-dimensional pseudo-inverse reconstruction of a rectangle using the Kerns' scattering matrix formulation based on nine frequencies in a lossless background.

We assume that our objects exist in an attenuating background soil (complex k_0[18]). Figure (4-11) and Figure (4-12) are the forward scattering models of the point scatterer in the x-t domain using point source illumination and the Kerns' scattering matrix formulation, respectively. Figure (4-13) and Figure (4-14) are the reconstructed images of the point scatterer for both cases. Similarly, we show the forward models of the rectangle in Figure (4-15) and Figure (4-16), and the reconstructed results are shown in Figure (4-17) and Figure (4-18).

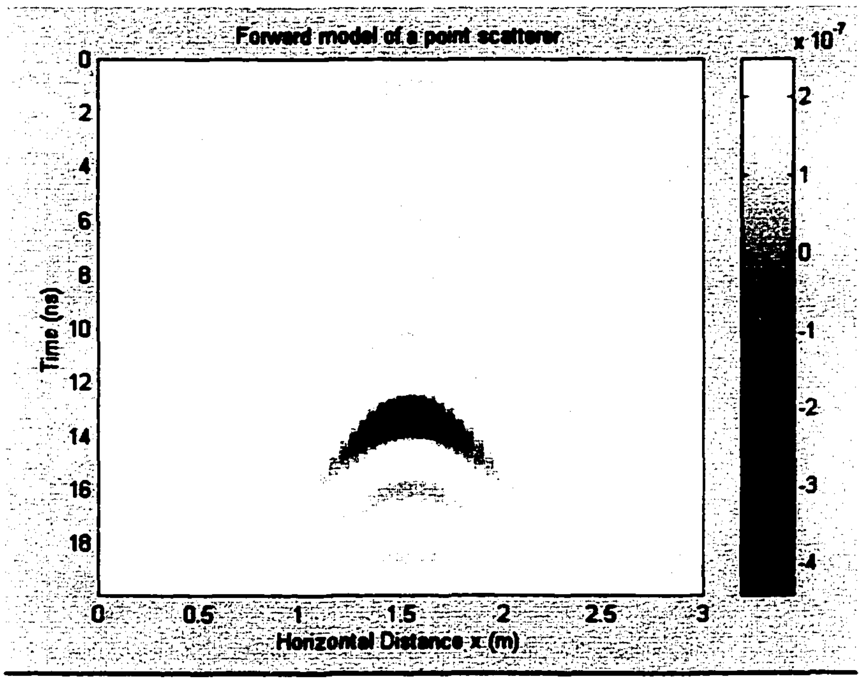

Figure 4-11: Forward model of a two-dimensional point scatterer in the x-t domain using point source illumination in a lossy background.

The reconstruction results are also based on the same nine frequencies used in the

[18]The range of the wavelengths λ is $0.2m \leq \lambda \leq 1m$. For lossy case, $k_0 = 2\pi/\lambda + i/depth$ (conductivity decreases linearly with depth).

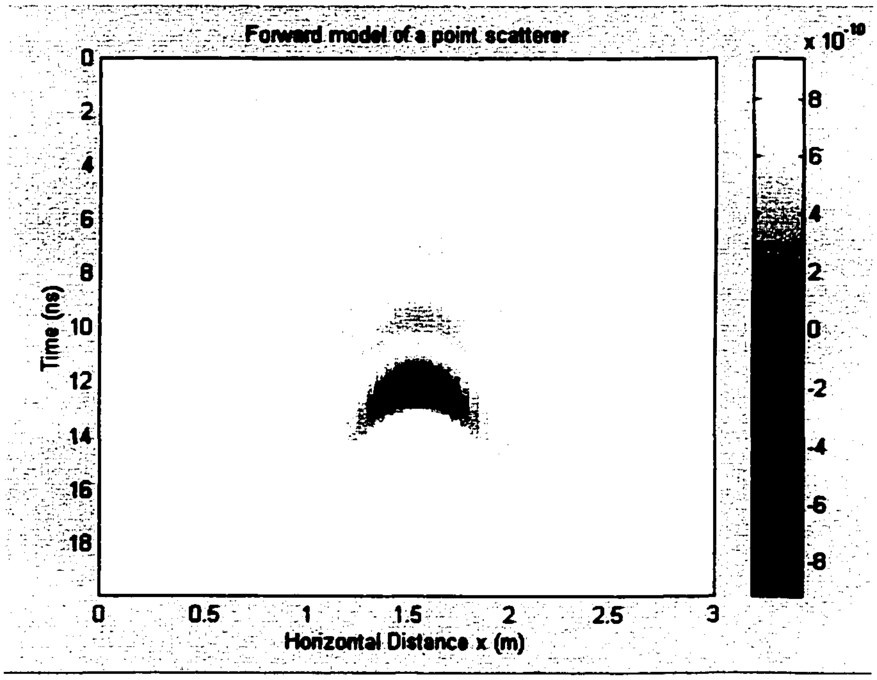

Figure 4-12: Forward model of a two-dimensional point scatterer in the x-t domain using the Kerns' scattering matrix model in a lossy background.

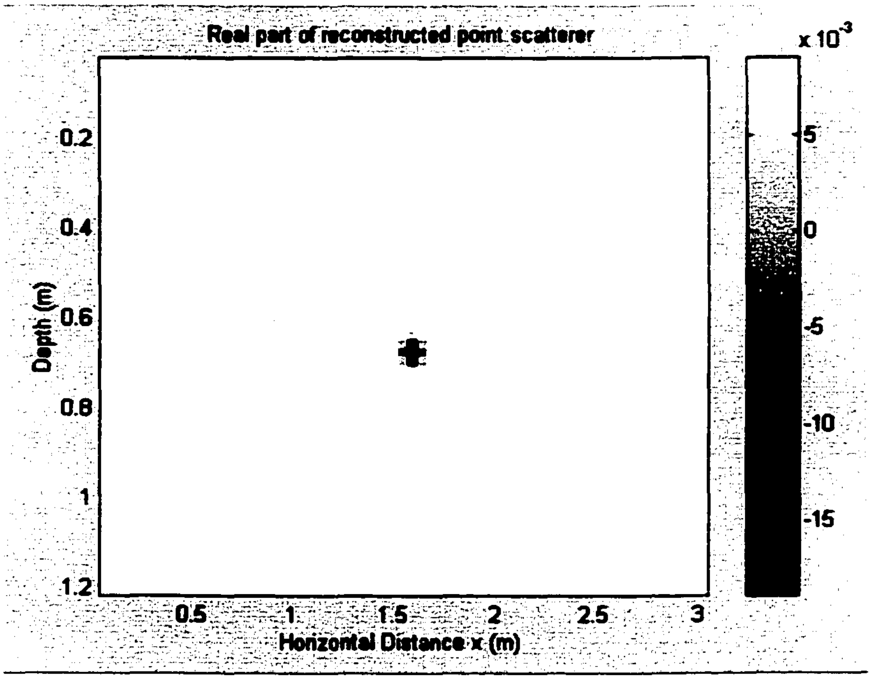

Figure 4-13: Two-dimensional pseudo-inverse reconstruction of a point scatterer using point source illumination based on nine frequencies in a lossy background.

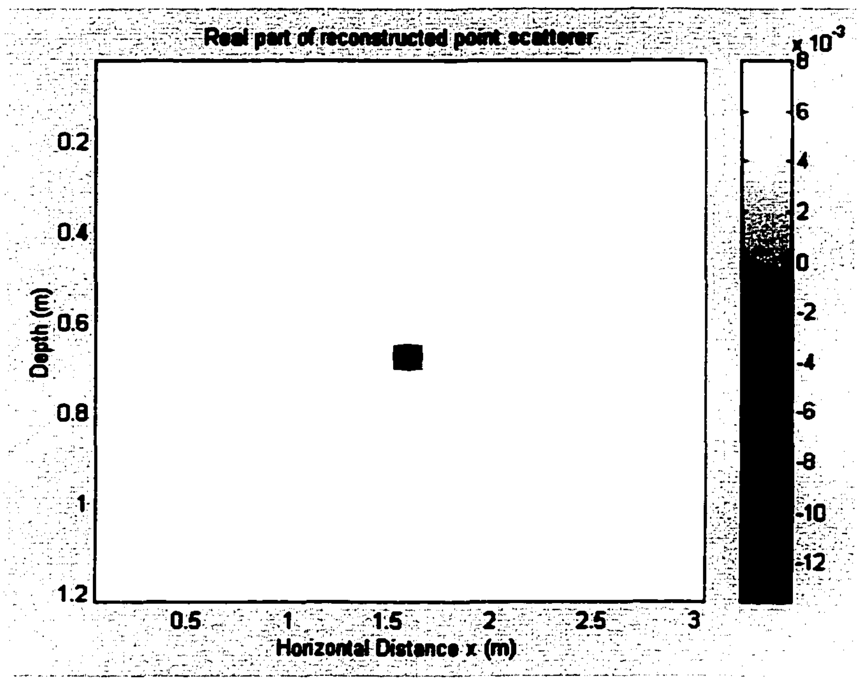

Figure 4-14: Two-dimensional pseudo-inverse reconstruction of a point scatterer using the Kerns' scattering matrix formulation based on nine frequencies in a lossy background.

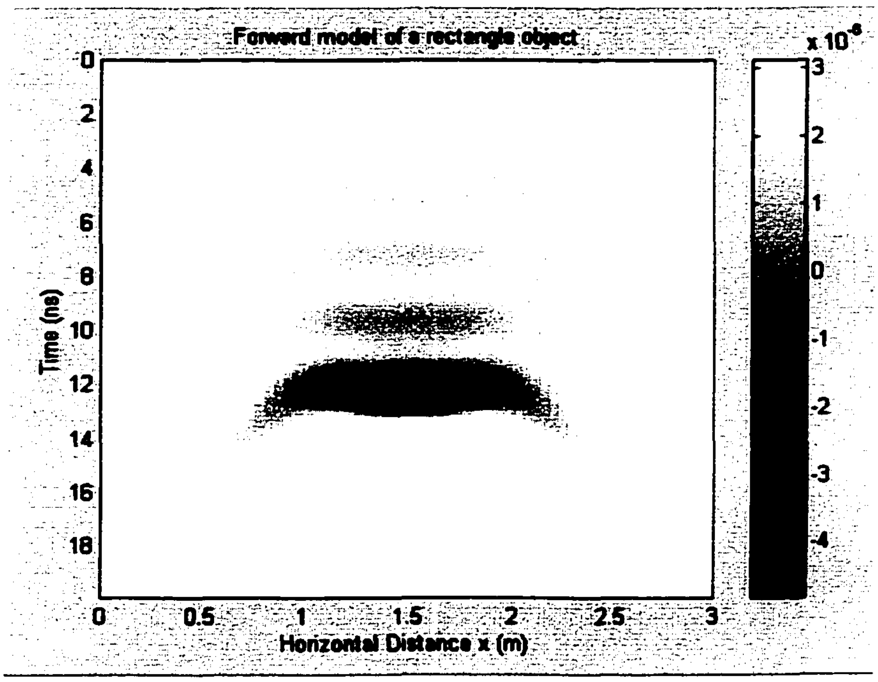

Figure 4-15: Forward model of a two-dimensional rectangle in the x-t domain using point source illumination in a lossy background.

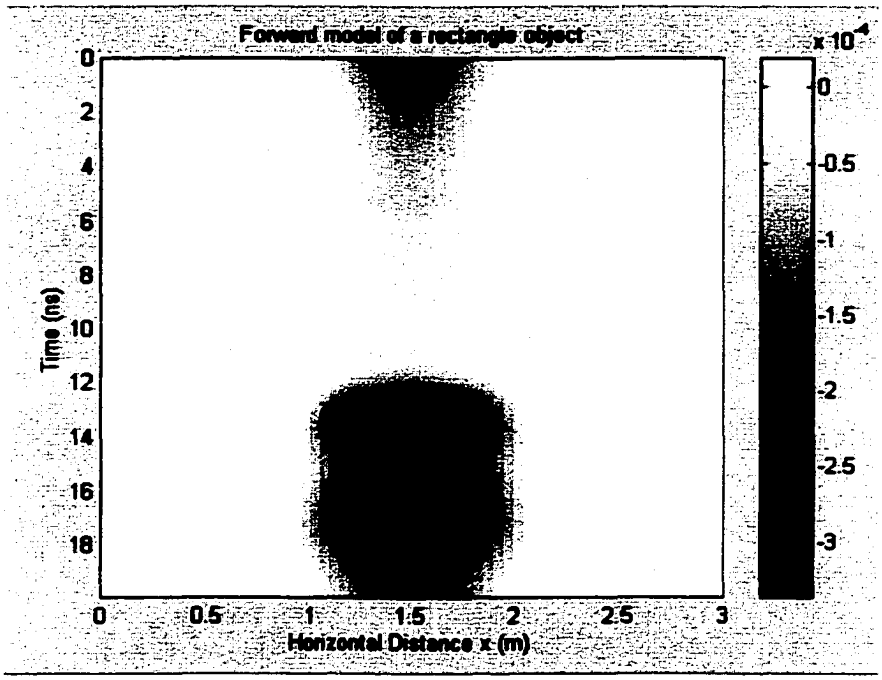

Figure 4-16: Forward model of a two-dimensional rectangle in the x-t domain using the Kerns' scattering matrix model in a lossy background.

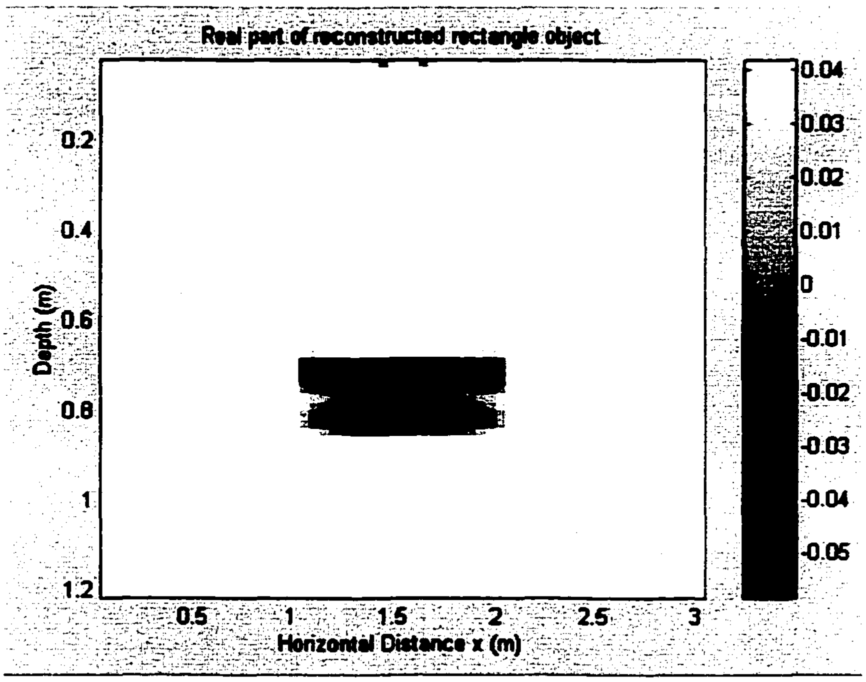

Figure 4-17: Two-dimensional pseudo-inverse reconstruction of a rectangle using point source illumination based on nine frequencies in a lossy background.

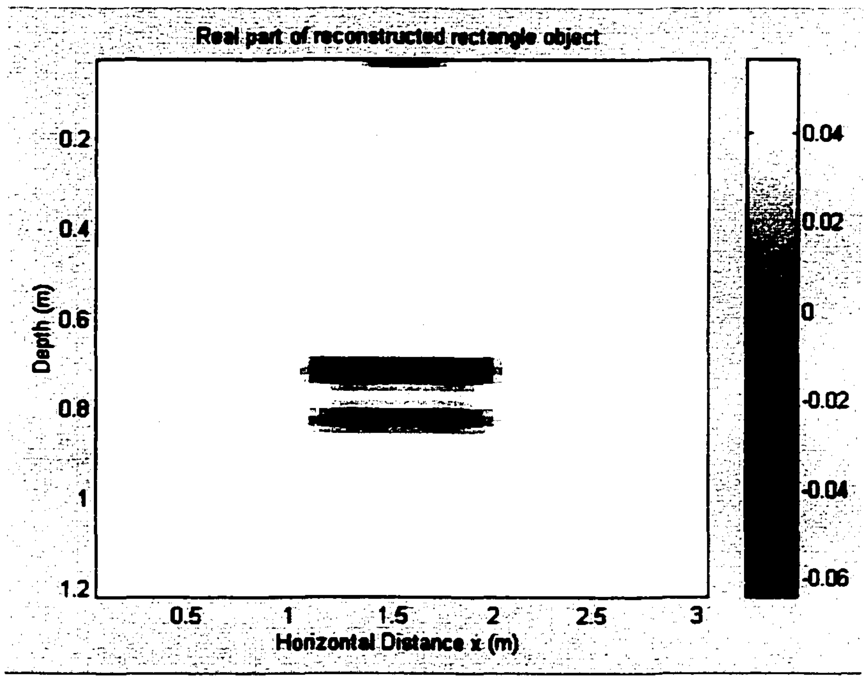

Figure 4-18: Two-dimensional pseudo-inverse reconstruction of a rectangle using the Kerns' scattering matrix formulation based on nine frequencies in a lossy background.

lossless case. We get the fairly good images of the point scatterer and the rectangle. As expected, there is a slight loss of amplitude in the reconstructed images as compared to the lossless background. We can also notice that the reconstructed rectangle is hollow, and only the boundaries of the rectangle are reconstructed. This is because for the K-space coverage [9] of our imaging algorithm, there is no coverage at the origin $K_x = K_y = 0$. This suggests that there is no spatial DC component and the average value of the reconstructed object function $\mathbf{O}$ will be zero, and consequently the image will be hollow.

4.1.2 Reconstruction Results for Experimental Data

Two-dimensional multi-monostatic GPR measurements were made over a cast iron pipe in a large sand pit using a Mala RAMAC system with 200 MHz center-frequency antennas. The measurement line was perpendicular to the pipe axis. Figure (4-19) shows one of the vertical sections of the raw data.

All reconstructions presented here assume a lossless background, a background wave speed of 0.11 m/ns, and use 30 frequencies uniformly distributed over the spectral band 50 - 417 MHz (Figure (4-20)). Dipole antennas, such as those used in this study, are characterized as being fairly directional, with (two-dimensional scalar) transmitting coefficients given by

$$\mathbf{S}_{10}(K_x, \omega) = \frac{e^{a(\omega)K_x{}^2}}{\gamma(K_x, \omega)} \quad . \tag{4-2}$$

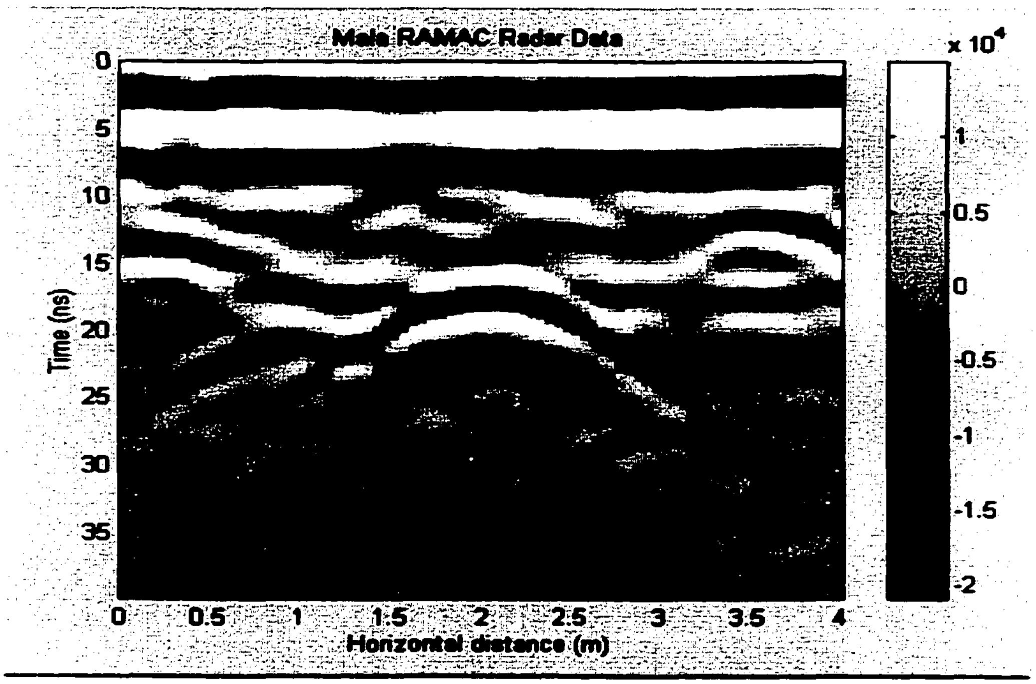

Figure 4-19: Two-dimensional monostatic GPR data

When the exponential function a is large, the beam pattern is quite directional with most of the energy being radiated vertically and, conversely, when a is small, the antennas are nearly omni-directional. Since antenna beam patterns can change with soil conditions, there is no practical means to fully characterize the beam patterns of a particular antenna pair. Here, several forms of a are empirically tested.

In the first case, $a(\omega) = -\alpha \ln(10)/\Re[k_0]^2$ is used. Figure (4-21) shows the reconstructed image of permittivity for $\alpha = 1$ (left) and $\alpha = 10$ (right). The ringing of the shallower layers is caused by the limited bandwidth.

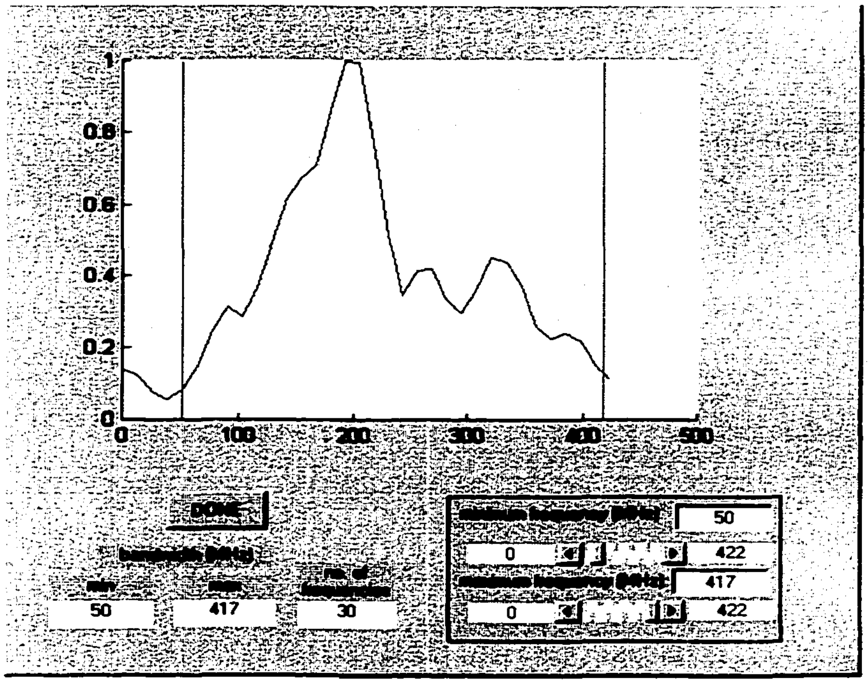

Figure 4-20: Frequency spectrum of a two-dimensional monostatic GPR data set

As expected, the image of the pipe becomes more elongated as the beam pattern becomes more directional. For both cases shown in this figure, the beam patterns are too directional.

The best reconstruction of the pipe was obtained for $\alpha = 0.01$ (Figure (4-22)). Here, the image of the pipe is nearly circular, as it should be. The deeper region of high permittivity is presumed to be water-saturated sand.

To evaluate the influence of frequency-dependence in the beam pattern, images are reconstructed for $a = -\alpha \ln(10)$. Figure (4-23) shows the reconstructed spatial variations in permittivity for $\alpha = 1$ (left) and $\alpha = 0.01$ (right).

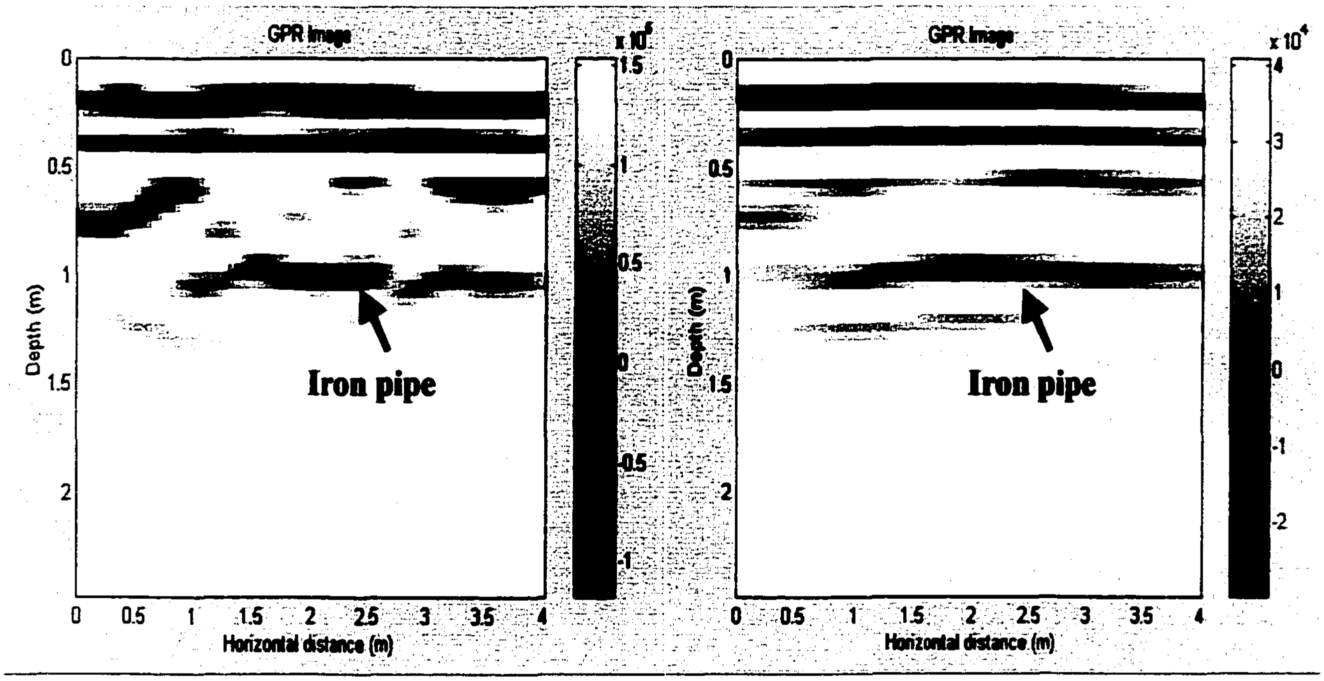

Figure 4-21: Reconstructed image of permittivity using the pseudo-inverse algorithm for two-dimensional monostatic GPR data using $\alpha = 1$ (left) and $\alpha = 10$ (right).

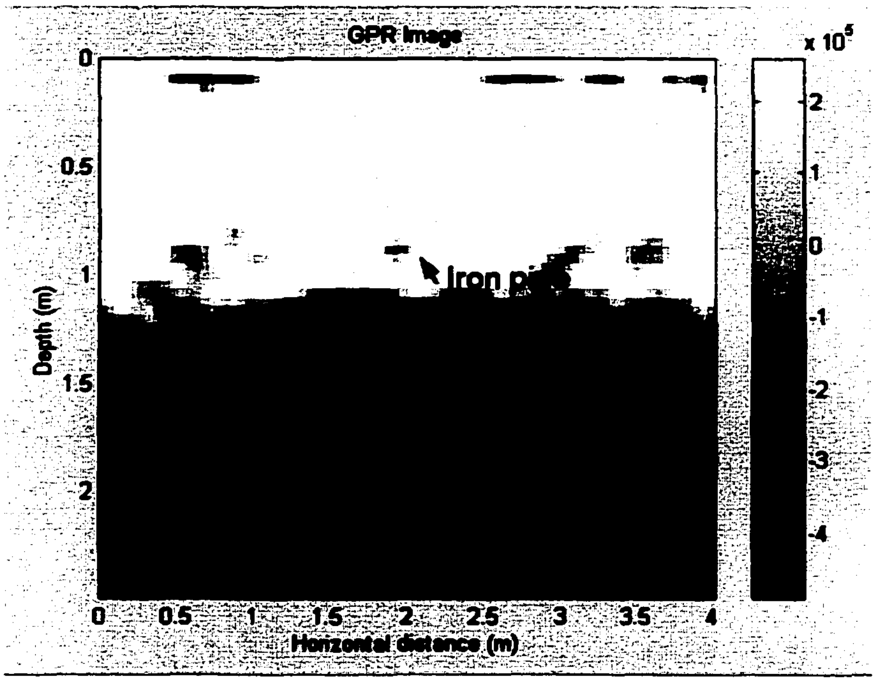

Figure 4-22: Reconstructed image of permittivity using pseudo-inverse algorithm for two-dimensional monostatic GPR data for $\alpha = 0.01$.

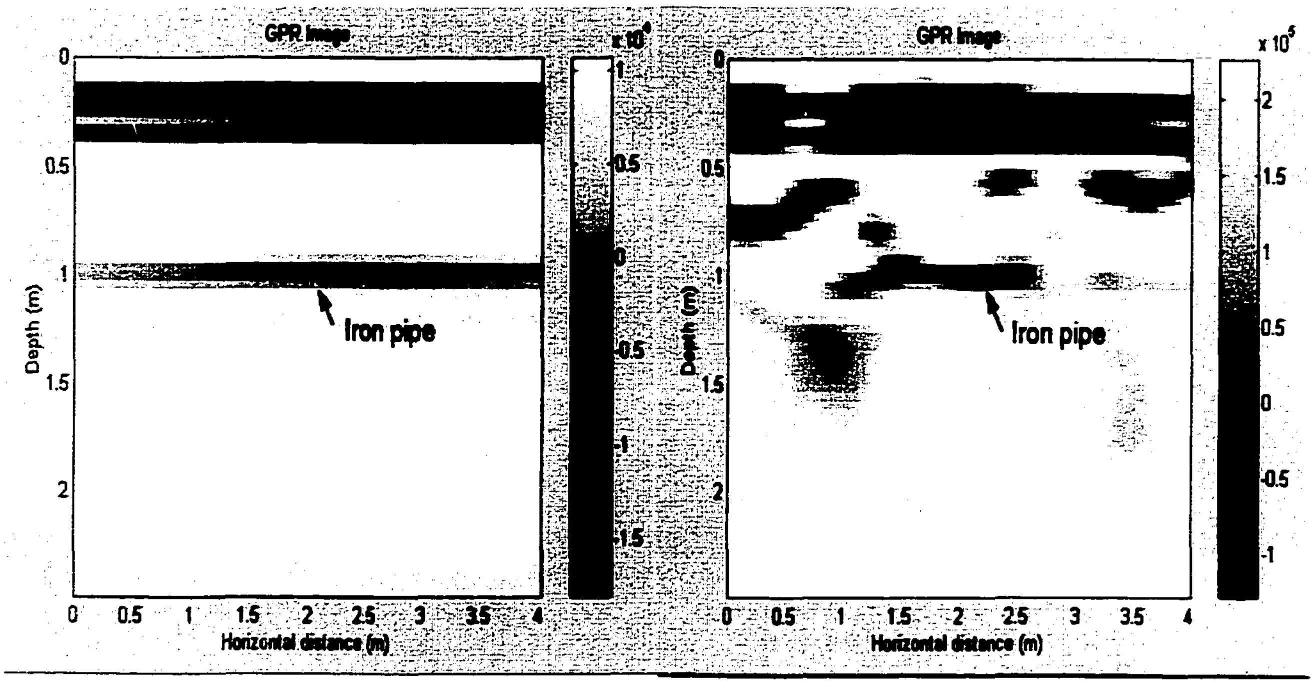

Figure 4-23: Reconstructed image of permittivity using the pseudo-inverse algorithm for two-dimensional monostatic GPR data using $\alpha = 1$ (left) and $\alpha = 10$ (right).

The image of the pipe becomes less elongated as the beam pattern becomes less directional; however, this form of the beam pattern provides results that are inferior to the frequency-dependent beam pattern.

4.2 3-D Pseudo-inverse Reconstruction

In Section 4.2.1, we show examples of image reconstructions for fully 3-D synthetic multi-monostatic GPR data. In Section 4.2.2, the image reconstruction of fully 3-D experimental multi-monostatic GPR data is shown. Both reconstructions use the directly analytical pseudo-inverse techniques described in Section 3. The comparison of our pseudo-inverse algorithm and the traditional DT algorithm is also given Section 4.2.2.

4.2.1 Reconstruction Results for Synthetic Data

In this section, the pseudo-inverse imaging formula is applied to broadband simulated data for a point scatterer (Figure (4-24)) in both lossless and attenuating background for the three-dimensional reflection geometry. Similar to the 2-D case, the point scatterer is embedded in a soil background, and has a complex dielectric contrast $\varepsilon/\varepsilon_0 = 0.8$ at all frequencies relative to the surrounding soil. Therefore, the value of object function is $\mathbf{O}(x, z) = 1 - 0.8 = 0.2$ for the point scatterer and $\mathbf{O} = 0$ within the background area.

Lossless Background

First, it is assumed that our object exists in a non-attenuating background soil (real k_0). Figure (4-25) and Figure (4-26) are the forward scattering models of the point scatterer in the x-t domain using point source illumination and the Kerns' scattering matrix formulation, respectively. Figure (4-27) is the reconstructed image of the point scatterer using point source illumination. Figure (4-28) is the reconstructed image of the point scatterer using the Kerns' scattering matrix model.

The reconstructions are all based on eight frequencies uniformly distributed over 100

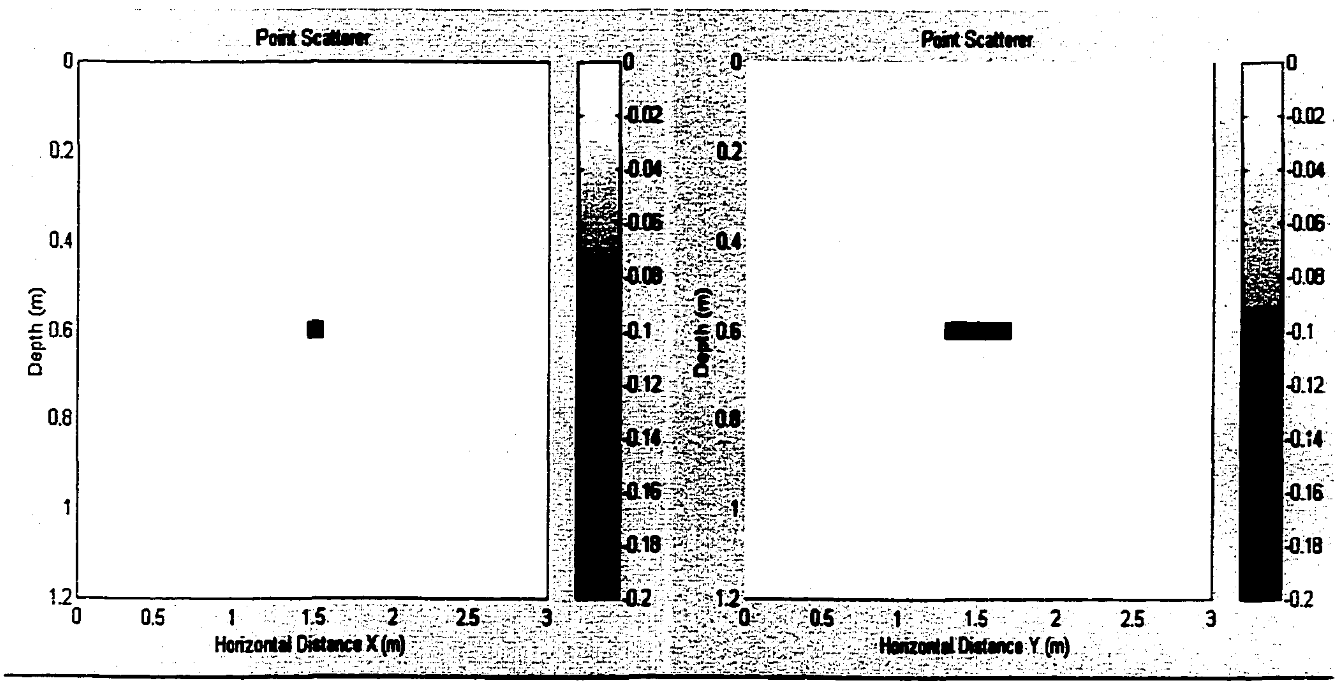

Figure 4-24: x-z slice (left) and y-z slice (right) of the original three-dimensional point scatterer for pseudo-inverse synthetic data reconstruction. The point scatterer has a value of 0.2 at all frequencies, and the background region has a value of zero.

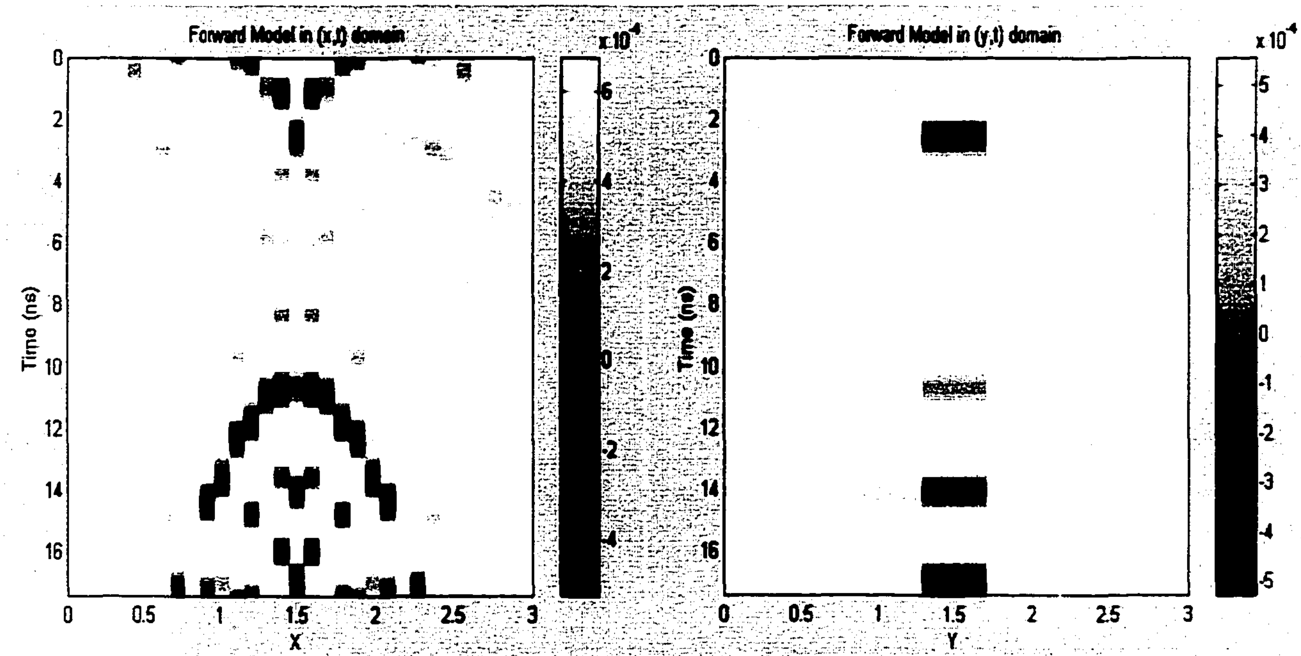

Figure 4-25: x-t slice (left) and y-t slice (right) of the forward model of a three-dimensional point scatterer using point source illumination in a lossless background.

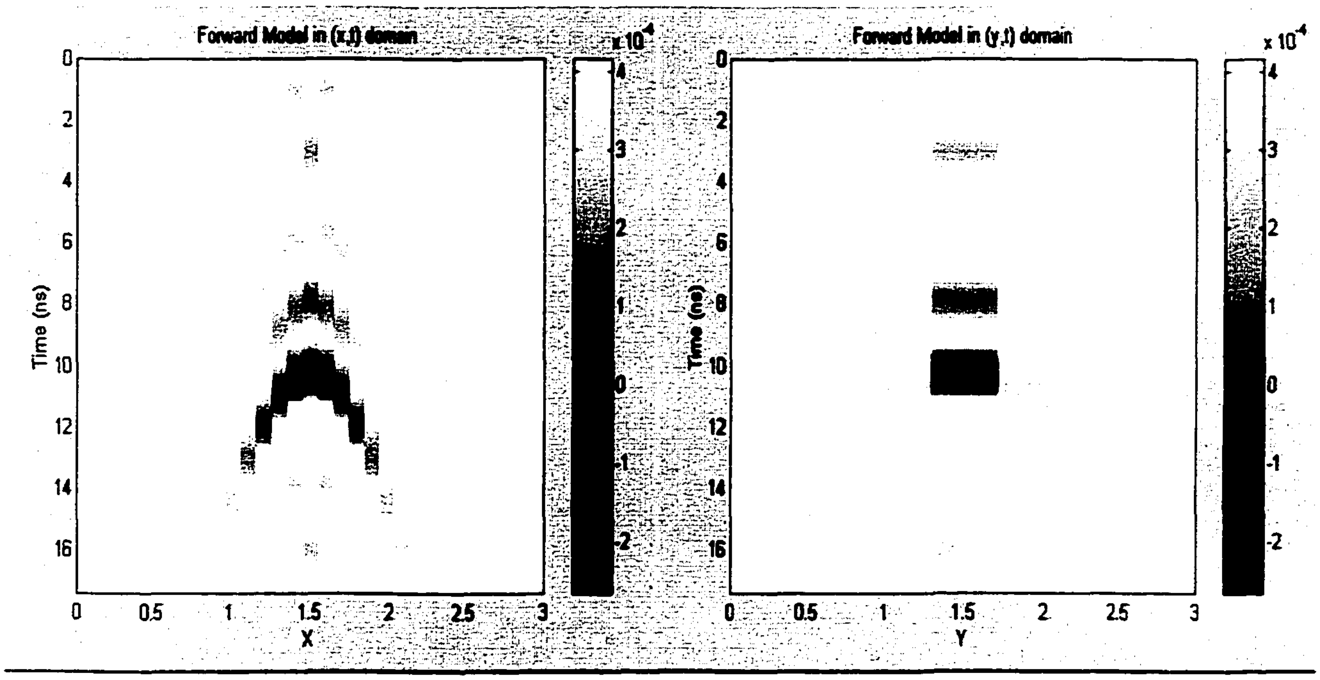

Figure 4-26: x-t slice (left) and y-t slice (right) of the forward model of a three-dimensional point scatterer using the Kerns' scattering matrix model in a lossless background.

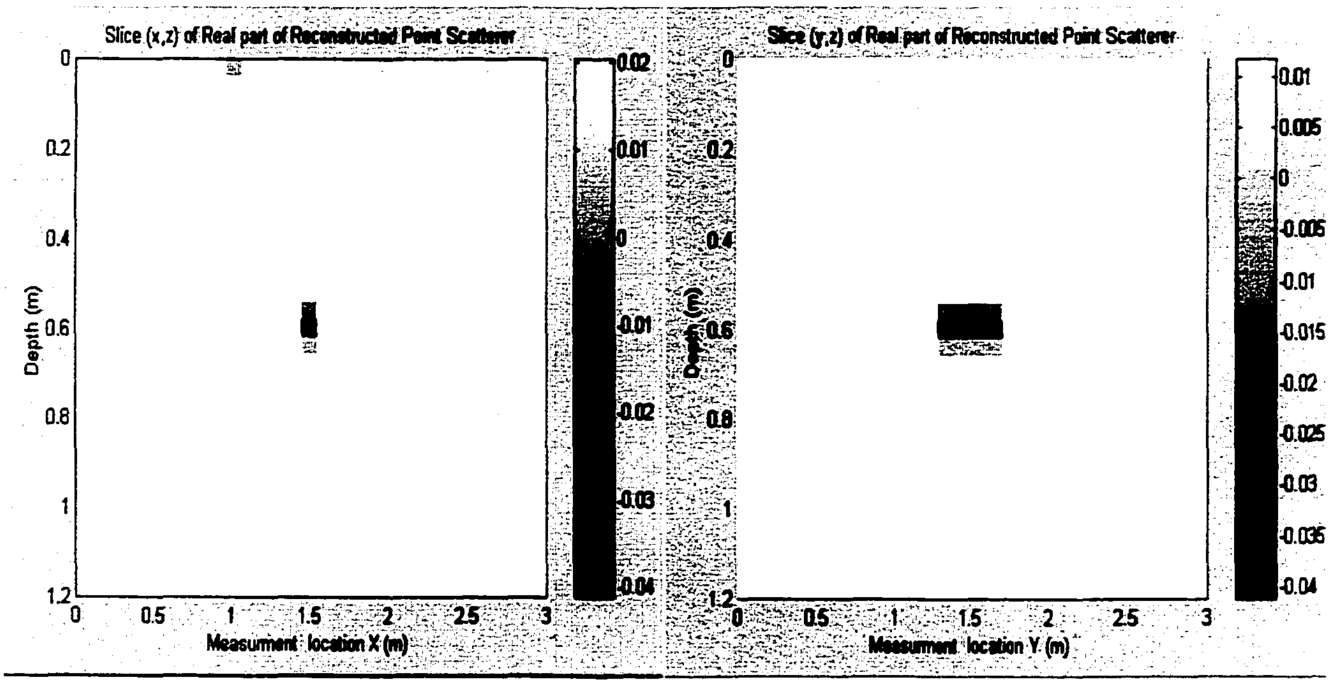

Figure 4-27: x-z slice (left) and y-z slice (right) of three-dimensional pseudo-inverse reconstruction of a point scatterer using point source illumination based on eight frequencies in a lossless background.

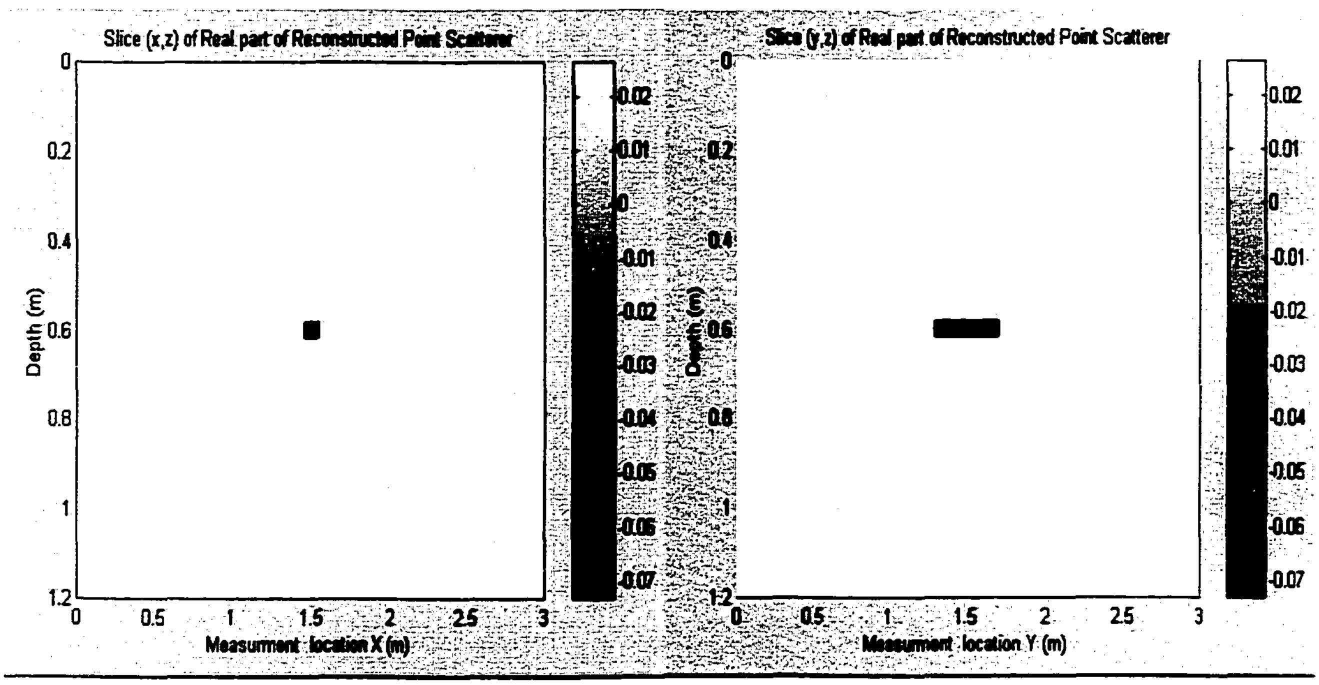

Figure 4-28: x-z slice (left) and y-z slice (right) of three-dimensional pseudo-inverse reconstruction of a point scatterer using the Kerns' scattering matrix formulation based on eight frequencies in a lossless background.

MHz to 500 MHz for a regularization parameter $\beta = 10^{-9}$. It can be noted that we get the rather good representation of the original objects.

Lossy Background

We assume that our object exists in an attenuating background soil (complex k_0[19]). Figure (4-29) and Figure (4-30) are the forward scattering models of the point scatterer in the x-t domain using point source illumination and the Kerns' scattering matrix formulation, respectively. Figure (4-31) is the reconstructed image of the point scatterer using point source illumination. Figure (4-32) is the reconstructed image of the point scatterer using the Kerns' scattering matrix model.

The reconstructions are also based on the same eight frequencies used in the lossless case. We get a fairly good image of the point scatterer. As in the 2-D case, there is also a slight loss of amplitude in the reconstructed images as compared to the lossless background.

4.2.2 Reconstruction Results for Experimental Data

Fully three-dimensional multi-monostatic GPR measurements were made over a plastic water pipe beneath the street in Tampa, FL, using a Mala RAMAC system with 250 MHz center-frequency antennas. Figure (4-33) shows two slices of the vertical

[19]The range of the wavelengths λ is $0.2m \leq \lambda \leq 1m$. For lossy case, $k_0 = 2\pi/\lambda + i/depth$ (conductivity decreases linearly with depth).

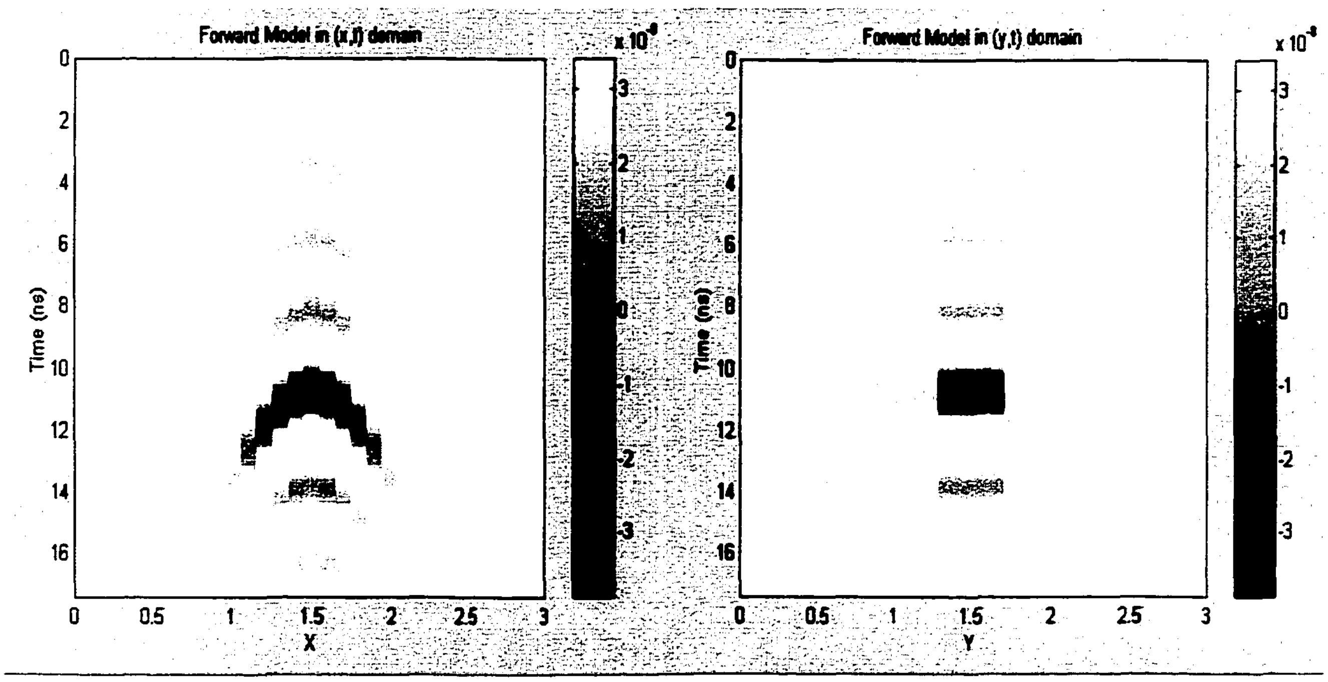

Figure 4-29: x-t slice (left) and y-t slice (right) of the forward model of a three-dimensional point scatterer using point source illumination in a lossy background.

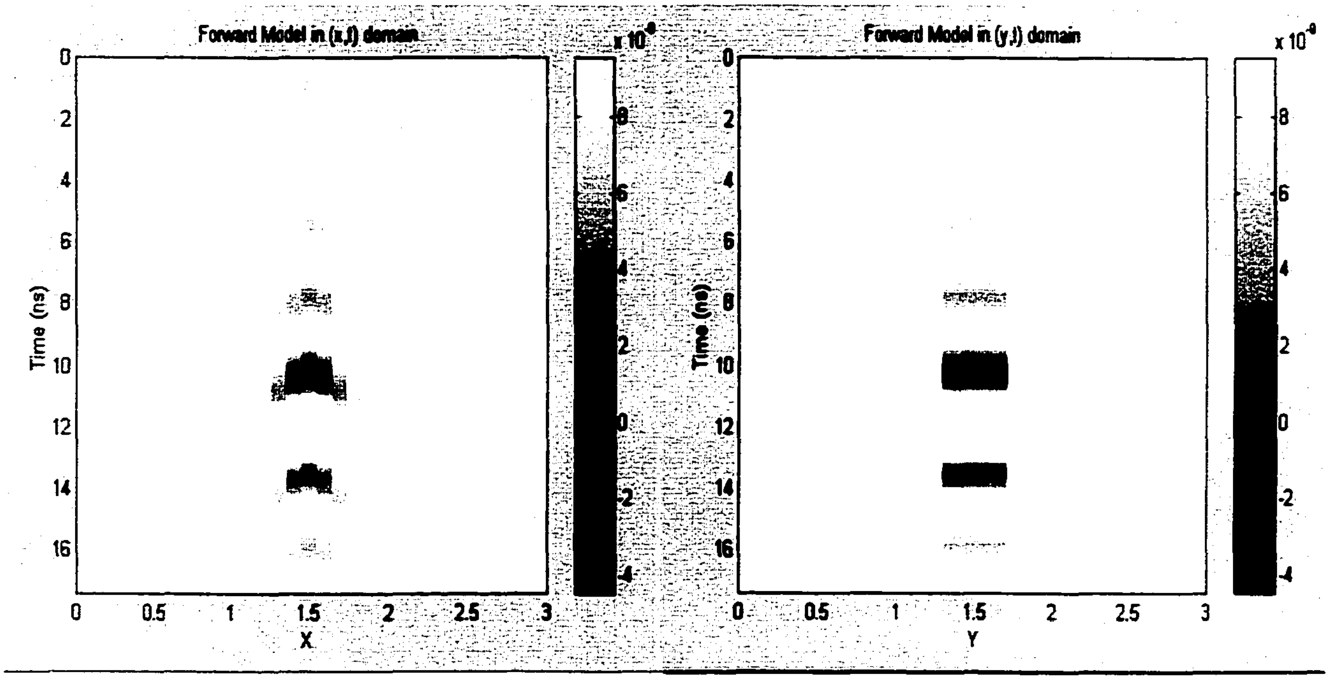

Figure 4-30: x-t slice (left) and y-t slice (right) of the forward model of a three-dimensional point scatterer using the Kerns' scattering matrix model in a lossy background.

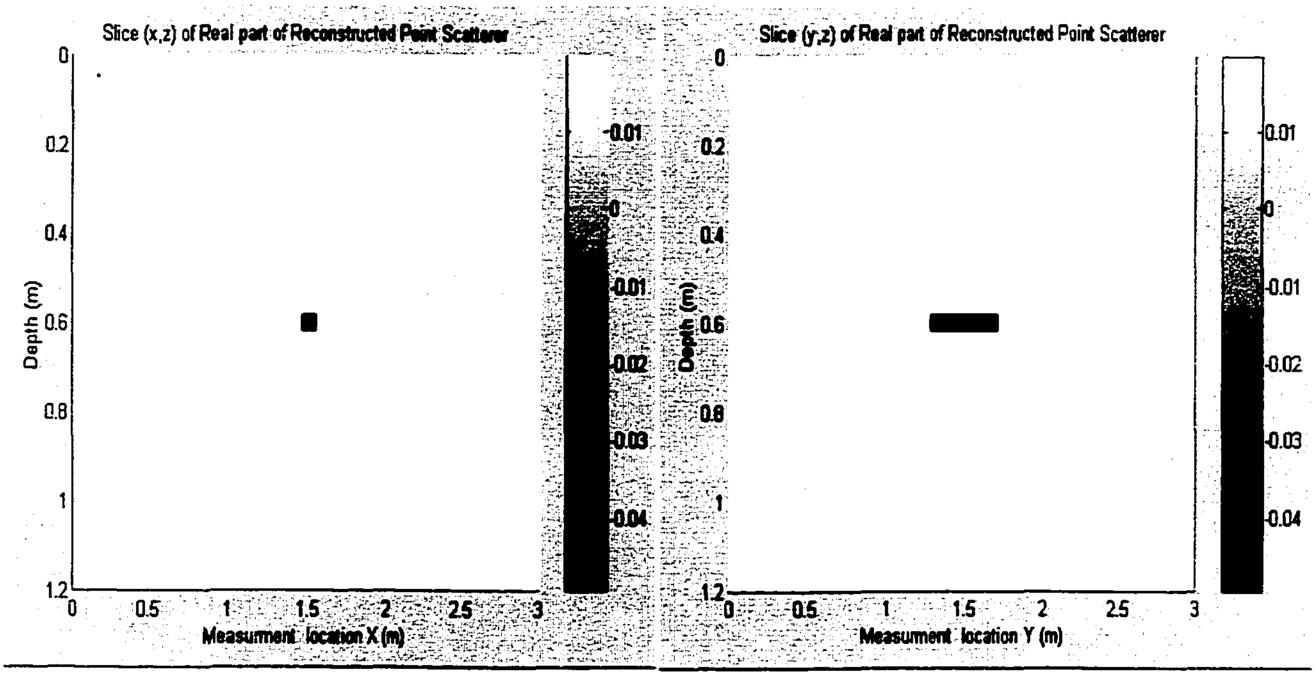

Figure 4-31: x-z slice (left) and y-z slice (right) of three-dimensional pseudo-inverse reconstruction of a point scatterer using point source illumination based on eight frequencies in a lossy background.

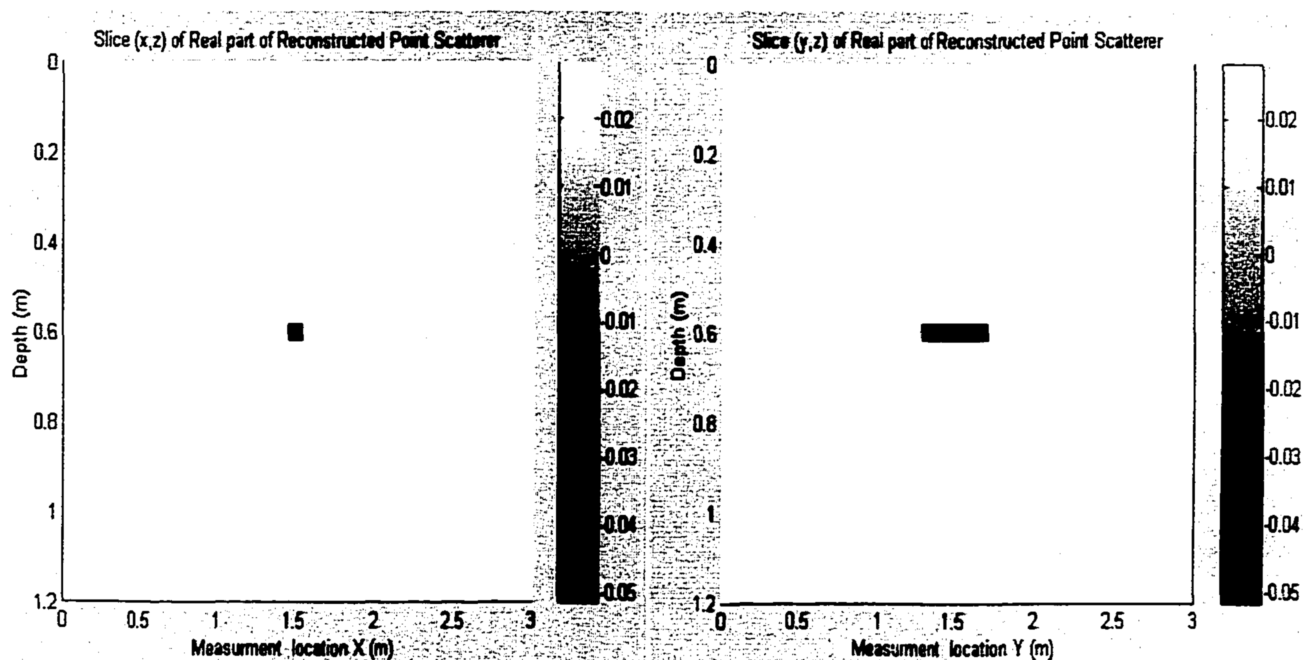

Figure 4-32: x-z slice (left) and y-z slice (right) of three-dimensional pseudo-inverse reconstruction of a point scatterer using the Kerns' scattering matrix formulation based on eight frequencies in a lossy background.

sections of the raw data.

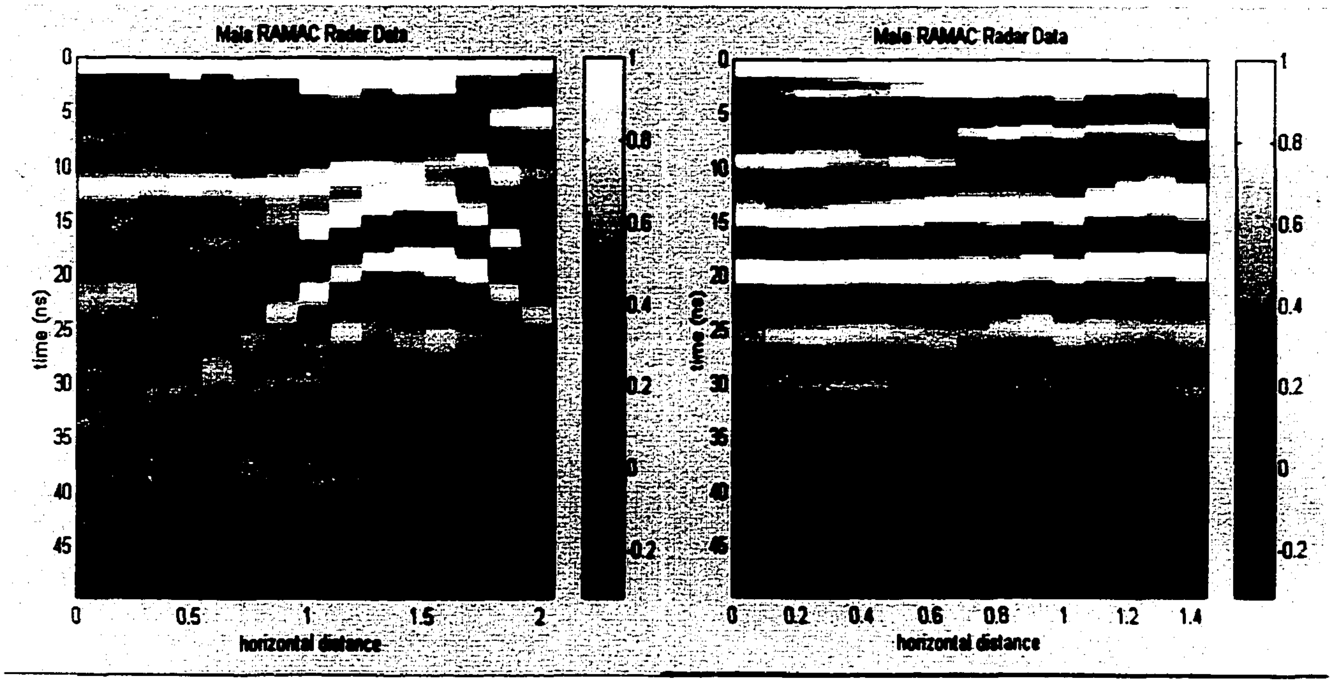

Figure 4-33: x-t slice (left) and y-t slice (right) of vertical sections of the three-dimensional monostatic GPR data

Our reconstruction presented here assumes a lossless background, a background wave speed of 0.1 m/ns, and uses 32 frequencies uniformly distributed over the spectral band 51 - 356 MHz (Figure (4-34)). Since we have no prior knowledge of the antenna beam pattern used in this particular study, several antenna transmitting coefficients are tested in the reconstructions. The best result is shown in Figure (4-35). Figure (4-36) is the reconstructed plastic pipe in three-dimensions.

For comparison, we give reconstructions using the traditional DT algorithm for the same full three-dimensional GPR data set in Figure (4-37). The reconstruction is also

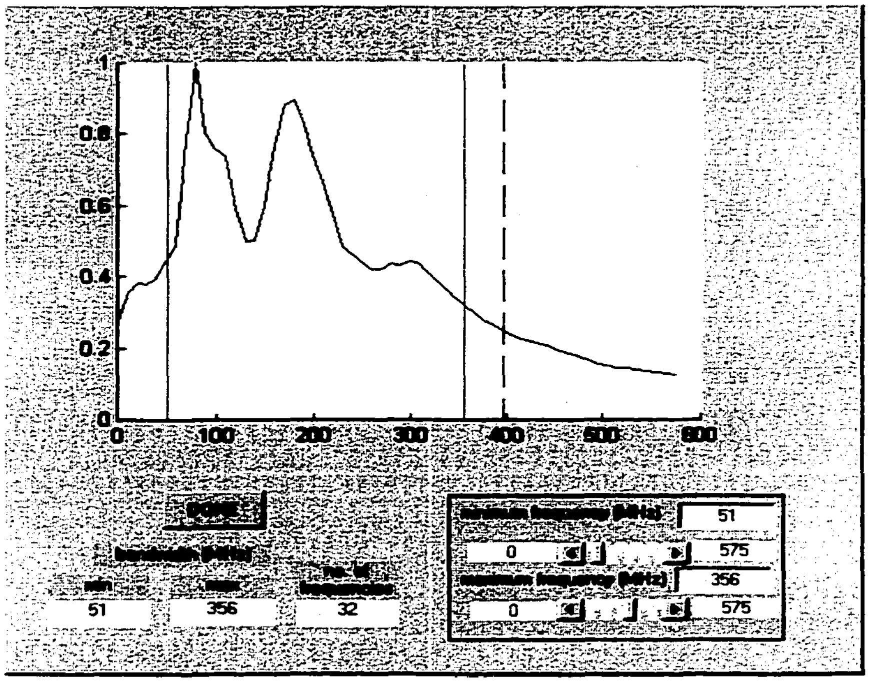

Figure 4-34: Frequency spectrum of a three-dimensional monostatic GPR data set

based on the same background wave speed and the same spectral range. Comparing Figure (4-35) and Figure (4-37), we find that both images of the pipe are in exactly the same locations.

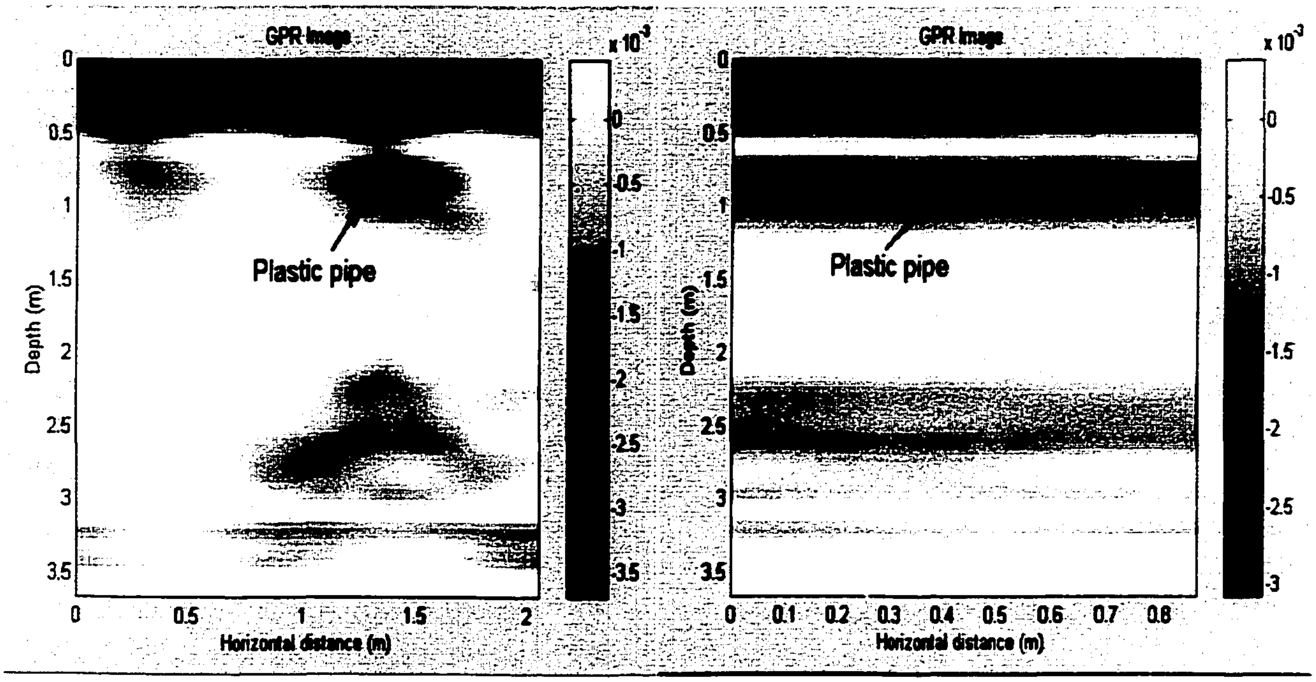

Figure 4-35: x-z slice (left) and y-z slice (right) of the three-dimensional pseudo-inverse reconstruction of a plastic pipe.

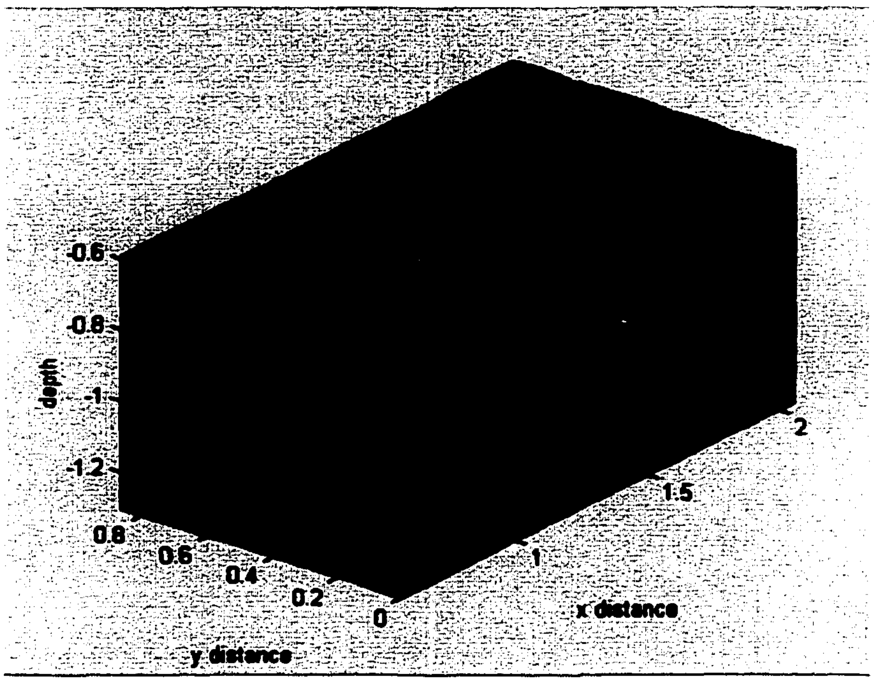

Figure 4-36: Three-dimensional pseudo-inverse reconstruction of a plastic pipe.

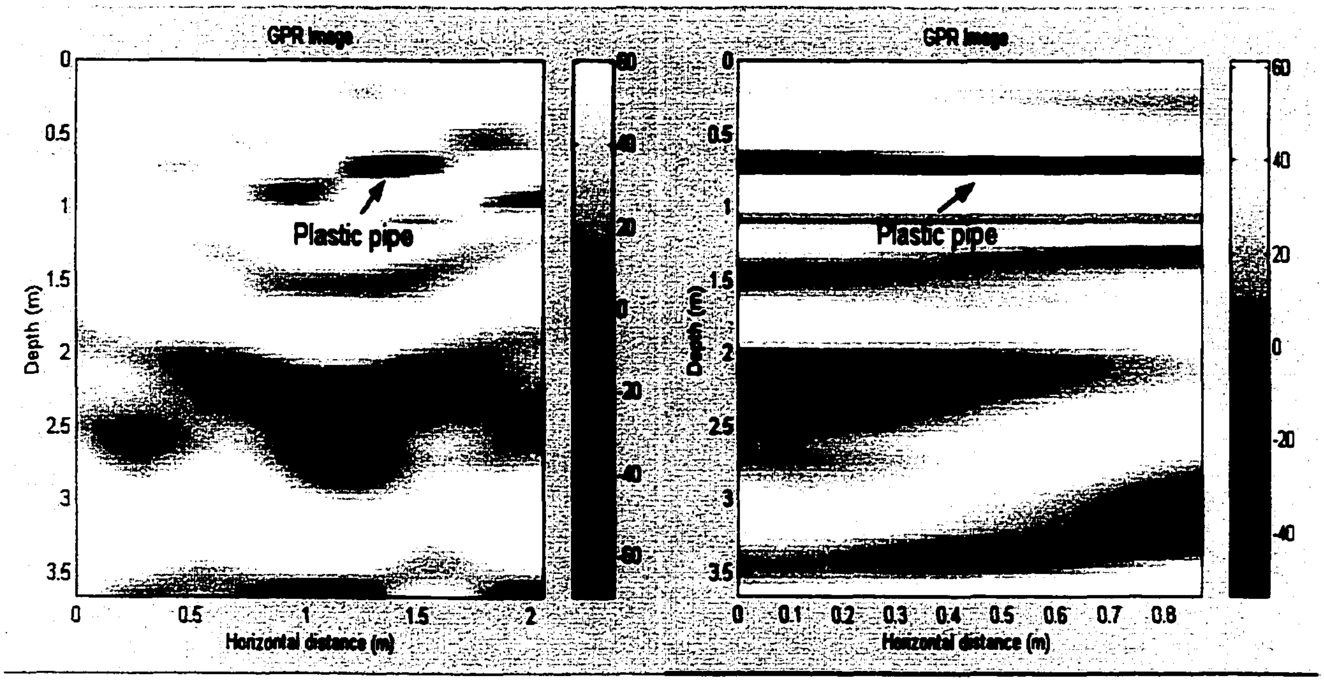

Figure 4-37: x-z slice (left) and y-z slice (right) of the three-dimensional DT reconstruction of a plastic pipe.

5 Conclusion and Discussion

In this thesis, a regularized pseudo-inverse algorithm is applied to two-dimensional and three-dimensional multi-monostatic GPR data. The method employs a linear scattering model for electromagnetic wavefields based on the Born approximation, which is inverted analytically to yield a subsurface image based on scattered field measurements. It provides a direct, non-iterative inversion formula, which has an advantage of computational efficiency. For synthetic GPR data, the reconstruction solutions satisfy the forward models exactly. For experimental GPR data, there is no apriori characterization of the frequency-dependent antenna beam pattern. The beam pattern function is determined empirically based on the quality of the reconstructed images of the object (such as a pipe) known to be evident in the data. After this calibration, the object (pipe) as well as the deeper region of a saturated or non-saturated soil background are well resolved in the images.

Reconstructions have been obtained for both a lossless and a lossy background. In realistic GPR imaging applications, the attenuation caused by the host geology is inevitable, and the evanescent wavefield components are important since radar wavelengths are often times on the same order as the depth and size of underground features of interest. Thus in this algorithm, soil attenuation can be incorporated into the mathematical inversions, and evanescent components are included to help improve image resolution. Point sources/receivers are assumed in most of the traditional imaging methods. Here, the more realistic Kerns' scattering matrix formulation is used to simulate the transmitter/receiver beam pattern.

This work is an extension of a DT algorithm for multi-monostatic GPR imaging developed by Deming and Devaney [10]. There are also some directions for future extensions based upon the present work. First of all, we can do some further characterization of antenna beam patterns. For example, a delta function response can be generated by a buried steel ball. By using scattered field measurements over a steel ball and the traditional DT algorithm, the antenna beam pattern can be quantified analytically for a particular antenna pair in a GPR experiment. This antenna beam pattern then can be used in our pseudo-inverse reconstruction to get a better image of other features. Our imaging algorithm can also be used to reconstruct images for multi-bistatic GPR data by introducing slight changing into the mathematical formulation. Furthermore, it will be of interest to use Kaczmarz method [10, 25] and find computationally efficient ways to incorporate prior information, thus obtaining image enhancement.

References

[1] A.P. Annan, "Uses and Techniques of Ground Penetrating Radar in Near-Surface Geophysics", *Ground Penetrating Radar Workshop Notes*, SEG Continuing Education, 1992.

[2] U. Basson, "Imaging of Active Fault Zone in The Dead Sea Rift: Evrona Fault Zone as A Case Study", Thesis submitted for the degree of Ph.D., Tel-Aviv University, Raymond & Beverly Sackler, Faculty of Exact Sciences, Department of Geophysics & Planetary Sciences, 2000.

[3] M. Bertero, "Linear inverse and ill-posed problems", *Advances in Electronics and Electron Physics*, vol. **75**, pp. 1-121, 1988.

[4] M. Cheney, "Tomography Problems arising in Synthetic Aperture Radar", pp. 1-16, 2000.

[5] W.C. Chew, *Waves and Fields in Inhomogeneous Media*, New York: IEEE Press, 1990.

[6] D. Colton, H.W. Engl, A.K. Louis, J.R. McLaughlin and W. Rundell, *Surveys on Solution Methods for Inverse Problems*, SpringerWienNewYork, 2000.

[7] J.L. Davis and A.P. Annan, "Ground Penetrating Radar for High Resolution Mapping of Soil and Rock Stratigraphy", *Geophysical Prospecting*, Vol. **37**, pp. 531-551, 1989.

[8] S.R. Deans, *The Radon Transform and Some of Its Applications*, John Wiley and Sons, 1983.

[9] R.W. Deming, "New Tomographic Imaging Methods for Geophysical and Medical Applications", Thesis submitted for the degree of Ph.D., Northeastern University, Boston, Massachusetts, Department of Electrical and Computer Engineering, 1996.

[10] R.W. Deming and A.J. Devaney, "Diffraction tomography for multi-monostatic ground penetrating radar imaging", *Inverse Problems*, **13**, pp. 29-45, 1997.

[11] A. Derneryd and A. Lagerstedt, "Novel Slotted Waveguide Antenna with Polarimetric Capabilities", *Proc. of IGARSS Conference*, Firenze, Italy, pp. 2054-2056, 1995.

[12] A.J. Devaney, "A Filtered Backpropagation Algorithm for Diffraction Tomography", *Ultrasonic Imaging*, Vol. bf 4, pp. 336-350, 1982.

[13] A.J. Devaney, "Geophysical Diffraction Tomography", *IEEE Trans. on Geosciences and Remote Sensing*, GE-**22**, pp. 3-13, 1984.

[14] A.J. Devaney and D. Zhang, "Geophysical Diffraction Tomography in A Layered Background", *Wave Motion*, Vol. **14**, pp. 243-265, 1991.

[15] A.J. Devaney, "Introduction to Inverse Scattering Theory", Stanford Lectures, Lecture I, August 1999.

[16] D.E. Dudgeon and R.M. Merserau, *Multidimensional Digital Signal Processing* , Ch. **7**, Englewod Cliffs NJ: Prentice Hall, 1984.

[17] P. Gilbert, "Iterative Methods for The Three Dimensional Reconstruction of An Object from Projections", *J. Theor. Biol.*, Vol. **36**, pp. 105-117, 1972.

[18] R. Gordon, R. Bender and G.T. Herman, "Algebraic Reconstruction Techniques (ART) for Three-Dimensional Electron Microscopy and X-ray Photography", *J. Theor. Biol.*, Vol. **29**, pp. 471-481, 1970.

[19] R. Gordon and G.T. Herman, "Three-Dimensional Reconstruction from Projections: A Review of Algorithms", *Int. Rev. Cytol.*, Vol. . **38**, pp. 111-151, 1974.

[20] R. Gordon, "A Tutorial on ART", *IEEE Trans. Nuclear Science*, NS-**21**, pp. 78-93, 1974.

[21] L. Hatton, M.H. Worthington and J. Makin, *Seismic Data Processing: Theory and Practice*, Blackwell Scientific Publications Inc., 1986

[22] G.T. Herman and A. Lent, "Iterative Reconstruction Algorithms", *Comput. Biol. Med*, Vol. **6**, pp. 273-294, 1976.

[23] G.T. Herman, "Image Reconstruction form Projections", *The Fundamentals of Computerized Tomography*, New York: Academic, 1980.

[24] C. Jorgensen, M. Speece and A.J. Witten, "Three-Dimensional Diffraction Tomography using GPR", *70th Ann. Internat. Mtg: Soc. of Expl. Geophys.*, pp. 1247-1250, 2000.

[25] S. Kaczmarz, "Approximate Solution of Systems of Linear Equations", *Int. J. Control.* Vol. **57**, No. 6, pp. 1269-1271, 1993.

[26] A.C. Kak, "Computerized Tomography with X-ray, Emission, and Ultrasound Sources", Proc. IEEE, Vol. **67**, pp. 1245-1272, 1979.

[27] D.M. Kerns, "Plane-Wave Scattering-Matrix Theory of Antennas and Antenna-Antenna Interactions", National Bureau of Standards Monograph, Washington, DC: US Govt Printing Office, 1981.

[28] K.T. Ladas and A.J. Devaney, "Generalized ART Algorithm for Diffraction Tomography", *Inverse Problems*, Vol. **7**, pp. 109-125, 1991.

[29] K.T. Ladas and A.J. Devaney, "Iterative Methods in Geophysical Diffraction Tomography", *Inverse Problems*, Vol. **8**, pp. 119-132, 1992.

[30] K.T. Ladas and A.J. Devaney, "Application of An ART Algorithm in An Experimental Study of Ultrasonic Diffraction Tomography", *Ultrasonic Imaging*, Vol. **15**, pp. 48-58, 1993.

[31] V.A. Lakshiminarayanan and A. Lent, "Methods of Least Squares and SIRT in Reconstruction", *J. Theor. Biol.* Vol. **76**, pp. 267-295, 1979.

[32] K.J. Langenberg, M. Brandfass, K. Mayer, T. Kreutter, A. Brüll, P. Felinger and D. Huo, "Principles of Microwave Imaging and Inverse Scattering", *EARSeL Advanced in Remote Sensing*, Vol. **2**, pp. 163-186, 1993.

[33] W. Menke, *Geophysical Data Analysis: Discrete Inverse Theory*, revised edition: Academic Press Inc., 1989.

[34] J.E. Molyneux and A.J. Witten, "Diffraction Tomography Imaging in a Monostatic Measurement Geometry", *IEEE Trans. on Geosciences and Remote Sensing*, Vol. **31**, No. 2, pp. 506-511, March 1993.

[35] C.L. Morgan, *Basic Principles of Computed Tomography*, University Park Press, 1983.

[36] P.M. Morse and H. Feshbach, *Methods of Mathematical Physics*, vol. **1**, McGraw-Hill, New York, 1953.

[37] F. Natterer, *The Mathematics of Computerized Tomography*, New York: Wiley, 1986.

[38] S. Nilsson, "Application of Fast Backprojection Techniques for Some Inverse Problems of Integral Geometry", Linköping Studies in Science and Technology, Dissertation No. 499, 1997.

[39] S.J. Norton and M. Linzer, "Ultrasonic Reflectivity Imaging in Three dimensions: Exact Inverse Scattering Solutions for Plane, Cylindrical and Spherical Apertures", *IEEE Trans. Biomed. Eng.*, BME-*28*, pp. 202-220, 1981.

[40] R.N.O. Petersson, A.G. Derneryd and P. Ingvarson, "Microstrip Antennas for Remote Sensign Satellites", *Proceedings of PIERS Conferences*, Noordwijk, The Netherlands, July 1994.

[41] R.G. Pratt and M.H. Worthington, "The Application of Diffraction Tomography to Cross-hole Seismic Data", *Geophysics*, Vol. **53**, No. 10, pp. 1284-1294, Oct. 1988.

[42] Slaney M., Kak A.C. and Larsen L.E., "Limitations of Imaging with First Order Diffraction Tomography", *IEEE Trans. Microwave Theory Tech.*, **MTT-32**, pp. 860-873, 1984.

[43] L.J. Squires and G. Cambois, "A Linear Filter Approach to Designing Off-diagonal Damping Matrices for Least-squares Inverse Problems", *Geophysics*, Vol. **57**, No. 7, pp. 948-951, July 1992.

[44] R.R. Stewart, "Exploration Seismic Tomography: Fundamentals", Course Notes Series, Vol. **3**, S.N. Domenico, Editor, Society of Exploration Geophysicists, 1991.

[45] A. Tarantola, "Linearized Inversion of Seismic Reflection Data", *Geophysical Prospecting*, Vol. **32**, pp. 998-1015, 1984.

[46] C.W. Therrien, *Discrete Random Signals and Statistical Signal Processing*, Prentice Hall, Englewood Cliffs, New Jersey, 1992.

[47] F. Treves, *Basic Linear Partial Differential Equations*, Academic Press, New York, 1975.

[48] J.C. VanDecar and R. Snieder, "Obtaining Smooth Solutions to Large, Linear, Inverse Problems", *Geophysics*, Vol. **59**, No. 5, pp. 818-829, May 1994.

[49] A.J. Witten and E. Long, "Shallow Applications of Geophysical Diffraction Tomography", *IEEE Transactions on Geosciences and Remote Sensing*, GE-**24**, No. 5, pp. 654-662, 1986.

[50] A.J. Witten and J.E. Molyneux, "Geophysical Imaging with Arbitrary Source Illumination", *IEEE Trans. Geosci. and Remote Sensing*, GE-**26**, pp. 409-419. 1988.

[51] A.J. Witten and W.C. King, "Sounding Out Buried Waste", *Civil Engineering*, Vol. **60**, pp. 62-64, 1990.

[52] A.J. Witten, "The Application of a Maximum Likelihood Estimator to Tunnel Detection", *Inverse Problems*, Vol. **7**, pp. L49-L45, 1991.

[53] A.J. Witten and J.E. Molyneux, "Geophysical Diffraction Tomography: Validity and Implementation", *Geophysical Inversion*, Eds. J.B. Bednar, J.R. Lines, R.H. Stolt and A.B. Weglein (SIAM), pp. 354-369, 1992.

[54] A.J. Witten, S.S. Stevens, W.C. King and J.R. Ursic, "Field Studies in Geophysical Diffraction Tomography", *Inverse Problems in Scattering and Imaging*, Vol. **1767**, pp. 177-185, 1992.

[55] A.J. Witten, D.D. Gillette, J. Sypniewski and W.C. King, "Geophysical Diffraction Tomography at a Dinosaur Site", *Geophysics*, Vol. **57**, pp. 187-195, 1992.

[56] A.J. Witten, J.E. Molyneux and J.E. Nyquist, "Ground Penetrating Radar Tomography: Algorithms and Case Studies", *IEEE Trans. on Geosciences and Remote Sensing*, Vol. **32**, No. 2, pp. 461-467, March 1994.

[57] A.J. Witten, W.C. King and J.R. Ursic, "High Resolution Image Processing of Geophysical Data with Diffraction Tomography", *Army Science: Then New Frontiers, Military and Civilian Applications*

[58] A.J. Witten, T.E. Levy, J.R. Ursic, and Paul White, "Geophysical Diffraction Tomography: New Views on the Shiqmim Prehistoric Subterranean Village Site (Israel)", *Geoarchaeology: An International Journal*, Vol. bf 10, No. 2, pp. 97-118, 1995.

[59] A.J. Witten, "Three-dimensional Imaging from $2\frac{1}{2}$-dimensional reflection measurements", *Geophysical Research Letters*, Vol. **26**, No. 24, pp. 3701-3704, December 1999.

[60] E. Wolf, "Three-Dimensional Structure Determination of Semi-Transparent Objects from Holographic Data", *Optical Communications*, Vol. **1**, pp. 153, 1969.

[61] R. Wu and M.N. Toksöz, "Diffraction Tomography and Multisources Holography Applied to Seismic Imaging", *Geophysics*, Vol. **52**, No. 1, pp 11-25, Jan. 1987.

[62] R. Wu, F.V. Araujo and L. Huang, "Multifrequency Backscattering Tomography for Constant and Vertically Varying Backgrounds", *Int. J. Imaging Systems and Tech*, Vol. **5**, pp. 7-21, 1994.

[63] R. Zahn and M. Schlott, "Active Antenna for X-band Space SAR", *Proc. Int. Conf. on Radar*, Paris, France, pp. 36-41, 1994.